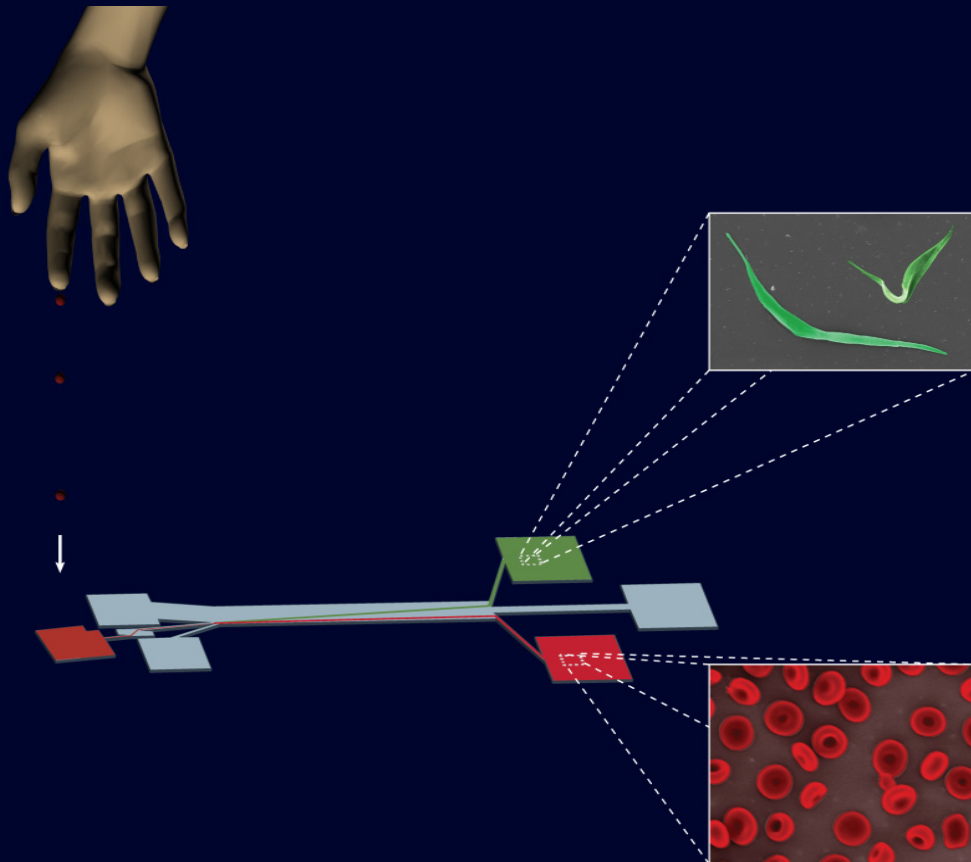


Microfluidic Cell Sorting and Analysis

– Point-of-Care Diagnosis of Human African Trypanosomiasis



Stefan H. Holm

*Solid State Physics
Department of Physics
Lund University*



LUND
UNIVERSITY

Microfluidic Cell Sorting and Analysis

– Point-of-Care Diagnosis of Human African Trypanosomiasis

Master of Science Thesis

Stefan H. Holm

Supervisors

Jonas Tegenfeldt

Jason Beech

Opponents

Greger Hammarin

Mattias Törnqvist

*Solid State Physics
Department of Physics
Lund University*



LUND
UNIVERSITY

Division of Solid State Physics
Department of Physics
Lund University
P.O. Box 118
S-221 00 Lund

Copyright © Stefan Holm 2012
Printed in Sweden by Media-Tryck, Lund
June 2012

Table of Contents

Abstract	7
Swedish summary	8
- <i>Populärvetenskaplig sammanfattning</i>	8
Preface and acknowledgements	9
List of Articles	12
List of Acronyms and Notations	13
1. Introduction	17
1.1 Applicable particle sorting techniques	19
1.3 Deterministic lateral displacement in brief	19
1.3 Summary of the objectives of the thesis	23
2. Fluid theory	27
2.1 Fluid Theory	28
2.2 Diffusion	34
3. Deterministic Lateral Displacement	39
3.1 Theory	40
3.2 Flow simulations	43
3.3 Device design	47
3.4 Dynamic range	50
3.5 Sorting based on shape	53
3.6 Existing shape-sensitive sorting devices	54
4. Human African Trypanosomiasis	57
4.1 Variants	58

Table of Contents

4.2 Endemic foci	58
4.3 Treatment	60
4.4 Trypanosome life cycle	61
4.5 Characteristics of <i>Trypanosoma brucei</i>	62
4.6 Immune response evasion of <i>Trypanosoma brucei</i>	63
4.7 Detection and diagnosis	64
4.7.1 <i>Card Agglutination Test for Trypanosomiasis</i>	65
4.7.2 <i>Blood-film examination</i>	66
4.7.3 <i>Lymph node aspirate</i>	66
4.7.4 <i>mini-Anion-Exchange Centrifugation Technique</i>	66
4.7.5 <i>Micro-hematocrit centrifugation technique</i>	66
4.7.6 <i>Quantitative Buffy Coat</i>	67
4.8 <i>Trypanosoma cyclops</i>	68
5. Blood	69
5.1 Composition	70
5.2 Red blood cells	73
5.3 Red blood cell deformability	75
5.3.1 <i>Erythrocyte filtration</i>	78
5.3.2 <i>Ektacytometry</i>	78
5.3.3 <i>Micropipette aspiration technique</i>	78
5.3.4 <i>Erythrocyte sedimentation rate</i>	79
5.4 Microfluidic methods for red blood cell deformability analysis	79
5.4.1 <i>Restriction based microfluidic devices</i>	80
5.4.2 <i>Laser-based microfluidic devices</i>	81
5.5 Anemia	83
5.5.1 Sickle cell anemia	83
5.5.2 Thalassemia	84
5.5.3 Pernicious anemia	84
5.6 Anemia and HAT	85
6. Experimental Details	87
6.1 Device fabrication	88
6.4 Result analysis	95
6.4.1 <i>Particle tracking software</i>	96
6.5 Biological methods	99

Table of Contents

6.5.1 Hematological methods	99
6.5.2 Trypanosome handling	100
6.5.3 Characteristics of <i>T. cyclops</i>	103
7. Device design and characterization	105
7.1 Device design	105
7.2 Characterization of the device performance	111
8. Blood analysis	117
8.1 Effect of channel depth	118
8.2 Effect of pressure	119
8.3 Osmolarity measurements	122
8.3.1 Osmolarity and RBC morphology	122
8.3.2 Red blood cells analysis in deterministic lateral displacement devices under non-isotonic conditions	126
10. Conclusions	139
Appendix 1. Sample preparation	143
A1.1 Drawing blood samples	143
A1.2 Trypanosome samples	143
A1.3 Simultaneous analysis	143
A1.3 Staining of <i>T. cyclops</i>	143
A1.4 DiI staining of RBC	144
A1.5 Preparation of Cunningham's medium from dry salt	144
Appendix 2. Handling of <i>T. cyclops</i>	145
A2.1 Freezing	145
A2.2 Reactivation	145
A2.3 Culture splitting	145
Appendix 3. Device fabrication	147
A3.1 UV lithography	147
A3.2 Soft Lithography	148
A3.3 Preparation for SEM of RBC and trypanosomes	149
Appendix 4. Osmolarity Measurements	150

Table of Contents

Appendix 5. MATLAB and Java code	153
A5.1 Particle tracker	153
<i>Outletgraph.m</i>	173
<i>fixAndTrack.m</i>	175
A5.2 Java program for designing the array	176
Appendix 6. Laboratory Setup	188
Published Manuscript	187
References	194

Abstract

In this master thesis project a new method for diagnosing sleeping sickness in Africa has been developed. Today, the scarce number of parasites in blood compared to the huge amount of blood cells, mainly red blood cells (RBCs), makes correct diagnosis of people infected with sleeping sickness problematic. Especially in field-diagnosis where microscopic examination of blood smears is the most common method of detection. The method presented herein is based on deterministic lateral displacement (DLD), a technique which primarily has been used to separate spherical cells and particles of different sizes. As shown in this thesis, the separation of particles in a conventional DLD device is mainly based on the smallest dimension of cells. For red blood cells (RBCs) and the trypanosome parasites this size is identical, 2.5 μm . Instead, the differences in morphology were utilized to achieve separation. The long and slender trypanosomes can be sorted out from a sample of the disc shaped RBCs by optimization of the channel depth. The depth where best separation was achieved was just above the diameter of the RBCs. Due to interaction with the shear field of the fluid, the RBCs behaved as 2.5 μm small particles while the rotation of the trypanosomes is hindered as the channel depth was smaller than its longest dimension, consequently its effective size was increased. This maximized the difference in behavior, *i.e.* effective size, and consequently separation efficiency. Around 99 % of the RBCs were estimated of being separated from the parasite which, in a final device, could considerably increase detection limit and minimize false positives during diagnosis.

Keywords: Deterministic Lateral Displacement, Separation science, Microfluidics, Sleeping-sickness, Lab-on-a-Chip, Point-of-Care.

Swedish summary

- Populärvetenskaplig sammanfattning

I detta arbete har en ny metod för diagnosticering av sömnsjukan i Afrika utvecklats. Vanligen vid diagnosticering utgör parasiternas, trypanosomernas, låga koncentration i förhållande till de normala blodcellerna, framför allt röda blodcellerna, ett stort problem. Kombinerat med att den vanligaste metoden för att påvisa parasiterna är enkla undersökningar av blodprov i primitiva mikroskop blir det många prov som felaktigt får ett negativt resultat. Metoden som används i detta arbete är deterministisk sidoförskjutning (DLD), en teknik vilken främst har använts för att separera sfäriska celler och partiklar av olika storlek från varandra. I en konventionell DLD blir partiklar separerade från varandra beroende på deras minsta dimension, vilket också visas senare i detta arbete. Detta utgör ett problem i separationen mellan röda blodceller och trypanosomparasiterna då dess minsta storlek är identisk, 2.5 μm . För att erhålla separation implementeras en ny metod i DLD där separationen påverkas av partiklarnas former. Genom att använda DLD system med optimalt djup kan de långa och ringlande parasiterna sorteras ut från de bikonkava röda blodcellerna. Efter test av flera olika djup visade det sig att bäst separation erhöles vid ett djup precis över diametern av de röda blodcellerna. Vid detta djupet kan de röda blodcellerna rotera fritt och de kommer på grund av flödets skjuvkrafter tvingas att sorteras beroende på deras minsta diameter. De längre parasiterna kan inte rotera fritt utan de kommer att sorteras som större partiklar. Cirka 99% av de röda blodcellerna var uppskattade att bli separerade från parasiterna, detta skulle i en slutlig apparat leda till en betydligt lägre gräns för vilka koncentrationer av parasiter i blodet man kan detektera och därmed skulle man kunna undvika en stor del av de felaktiga diagnoserna.

Preface and acknowledgements

I first met Jonas and Jason during the experimental biophysics course given in my last semester in my studies towards my Master of Science degree in nanotechnology. The course differed from every other course I had up until that time. The focus was heavily on experimental work and problem solving, the closeness to research was clear immediately. During the course the research field was covered and we were given presentations about the research conducted in Jonas group. I had already been interested in microfluidics from an earlier course, but this course widened my sight of its possibilities. Jason, who had done his Master thesis for Jonas, and at this time was in pursuit of his PhD degree in the same group, had done a great amount of work related to the deterministic lateral displacement (DLD) technique. A microfluidic particle separation technique which was developed at Princeton, the same place and at the same time as Jonas did a Postdoc. The technique had thereafter continued to be developed at Lund University and recently before I started my work they had shown how the behavior of the sorting of the non-spherical red blood cells (RBCs) could be affected by the depth of the channel. A method which had the potential of opening up for shape based particle sorting. During a conference Jonas and Jason met Dr Mathis Riehle who introduced them to the problem of sorting parasites from human blood for improved detection and diagnosis. The smallest dimension of the RBCs (their width, $\sim 2.5 \mu\text{m}$) is almost identical to the width of trypanosome parasite, due to the fact that sorting in a conventional DLD is significantly influenced by the smallest dimension; separation would be difficult with low sensitivity as a result. A shape based particle sorting device would have the potential to separate parasites and RBCs more efficiently due to

their large morphological differences, with the parasites being long, slender and worm-like while the RBCs are biconcave disc-shaped.

When I was asked after the course if I was interested in taking on this project I did not think twice and have never regretted my decision. Much work has been put into this project and many times we have faced difficult problems, however, long nights, hard work and great input from Jason and Jonas has been a recipe for success in this project.

Several people have been provided significant help and contributed to making this project fruitful. First, Jonas, who has always believed in me and, with great knowledge and creative ideas, helped solve any problem we have faced. Besides the input to the project the writing of the manuscript and this thesis was made straight forward with the input from Jonas.

My other supervisor, Jason, is always full of ideas how to overcome any obstacles on the journey. He did a great amount of work on DLD devices including optimization of device manufacturing and was happy to share all of his results. He also did a great amount of work on the article (article I) which much of the work presented herein resulted in. Many times, we struggled together for long hours in the lab, not every time successful but Jason's energy and passion made these time easy.

Several other people have provided help for this project. First, Mike Barrett at Glasgow University, the institute of infection, immunity and inflammation, provided us with parasite samples and culture medium which was used in the experiments. He has always been helpful and also given insight into the field of trypanosomiasis research, including what is needed in field-detection. Further people in Mike's group who have been involved are Gordon Campbell and Federica Giordani who have been cultivating the parasites and provided us with detailed instructions of how to keep them alive.

In Lund University I have enjoyed my time as part of the bio-group at solid state physics. The Friday meetings with interesting presentations

and something for a sweet tooth is a great time for fruitful discussions. In this group several people has provided significant input, Henrik Persson, together with Fredrik Johansson, have provided us with help related to fixation of cells and SEM work. Martina Balaz provided input on how to set up the sterile cultivation for the parasites. The rest of the biogroup have provided valuable feedback during presentations of our work.

Several other employees at FTF have helped me during my stay here. To name a few, Lena Timby, Mona Hammar, Anneli Löfgren and Anders Gustafsson. They did a variety of tasks in order to make my stay here as easy as possible, including much of the administrative work. Ivan Maximov, Mariusz Graczyk and Anders Kvennefors have provided help in the clean room, mainly but not limited to the work related to SU8 processing and device characterization.

Further, my friends and family who have always been supportive has made long hours in the lab and any setback easier to tackle, I am truly grateful for all of you.

List of Articles

I. Separation of Parasites from Human Blood Using Deterministic Lateral Displacement

Stefan H. Holm*, Jason P. Beech*, Michael P. Barrett and Jonas O. Tegenfeldt

Lab Chip, 2011, 11, 1326-1332

DOI: 10.1039/C0LC00560F

II. Sorting cells by size, shape and deformability

Jason P. Beech*, Stefan H. Holm, Karl Adolfsson and Jonas O. Tegenfeldt

Lab Chip, 2012, 12, 1048-1051

DOI: 10.1039/C2LC21083E

List of Acronyms and Notations

A	area
AFM	atomic force microscopy
BBB	blood-brain barrier
C	compactness number
CATT	card agglutination test for trypanosomiasis
CDC	centers for Disease control and prevention
CFD	computational fluid dynamics
CiATT	indirect agglutination test for trypanosomiasis
CNS	central nervous system
CSF	cerebrospinal fluid
CV	coefficient of variation
d	depth
D	diffusion constant
D_c	critical diameter
Da	Dalton
DAPI	4',6-diamidino-2-phenylindole
D_c	critical diameter
DLD	deterministic lateral displacement
DMSO	dimethylsulfoxide
EC	ektacytometry
EDTA	ethylenediaminetetraacetic acid
ESR	erythrocyte sedimentation rate test
EtOH	ethanol
FACS	fluorescence-activated cell sorter
FBS	fetal bovine serum
FOV	field-of-view
FFT	fast Fourier transform

List of Acronyms and notations

FPS	frames per second
FEM	finite element method
G	gap size
GUI	graphical user interface
h	height
HAT	human African trypanosomiasis
Hb	hemoglobin
HbS	sickle cell variant hemoglobin
HSt	hereditary stomatocytosis
KOH	potassium hydroxide
L	litre
l	characteristic length
LDE	laser diffracted ellipsometry
Le	entrance length
LNA	lymph node aspiration technique
LOC	lab-on-a-chip
Le	entrance length
L _s	length of array section
M	mole
m	metre
μ	micro
mAECT	mini-anion-exchange chromatography
MAT	micropipette aspiration technique
MCH	mean corpuscular hemoglobin
MCV	mean corpuscular volume
MEMS	microelectromechanical systems
MHCT	micro-hematocrit centrifugation technique
n	nano
N	array period
NaCl	sodium chloride
NaOH	sodium hydroxide
NPV	negative predictive value
O	oxygen
Osm	osmolarity

List of Acronyms and notations

P	pressure
ρ	density
PBS	phosphate-buffered saline
PDMS	poly-(dimethylsiloxane)
Pe	Péclet number
PEB	post-exposure bake
PEG	polyethylene glycol
PFP	parabolic flow profile
pH	potential hydrogen
PLL	poly-L-lysine
POC	point-of-care
PPV	positive predictive value
PVP	polyvinylpyrrolidone
QBC	quantitative buffy coat
R	fluidic resistance
RBC	red blood cell
RCF	relative centrifugation factor
Re	Reynolds number
R_{hyd}	hydraulic resistance
RMS	root-mean-square
SAV	surface area-to-volume ratio
SEC	size exclusion chromatography
SEM	scanning electron microscope
SIT	sterile insect technique
SS	sleeping sickness
Std	standard deviation
T	temperature
<i>T. brucei</i>	<i>Trypanosoma brucei</i>
u	characteristic velocity
VSG	variant surface glycoprotein
w	width
WBC	white blood cell
WHO	world health organization
x, y, z	rectilinear spatial coordinates

List of Acronyms and notations

Z	zeta potential
ZSR	zeta sedimentation rate
α	correction factor
ΔN	row shift fraction
λ	center -to-center distance

1. Introduction

This thesis concerns the field of microfluidics, a wide spanning field which can be described as consisting of systems of small, micrometer-sized, channels for the analysis, processing and manipulation of liquids in the volume range of nano- to attolitres. The spark, which initiated the growth of microfluidic science, is in large part attributed to advances in related fields such as the advent of semiconductor processing and molecular analysis through chromatography. Photolithography, etching and other methods for processing silicon had proven to be a tremendous success in fabrication of integrated circuits and microelectromechanical systems (MEMS) devices and gave a method, which could be directly applied in the creation of microfluidic devices. This, together with recent advances in other analysis technologies such as chromatography, lead to an increased belief in the great potential that microfluidics could offer. Some of the advantages stem directly from the smaller size of microfluidic systems, such as a lower energy, liquid, sample and reagent consumption and the ability to analyze very small volume samples. Others include the possibility to integrate many smaller processing units, each with its own specific task, into larger systems capable of advanced sample processing, which would otherwise require all the equipment and personnel of a large scale laboratory. This is often referred to as a Lab-On-a-Chip (LOC), where the common goal is to incorporate the function, whether analytical, preparative or both, of a complete laboratory environment onto a small, handheld chip. It is easy to make comparisons to the evolution of information technology rendering the computers and smartphones of today. Much as in the same way as Eniac³ and other early computers had sizes comparable to houses and now have the

ability to fit into the palm of our hands, a whole lab can be scaled down to a single microfluidic chip, with a size of a few square centimeters. It would not just decrease the cost per test considerably but also has the potential to make diagnostic devices portable. A few examples have already been brought to the market and are in widespread use, one is the glucose monitor with which diabetes patients can obtain an instant and accurate reading of their current blood-sugar levels. This enables the person to make any adjustments required through self-injection of insulin, without the need for daily visits to a hospital and consequently the person can live a completely normal life. This is one example of a Point-Of-Care (POC) device: a cheap, portable, low-energy consuming apparatus which brings diagnosis to the location where it is needed. Much of the work presented herein is focused on the designing, processing and characterization of another POC application, namely a device capable of diagnosing Sleeping Sickness (SS) or Human African Trypanosomiasis (HAT). The disease is endemic across the whole African continent, mainly in the northern Sub-Saharan Africa, which includes some of the poorest countries of the poorest continent on Earth. In these areas resources are scarce and the absence of medical equipment and facilities for both diagnosis and treatment has given the disease the ability to cause serious harm to human life. At the same time, the drugs used for treatment can cause severe side effects, making it crucial to have tools for accurate patient screening before treatment. By bringing cheap, easy to use, POC devices to these remote areas mass screening followed by rapid treatment would be made possible. By starting medication at an early stage, patients will both have a greater chance of successful recovery and it would also swiftly prevent further spread of the disease. Apart from increasing the quality of life considerably in the region it would also have the potential of completely eradicating the disease.

Accurate diagnosis of HAT relies on finding the parasite that causes the disease, *Trypanosoma brucei* (*T. brucei*). Often this is done by examining blood smears microscopically, but as 1 mL of blood contains around $5 \cdot 10^9$ red blood cells (RBCs) while there is a strong interest in diagnosis even in the cases when the HAT parasitemia (*i.e.* parasite concentration in the blood) is below 100 per mL there is a huge amount of background cells which act to impede detection with a large number of false negatives as a result. This problem has been in the center of this investigation and the focus has been on constructing a device capable of separating the *Trypanosoma* parasite from the huge background predominately consisting of RBCs. Separation followed by subsequent collection of the sorted cells would lead to an enrichment of the parasites, which would facilitate simple detection.

1.1 Applicable particle sorting techniques

There exists a wide range of passive, continuous, label-free microfluidic particle separation techniques. Hydrodynamic filtration⁴ and pinched flow fractionation^{5, 6} are two examples which rely on flow lanes of specific widths into which particles above a certain size cannot enter. Others instead utilize the hydrodynamic properties of soft cells in microchannels to achieve separation^{7, 8}. An interesting example is how ratcheting of cells can be utilized to avoid clogging of sieving structures.⁹ A final example is devices based on inertial effects.^{10, 11} These utilize the lift forces and secondary flows present in microchannels with flows run at Reynolds number greater than unity. Several reviews of these and other related techniques¹²⁻¹⁴ are available where the interested reader can obtain a more in-depth insight into these and other related microfluidic particle sorting techniques.

1.3 Deterministic lateral displacement in brief

The different microfluidic particle separation techniques discussed above all have their own advantages and disadvantages depending both on what parameters are needed to be utilized to achieve separation of particles and also what other factors are desirable during separation

(e.g. low cost, high throughput and simplicity of use). The technique which we have employed for developing a device, to operate in the field and capable of separation of parasites from human blood, is known as deterministic lateral displacement (DLD) and was first described by Huang *et al.* in 2004¹⁵ where a separation of spherical micrometer-sized beads with a resolution on the order of 10 nm was achieved. It has since been shown to be able to sort particles in a broad range of sizes from 70 nm¹⁶ to 40 μm ¹⁷. More detailed discussions on DLD are found in *Chapter 3*. In short, DLD relies on the laminar flow often present in microfluidics. Thus the regimes relevant to DLD can be estimated by the Reynolds number, *Equation (1)*, which is a measure of the ratio between the inertial and viscous forces.

$$R_e = \frac{\text{inertial forces}}{\text{viscous forces}} = \frac{D_H u \rho}{\eta} \quad (1)$$

Here, η is the dynamic viscosity of the fluid, ρ the density of the fluid, u the characteristic flow speed and D_H is the hydraulic diameter, which equals four times the cross-sectional area divided by the wetted perimeter. Often microfluidic devices operate at Reynolds numbers below 1, which is indicative of laminar flow. Generally the transition from laminar flow to turbulent flow is estimated to occur in the range from $R_e=100-2000$. *Figure 1* shows a brief illustration of how DLD is able to take advantage of this microfluidic phenomenon. Shown here is the flow through an array of pillars together with particles of two different sizes. The low Reynolds number flow act to obtain a symmetric bifurcation of the flow in the periodic post array. Depending on the distance between the pillars and the distance each row is displaced with respect to its preceding row the sizes of the flow streams will vary. In this specific example the smaller green particle is able to fit within the first flow stream closest to the post while the hydrodynamic center of the larger red particle is located in the second

flow stream. The green particle will therefore continue to reside in the same stream as it started; the red particle, however, will at each row of pillars be laterally displaced into the adjacent flow stream. This lateral displacement of particles is not a stochastic process, in contrast to many other microfluidic particle separation methods, and is what has given the technique its name, deterministic lateral displacement.

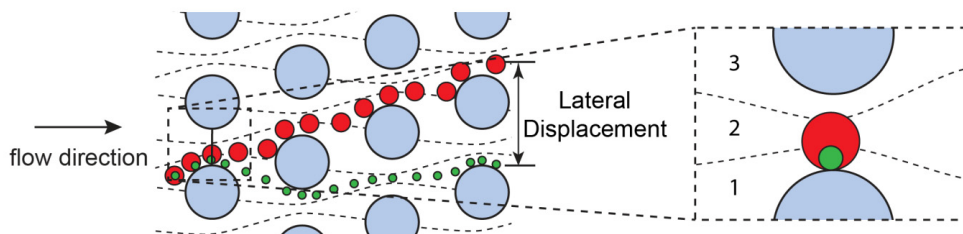


Figure 1. Illustration of a short segment of a DLD device. The low Reynolds number conditions result in a symmetric laminar flow with flow streams as shown in the illustration. The separation of the larger red particles from the smaller green depends on whether the particle's hydrodynamic center of mass is able to fit inside the flow stream closest to the posts, marked with 1 in the inset. Larger particles interact with the post and their hydrodynamic center of mass is displaced to the second flow stream resulting in a changed trajectory through the array of pillars. The small particles have a minimal interaction with the array and they are able to constantly reside in their initial flow stream, resulting in a lateral position at the exit coinciding with their initial lateral position.

Compared to the competing microfluidic particle separation techniques, DLD exhibits several highly desirable features, especially when considering POC sample processing. First it is a passive separation technique, meaning that the separation does not rely on any applied external field. The grounds for separation are the hydrodynamic driving force in combination with the steric interaction of the particles with the posts. Flow induction by non-electrical means has been shown and enables sample processing completely without the need for electricity.

Further, DLD has the ability to perform label-free separations; no staining or other manipulations of the sample are needed before analysis. This saves both costly time and also assures the sample components are as close to their original state as possible. Sorting methods relying on labeling, such as the commonly used Fluorescence

Active Cell-Sorter (FACS)¹⁸, has been shown to affect the function of the target cells due to the strong, often irreversible, conjugation between antibody and antigen¹⁹. Often, the sorting is carried out to select the subpopulation of cells desired to be further analyzed. But, if the sorting step itself acts to alter the cells in any way the validity of the final analysis can be put in question.

Furthermore, DLD is a continuous particle separation technique. The opposite would be a bulk separation technique such as size-exclusion chromatography (SEC). Here the sample is loaded into the system at a specific point in time and driven through the separation column. As the larger particles are not able to fit into the networks of smaller cavities they will have a shorter distance to travel and will consequently require shorter time to travel through the column. This difference in residence times between smaller and larger particles is the grounds for separation in this fairly widespread technique, however, to achieve separation the flow speed needs to be limited enough to give smaller particles enough time to reach the cavities where they will reside. In a continuous system, such as DLD devices, constant feeding of sample is possible and as a result easy integration in a larger system is possible. The key to achieve separation independent of time is that separation occurs perpendicular to the flow. The particle size, for example, can be determined by the lateral position at the end of the device instead of the elution time as in the previous example.

A final example of the advantages of DLD is its deterministic nature from where the technique has received its name. Unlike separation techniques based on, for example, diffusion^{20, 21}, margination⁸ or cell motility²² separation in DLD is not based on any stochastic processes. Instead the ground for separation is the deterministic lateral displacement of particles suspended in a flow under the hydrodynamic interaction with a post array. The separation efficiency is therefore not a function of the time a stochastic process is allowed to act and, in fact,

increasing the flow rates, and hence throughput, can even improve separation as it would suppress the influence of diffusion.

1.3 Summary of the objectives of the thesis

By using simple microfluidics we aim to develop a diagnostics device for HAT which has the potential to be made cheap and able to give rapid diagnosis detection. The primary objective is to enable sensitive separation of human blood and parasites to aid in parasite detection by removing the large background of blood cells, mainly RBCs. In a longer perspective the device would need to be adapted to field-use in the rural areas where the disease is endemic. The device should consequently not require any external power source and it should be portable.

The final device is intended to be both easy to operate and easy to verify the result of an analysis. At the same time it should be cheap, ~\$1 per test, and sensitive enough to compete with the large, power consuming, expensive techniques available at large hospitals, e.g. FACS^{23, 24} or automated image analysis systems^{25, 26}.

In a longer perspective, the aim for this project is to test separation of blood spiked with a, to human, pathogenic variant of the parasite, *T. brucei gambiense* or *T. brucei rhodesiense*, and also to perform analysis of actual samples from infected individuals. The safety regulations related to working with these strands of the parasite are rigorous. A class B bio hazard laboratory facility is required together with proper training and government approval. Therefore, for these initial tests the work is done with a, to human, non-pathogenic variant with similar characteristics, namely *T. cyclops*.

This thesis reports most of the, work which was done in relation to this project. It starts off, after this introduction, in **Chapter 2** with an introduction to fluid theory, deriving the resistance formulae of microfluidic channels and phenomena such as diffusion which are

increasingly important at these length scales. These were all crucial components in the decision on how the device would be designed for best performance together with simple handling and low degree of diffusion acting to decrease separation efficiency.

Chapter 3 gives a more thorough description of the DLD technique, and it also includes theory as well as several computer simulations of flow in microfluidic channels which have been done in order to verify what properties of the device are important to the critical diameter in a DLD device. Different device designs are also discussed in this section, highlighting their benefits and drawbacks.

Chapter 4 and **Chapter 5** deals with HAT and blood respectively. In the HAT chapter the disease progress is explained all the way from the midgut in the vector to second stage infection of a human host together with what treatments and diagnostics are available today. Detailed morphologies of the parasite is given, which is crucial to how the separation from blood cells in a DLD device can be carried out. Other microfluidic techniques for trypanosome detection are explained with their respective benefits and drawbacks. Likewise in the blood section, the functions of the blood, its constituents and morphology are given. Different diseases which affect the blood morphology are given together with diagnostic tools, both traditional and novel microfluidic devices.

Chapter 6 presents the experimental method from the first conceptions of a device to the final experiments. Every processing step is described in here together with answers to questions such as 'Which device designs were used and why?' and 'How was the result of an experiment quantified?'

Chapter 7 shows the results of the characterization of the device. Apart from probing the device with an atomic force microscope (AFM), the performance was measured by analyzing how spherical polystyrene beads of many different sizes behaved in the device.

Chapter 8 provides the result and a discussion of the experiments conducted with blood in the device. These measurements were conducted at different pressures, salt concentration (osmolarity) and device depths.

In **Chapter 9** the results of experiments with the trypanosome parasite are given. Due to the results from the blood chapter the method of choice for sorting out trypanosomes from blood was by optimization of the device depth. In this chapter the behavior of the parasite in devices of different depths is analyzed to determine what depth gives the highest separation efficiency. Finally separation measurements of blood spiked with trypanosomes are conducted and quantified.

Chapter 10 provides a short conclusion of the results obtained during this project and discussion about the device potential to efficiently diagnosis HAT in the field, together with a short outlook on what future measurements, optimizations and modifications the device needs to undergo before being capable of being put to use in the field.

2. Fluid theory

Definition of a liquid: "*A substance that deforms continuously under the application of shear (tangential) stress, no matter how small that stress may be. It does not expand indefinitely and is only slightly compressible*"²⁷

This section has been adapted from Nguyen *et al.*²⁸ if not stated otherwise.

Fluid flows at the micro scale in general behave completely differently than what we are used to seeing every day at the macroscale. Scaling between different variables, when decreasing the length scale act to introduce new phenomena in the micro domain.

$$\frac{\text{surface forces}}{\text{volume forces}} \propto \frac{l^2}{l^3} = l^{-1} \xrightarrow{l \rightarrow 0} \infty \quad (2)$$

As *Equation (2)* states, scaling down acts to modify the fluidic behavior such that it becomes dominated by the surface forces (e.g. viscosity and surface tension) instead of the volume forces (e.g. gravity and electromagnetism).

The molecules of a fluid are in a constant state of collision, with an overall behavior which is complex to predict theoretically. In contrast to nano channels²⁹, liquid flows in microfluidics can generally be treated as a continuum instead of a collection of point particles. This assumption is valid for standard microfluidics as around 30'000 water molecules would span a typical microfluidic channel of 10 μm . However, In order to achieve analytical solutions to the equations

governing the complex fluidic behavior, several more simplifications are typically made.

2.1 Fluid Theory

The primary laws, which are used to model any dynamic thermofluidic problem, are the conservations of mass, momentum and energy. The resulting relationships can however be simplified in several steps by considering an incompressible, Newtonian (*i.e.* the stress is directly proportional to the strain rate), isotropic liquid of constant temperature. The resulting relationships for a channel with pressure drop along the x -axis are shown in *Equation (3)* and *(4)*,

$$\frac{\partial u_i}{\partial x_i} = 0 \quad (3)$$

$$\rho \left(\frac{\partial u_i}{\partial t_i} + u_i \frac{\partial u_i}{\partial x_j} \right) = \rho \mathbf{F}_i - \frac{\partial p}{\partial x_i} + \eta \frac{\partial^2 u_j}{\partial x_j^2} \quad (4)$$

where u is the flow velocity, ρ the density, p represents the pressure and η the viscosity with Einstein summation convention.

By further assuming the channels to be straight and to have constant cross-sections the flow can be simplified to what is known as Hagen-Poiseuille flow. Together with the assumption of a no-slip boundary condition between the fluid and the wall, which is often a valid assumption in microchannels, we can simplify *Equation (3)* and *(4)* to the following relationships:

$$\frac{\partial p}{\partial y} = \frac{\partial p}{\partial z} = 0 \quad (5)$$

$$\frac{\partial p}{\partial x} = \eta \left(\frac{\partial^2 u_x}{\partial y^2} + \frac{\partial^2 u_x}{\partial z^2} \right) \quad (6)$$

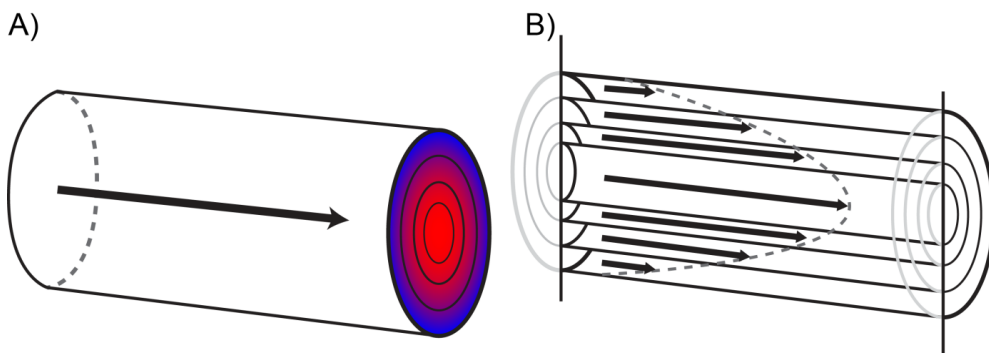


Figure 2. (A) A long straight microfluidic channel with a color-coded velocity profile of the flow. The parabolic flow profile is seen with its peak velocity in the center of the channel. (B) A cross-section of the same microfluidic channel is shown which further illustrates the laminar flow streams with a parabolic flow profile, which is a consequence of common pressure-driven flow.

With the length of the channel defined as being in the x-direction, Equation

(5) describes the pressure as being constant at any cross section throughout the channel. Pressure drop will only occur parallel to the flow. Equation (6) instead describes the relationship between the pressure drop and the velocity profile of the channel.

Solutions to these equations for many different types of cross-sections are available in the literature. Some of the solutions of the more commonly used cross-sections, namely circular, rectangular and triangular, are presented below. Circular cross-sections are often found in tubing, which is often used to connect different parts of a larger microfluidic system such as pressure sources or channels for pretreatment. Rectangular cross sections are common as a result of the planar lithographic device fabrication, for example the devices presented in this work which have been manufactured by replica molding following UV-lithography patterning of silicon. Triangular cross sections can be created by anisotropic etching, for example potassium hydroxide (KOH) treatment of silicon surfaces.

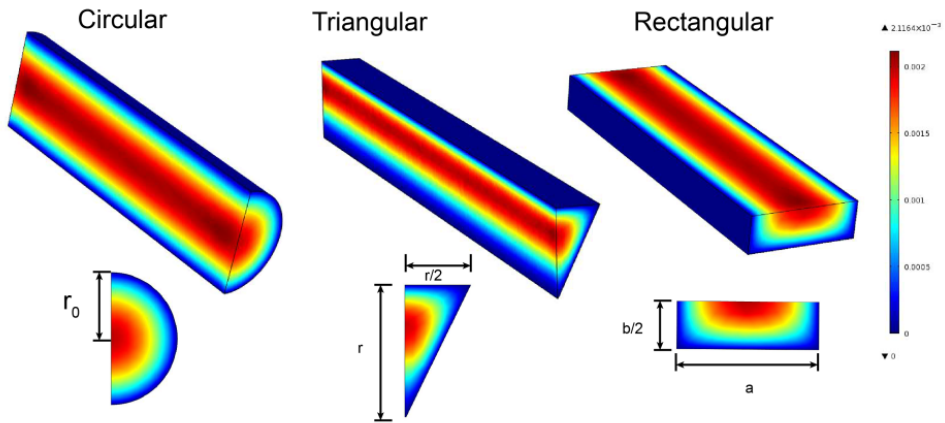


Figure 3. Cross-sectional view through the symmetry plane of fully developed flow profiles in channels of different geometries. The size-variables of these three typical channels geometries have been chosen arbitrarily; noteworthy is how the flow is restricted in sharp corners, which is clearly seen in the triangular channel geometry. The data was acquired by computational fluid dynamic modeling using COMSOL Multiphysics 4.1.

By using the variables given in *Figure 3* we can calculate the resistances of several common channel cross sections.²⁷ For a channel of circular cross section the resistance is given by *Equation (7)*.

$$R = \frac{8\eta L}{\pi r_0^4} \quad (7)$$

There does not exist any analytical solution for a general triangle, however, for an equilateral triangle the resistance is given below in *Equation (8)*.

$$R = \frac{320\eta L}{\sqrt{3}r_0^4} \quad (8)$$

Channels with rectangular cross section such as those used in this work are given by

$$R = \frac{12\eta L}{ab^3} \left[1 - \frac{192b}{\pi^5 a} \sum_{i=1,3,5,\dots}^{\infty} \frac{\tanh(i\pi a/2b)}{i^5} \right] \quad (9)$$

The part within brackets of *Equation (9)* is visualized in *Figure 4*. The result is that for a square channel the factor equals around 0.42, giving that *Equation (9)* can be simplified to *Equation (10)*

$$R = \frac{29\eta L}{ab^3} \quad (10)$$

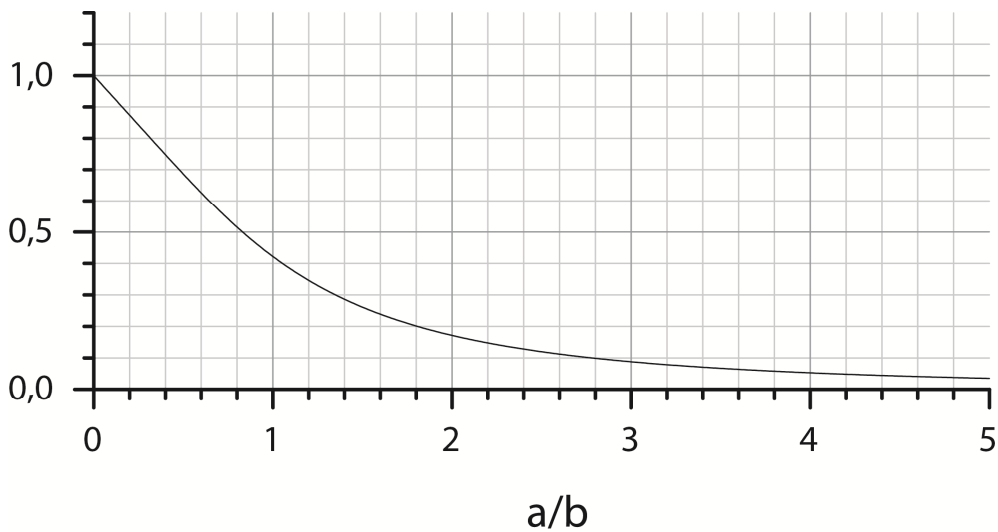


Figure 4 Plot showing the adjustment factor of a rectangular channel, expressed as a function of the width-to-height ratio. For a square channel the factor is ~ 0.42 .

For a rectangular channel with $w \geq 2h$ *Equation (9)* can be rewritten into *Equation (11)* with an error of less than 0.2%

$$R = \frac{12\eta L}{wh^3} \left(1 - 0.63 \frac{h}{w}\right)^{-1} \quad (11)$$

Solutions to several other, less common, symmetric cross-sections exist in the literature. However as a rough simple approximation, the flow resistance of channels of arbitrary shapes can be estimated by using the hydraulic diameter. This corresponds to how large a circular cross section has to be in order to have the same fluidic resistance as

the channel in question and it is given in *Equation (12)*, where A is the area of the cross section and P_{wet} is the wetted perimeter, the boundary, of the cross section.

$$D_h = \frac{4A}{P_{wet}} \quad (12)$$

Due to the inherent difficulties of characterizing the flow from the aforementioned governing equations several dimensionless numbers relating to the ratio between different variables are used to give an estimate of a particular situation. One of these dimensionless numbers is the Reynolds number, Re . As has been shown before, it is given by

$$Re = \frac{\textit{inertial forces}}{\textit{viscous forces}} = \frac{uD_H\rho}{\eta} \quad (13)$$

where ρ is the density of the fluid, D_h is the hydraulic diameter, u is the characteristic velocity in the channel and η the dynamic viscosity of the fluid. The ratio is used to determine the flow behavior of a wide range of systems, from the modeling of air-plane wings to estimating the flow regime in microfluidic channels. The transition from laminar to turbulent flow has been found to vary depending on factors such as aspect ratio and surface roughness, however generally this is said to occur at a Reynolds number of around 800-2000. Due to the small length scales in microfluidics it is common to operate at Reynolds numbers less than 1, indicating a flow dominated by viscous forces without turbulent characteristics. Exceptions such as inertial microfluidics exist where an elevated Reynolds number is necessary for operation of the devices.¹³

A fluidic system is often comprised of several elements with different hydraulic diameters. One common example of a situation where this occurs is when an inlet reservoir is connected to a channel. In this case

the flow profile of the fluid in the reservoir will be altered when entering the narrow channel and it will require some time before it fully adapts to the new size-constraint with a new parabolic flow profile as a result. The distance which the flow travels during this adaption time is called the entrance length and it is defined as the point where the developing centerline velocity is equal to 0.99 times its fully developed value. Deviations from parabolic flow can be of importance in DLD devices, as will be shown later. For low Reynolds numbers this length is given by

$$Le = D_h \left(\frac{0.6}{1 + 0.035Re_{D_h}} + 0.056Re_{D_h} \right) \quad (14)$$

where Re_{D_h} is the Reynolds number based on the hydraulic diameter. One can note that when Re_{D_h} is around 1 or below the entrance length will approach 0.6 times the hydraulic diameter.

Typically, the fluid flow in microfluidic channel is considered to be subject to a no-slip boundary condition. This results in a hydraulic resistance, which is dependent on both the perimeter and the cross-sectional area and taken into account through a correction factor, *Equation (15)*.

$$\alpha = \frac{A^2}{\eta L} R_{hyd} \quad (15)$$

Here, A is the cross sectional area, η the fluid dynamic viscosity and L the channel length. It has been shown that the correction factor depends linearly on the compactness number^{30, 31}, C , (16). Here, P is the perimeter and A the cross sectional area. This dependence shows the great impact of the high surface area-to-volume ratio in microfluidics. It also gives an easy way to estimate different channel types.

$$C \equiv \frac{P^2}{A} \quad (16)$$

2.2 Diffusion

The small characteristic length scales in microfluidics make diffusion a significant factor when constructing a system. Diffusion is due to the Brownian motion of the particle and is damped due to Stokes drag force. The mean square displacement for a spherical particle due to diffusion is given in (17) where n denotes the number of dimensions in which the diffusion is allowed to act, t is the time and D is the diffusion constant.

$$\langle x \rangle^2 = 2nDt \quad (17)$$

The diffusion constant is given by the Stokes-Einstein equation, Equation

(18), where k_B is Boltzmann's constant, T is the absolute temperature, r is the radius of the particle and η is the viscosity of the surrounding medium.

$$D = \frac{k_B T}{6\pi r \eta} \quad (18)$$

By combining Equation (17) and (18) the root-mean-square (RMS) distances that spherical particles of sizes relevant to microfluidics diffuse within a certain time can be calculated, these distances are given in Table 1.

Table 1 RMS of distance travelled due to Brownian motion of spherical particles of different sizes for different times in low Reynolds number flow.

Particle size	Time of diffusion	1 s	10 s	100 s	1000 s
10 nm		6.6 μm	21 μm	66 μm	210 μm
100 nm		2.1 μm	6.6 μm	21 μm	66 μm
1 μm		660 nm	2.1 μm	6.6 μm	21 μm
10 μm		210 nm	660 nm	2.1 μm	6.6 μm
100 μm		66 nm	210 nm	660 nm	2.1 μm

In general, diffusion can be said to be of an effect which needs to be taken into consideration when the sample consists of particles on the size scale of 1 μm or smaller. For a 1 μm particle it takes only a few seconds to diffuse a distance equal to its own size. Of course, if the residence time of a particle in a specific microfluidic device or channel is longer, the total effect of diffusion is increased. This is something that is taken into consideration in the dimensionless Péclet number which describes the relationship between convection and diffusion in terms of the time it takes to move a specific distance by radial diffusion and axial convection.

$$Pe \equiv \frac{\text{diffusion time}}{\text{convection time}} = \frac{l^2/D}{l/u} = \frac{lu}{D} \quad (19)$$

where l is the characteristic length, u is the characteristic velocity and D is the above described diffusion constant, Equation (18).

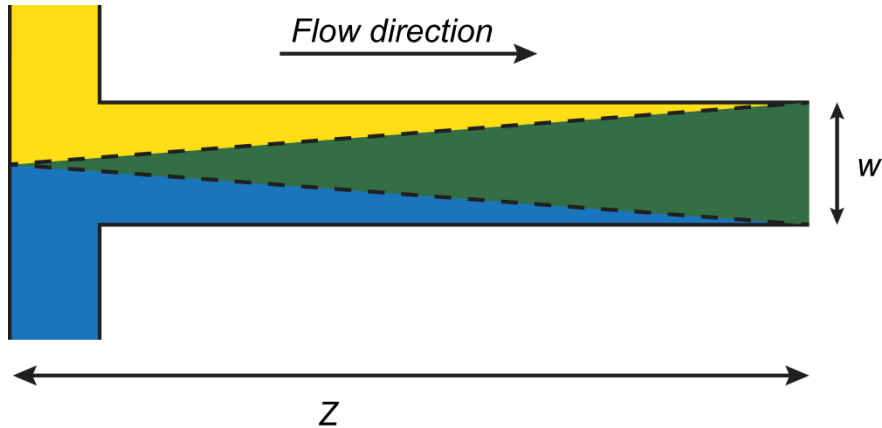


Figure 5. Mixing of fluids in microfluidic channels can sometimes be a challenge due to the absence of vorticity. Conversely, in many particle separation methods diffusion is something undesirable as it leads to a stochastic effect which suppresses separation of the entities in the sample.

The Péclet number can be described by visualizing the mixing of two co-flowing fluids, **Figure 5**. The width of the mixing zone grows by time and is given by

$$\delta = \sqrt{2Dt} \quad (20)$$

Complete mixing occurs when the mean diffusion distance is half the channel width. The time required can be calculated as follows, *Equation (21)*.

$$\delta = w \leftrightarrow t \sim \frac{l^2}{D} \quad (21)$$

During this time the fluid has moved a distance equal to

$$Z = ut \sim u \frac{l^2}{D} \quad (22)$$

this gives a ratio between convection and diffusion of

$$\frac{Z}{l} \sim \frac{u}{l} \frac{l^2}{D} = \frac{ul}{D} \equiv Pe \quad (23)$$

For a small protein in a 100 μm wide channel at a characteristic flow speed of 100 $\mu\text{m}\cdot\text{s}^{-1}$ the Péclet number would be 250, meaning that the mixing would need to occur over a length of 25 mm and it would take 4 minutes until complete mixing.

Sometimes diffusion is desirable and sometimes careful measures are taken to suppress the effect of diffusion as far as possible. As has been shown, in the case of mixing of liquids in microchannels the laminar nature of the flow in combination with the slow progress of diffusion will often require very long mixing times. Methods to decrease mixing times by inducing vorticity include the use of herringbone structures³², serpentine channels³³ and active chaotic mixing³⁴. Several other applications also completely rely on diffusion, such as the particle separation technique known as H-filter and its analytical counterpart, the T-sensor^{20, 35}. In general, however, the stochastic nature of diffusion acts to decrease resolution during particle separation. This is one aspect where the DLD technique is advantageous. As it is a passive and continuous separation technique increasing the flow rate, within "reasonable" limits (which will be discussed below), will increase the Péclet number and suppress diffusion acting to increase the separation efficiency. However, if the flow speed is increased a great amount, it will increase the Reynolds number and eventually reach a point where the flow shift to become turbulent. Further, shear forces at these very high flow speeds could act to distort the particles, depending on their deformability. This can both be a benefit or a drawback, depending on the sample to be sorted. This will be discussed further in *Chapter 6* and *7* and showed experimentally in *Chapter 8* during the analysis of RBCs in DLD devices at varying flow speeds.

3. Deterministic Lateral Displacement

The microfluidic particle-separation technique Deterministic lateral displacement (DLD) was first described by Huang *et al* in 2004¹⁵ where separation of spherical micrometer-sized beads with a resolution on the order of 10 nm was achieved. DLD has since been shown to be able to sort many different types of particles in a broad range of sizes from around 70 nm¹⁶ to 40 μm ¹⁷ in microfluidic devices to a few millimeter in macroscopic DLD devices³⁶. DLD devices consist of large symmetric post arrays, see *Figure 6A*, and take advantage of the laminar flow often present in microfluidic channels. By modifying the amount each row of posts is shifted with respect to the preceding row and the distance between two posts of the same row, flow streams with specific widths can be created and this will act to exclude the hydrodynamic center of particles above a certain size from residing in the flow stream closest to a post. This concept is illustrated in *Figure 6* where the smaller green particle is able to fit inside a flow stream and will hence follow this specific stream throughout its journey through the device, resulting in a lateral position at the end of the device identical to its initial lateral position. However, the larger red particle is not able to fit in the flow stream at the narrowest point between two posts (which could be seen as the decision point). It is therefore laterally displaced into the neighboring flow stream for each row. This lateral displacement forms the basis for the separation and as a consequence, it is what has given the technique its name.

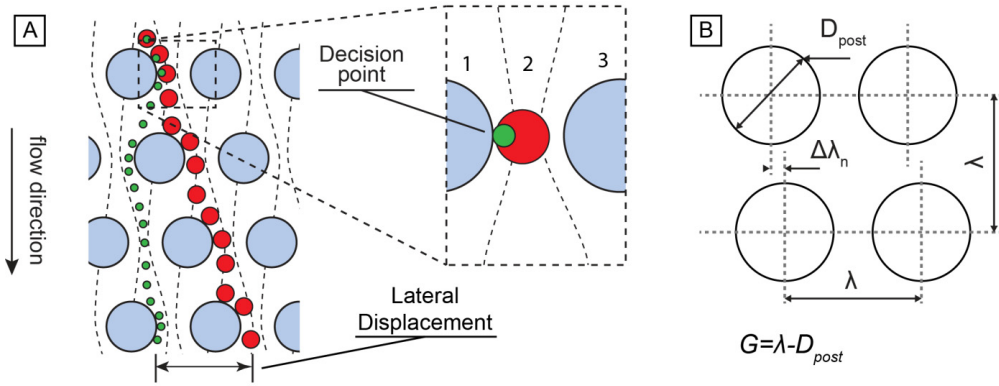


Figure 6. An illustration of size-based separation in a DLD device, (A) with the red particles being larger than the critical diameter of the device, while the green particles have a size smaller than the critical diameter. In the close-up of the narrowest point in the device, or the decision point for which trajectory a particle will reside in, it can be seen how the larger red particle is unable to continue its path through the device in the first flow stream and is laterally displaced into the second flow stream. This displacement will be repeated continuously for each row in the device. (B) A rhombic unit cell within the post array showing the parameters important for sorting of particles.

3.1 Theory

A more detailed view of the basis of the size-based particle separation in a DLD device is shown in *Figure 7*. Two different devices are shown with red particles of the same size. In *Figure 7A* the particles follow the overall fluid flow while the particles of the same size are laterally displaced in each row in *Figure 7C*. The arrays are identical except that they differ by the amount with which each row is displaced with respect to its preceding row. By using the notations given in *Figure 6B* we can define the period of the array as

$$N \equiv \frac{\lambda}{\Delta\lambda} \quad (24)$$

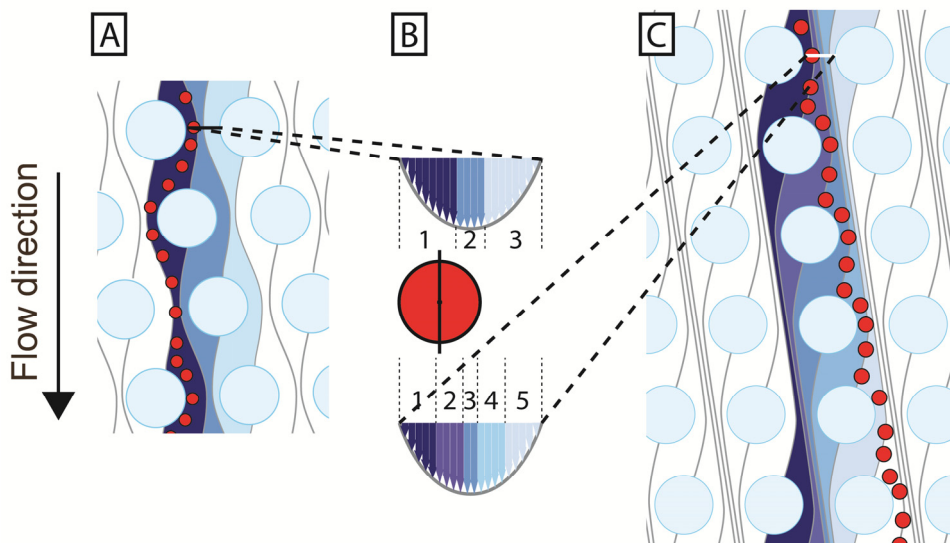


Figure 7. Illustration of how changes in array designs result in a different critical diameter. Two arrays are shown with identical designs except for the period of the array. The array in (A) has a period of $N=3$ while the array in (C) has a period of $N=5$. (B) The increase in period result in a smaller volume fraction being bifurcated at each row and consequently flow streams will be narrower, acting to exclude particles of smaller sizes.

The periods of the devices in *Figure 7A* and *7C* are $N=3$ and $N=5$ respectively. This means that the flow streams are aligned with respect to their initial position after this number of rows, as can be seen. Consequently, for each row in the device a volume fraction equaling $1/N$ th of the total flow is diverted and displaced to the neighboring gap. After N number of rows the flow streams are back to their original lateral position. By varying the period (and the resulting volume fraction being diverted at each row) different widths of the flow streams can be achieved. This is also illustrated in *Figure 7B* where the parabolic flow profiles (PFPs) are shown with the respective widths of the flow streams. The black vertical line of the red particle is drawn through its hydrodynamic center. It can be seen how the center of the particle is able to reside in the first flow stream of the $N=3$ device in *Figure 7A*, meaning that the particle is able to follow this stream throughout the entire array in what is known as zigzag mode. The particle is however too large to fit in the first flow stream of the device in *Figure 7C*, and consequently, at every decision point it will be

laterally displaced into the adjacent flow stream and will travel through the array in bump mode.

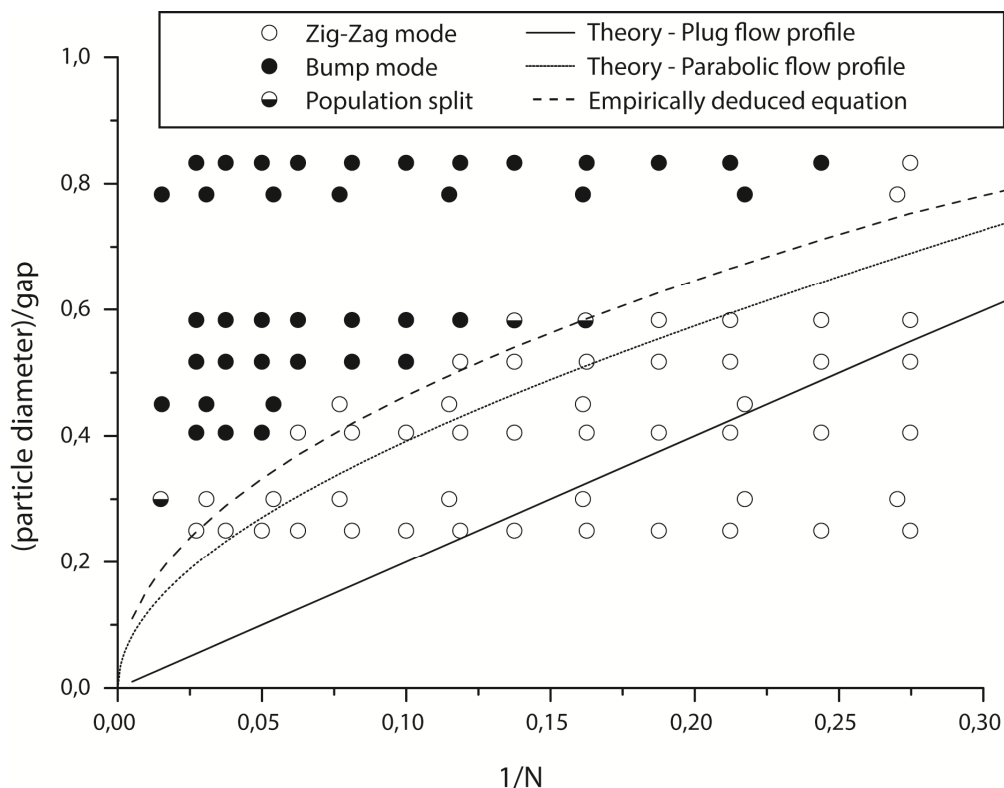


Figure 8. Our own experimental data on the transition between different types of trajectories for different normalized particle sizes as a function of the inverse periodicity of the device. The lines represent the theoretical values for both plug flow and parabolic flow as well as the empirically deduced value used for constructing the devices used herein³⁷

The cut-off size at which the transition from zigzag mode to bump mode occurs is known as the critical diameter, D_c , and corresponds to twice the width of the first flow stream. The critical diameter is a function of the period of the array, as has been shown, and also the distance between posts, *i.e.* the gap (G in *Figure 6B*). This is illustrated in *Figure 8* where we characterize the exact behavior of our particular devices with a method analogous to what has been reported by Inglis *et al.*³⁸. Experimental data points from measurements in our devices are plotted as particle diameter divided by gap over the inverse period.

Both the theoretical values for plug flow and parabolic flow³⁹ has been plotted in the graph and one can note the large discrepancy. The empirically deduced formula³⁷, (25), was used to construct the devices used within this thesis and can be seen to be much close to the parabolic flow theory than plug flow theory.

$$D_c = 1.4 \cdot G \cdot N^{-0.48} \quad (25)$$

As can be seen, this theoretically deduced formula results in an expected critical diameter which is even larger than the parabolic flow theory; this could be a result of the large *particle-to-gap* ratio acting to induce flow disturbances interfering with the symmetry of the flow field.

In the above we have described DLD as a technique that gives rise to a binary separation. It has however been shown by the Tegenfeldt group⁴⁰ and the Drazer group^{36, 41} that in the general case for non-integer periodicities up to four different trajectories are possible, a technique which with correct chosen array parameters would act to decrease the device length considerably and, consequently, the time needed to separate a specific sample.

3.2 Flow simulations

To evaluate the flow in DLD arrays, Computational Fluid Dynamics (CFD) simulations were carried out using COMSOL Multiphysics 4.0 (COMSOL, Inc., Burlington, USA), a software package based on the finite element method (FEM) to approximate the partial differential equations of any fluid dynamic problem. This provides the ability to evaluate any device design without the need of manufacturing an actual prototype, saving a great amount of time that would be spent on processing of masks, molds and devices followed by experimental analysis.

However, CFD analysis often requires an immense amount of computational power. The common computers of today are simply not powerful enough to be able to analyze larger microfluidic systems at a satisfactory level of resolution. What is often done is to simplify the structure to be analyzed. For the large symmetric DLD post arrays a rhombic unit cell can be constructed, as shown in *Figure 9*. The model takes use of periodic boundary conditions to connect the two pairs of opposite channel boundaries. Further, there is a compensation to allow for $1/N$ of the total flow to be bifurcated at each row. To additionally decrease the calculations needed, a symmetry plane in the z -direction at half the channel height is used.

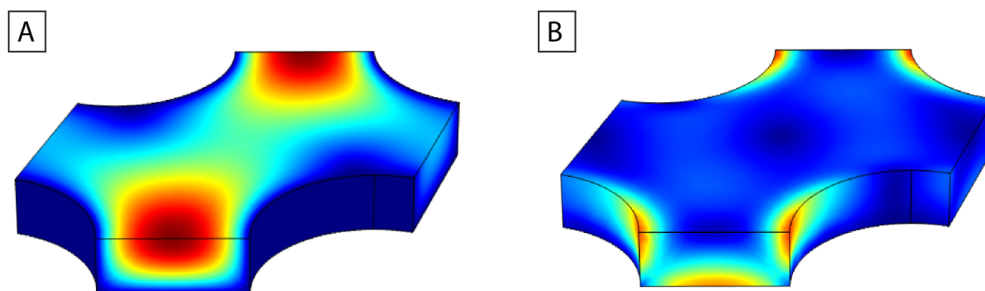


Figure 9. The result of a CFD simulation of a single rhombic unit cell within the post array. The model takes use of periodic boundary conditions to connect the two pairs of opposite channel boundaries, e.g. the flow leaving the unit cell to the left enters the same unit cell from the right, with matching flow profiles. A symmetry plane is used in the z -direction at half the channel height to additionally decrease the computation needed. This unit cell is similar to the actual design used in this project; the post diameter is $20\ \mu\text{m}$ with a gap size of $12\ \mu\text{m}$. In the particular analysis from where the images was extracted the period is 3 and the channel depth is $10\ \mu\text{m}$. (A) is showing the flow velocity distribution while (B) is showing the shear stress which act to distort deformable particles, decreasing their effective size at high flow rates.

The simulations done herein are used to give an estimate of the flow behavior and critical diameters in different designs of the device. This was done by investigating the impact of the post radius, the period, the particle's depth position in the unit cell and also the flow speed. The flow profiles of the CFD solution were thereafter analyzed to achieve the resulting critical diameter at the specific condition; the results are shown in *Figure 10* and *Table 2*.

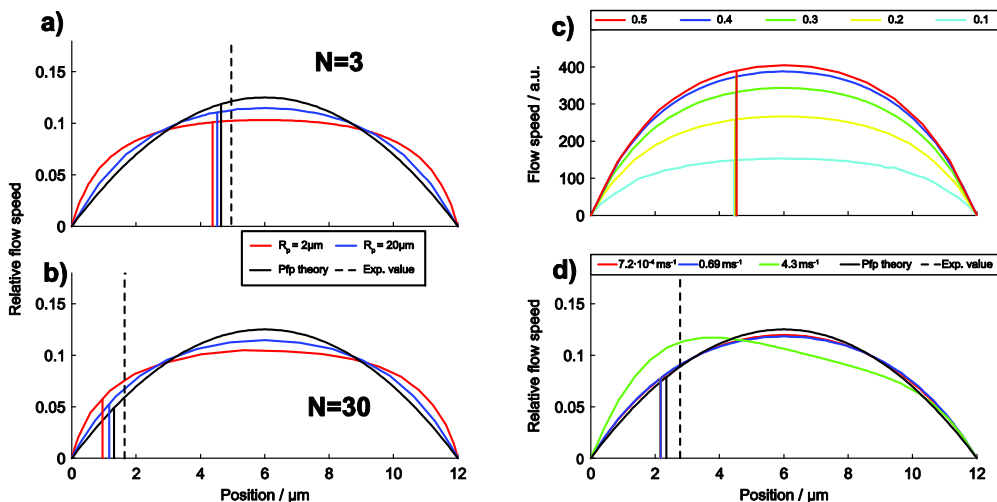


Figure 10. Flow profiles at the gap between two posts. The gaps and channel heights are constant ($12\mu\text{m}$ and $10\mu\text{m}$ respectively) while the periods, post radii and flow speeds are varied. (a) and (b) show comparisons between a period of 3 and a period of 30 respectively. The flow speeds are low enough to ensure laminar flow. In both graphs the flow profiles of arrays with post sizes of $2\mu\text{m}$ and $20\mu\text{m}$ is shown along with a theoretical parabolic flow profile. The corresponding critical radii are indicated by vertical lines such that the area bound by the curve and to the left of these lines is a fraction $1/N$ of the total area under the curve. Dashed lines represent values given by Eq. 16. It can be seen how smaller posts makes the flow profile adapt more to a plug-like flow than a parabolic flow profile, and as a consequence, the critical diameter decreases. (c) shows the flow profile of $N=3$ measured at different depths, from 0.1 to 0.5 of the total channel depth. These graphs have, unlike the rest, not been normalized, however the different R_c coincide closely. This shows how the separation of particles is not affected by its position along the normal direction of the device. (d) shows an array with $N=10$, $PR=10\mu\text{m}$ at varying flow speeds. The flow profiles at speeds below 0.69ms^{-1} coincide closely while higher flow speeds results in changed flow profiles indicating that a transition from laminar flow to turbulent flow has occurred. In the simulation the critical diameter decreases due to the transition from laminar to turbulent flow, however, the simulation should not result in a period flow in the array and consequently a precise critical diameter should not be possible to simulate under chaotic flow.

The simulations presented herein were all carried out on arrays with a gap of $12\mu\text{m}$ and a depth of $10\mu\text{m}$ while the periods, post radii and flow speeds were varied as noted in the graphs. Simplifications in the model include the finite mesh size and incompressible fluid. In all of the graphs except *Figure 10C* the flow profiles have been normalized to make comparison easier. *Figure 10A* and *Figure 10B* shows how the flow profiles are affected to a larger extent by the post radii than by the period in the array. The different curves are for post diameter of $2\mu\text{m}$

and 20 μm and also an ideal parabolic flow profile. Changing the period does not significantly affect the flow profile under these laminar conditions in this model. The change due to post radii is likely to be an effect of the entrance effects mentioned in *Section 2.1*, where the flow profile needs time to adapt to a change in channel size. Between two rows of posts there are no obstacles to interfere with the flow making the only constraints the side-walls of the array itself. A more uniform, plug-like, flow profile is therefore favored which subsequently has to be confined within the gap of the next row. Depending on the post radii and flow speed this process is allowed different times. As can be seen, the resulting flow profile of posts with the larger diameter, 20 μm , more closely resembles the parabolic flow profile.

Table 2. Result of the CFD Simulation, evaluation of critical diameter in a DLD device

post diameter (μm)	period	derived D_c (μm)
2	3	8.74
20	3	9.04
PFP theory	3	9.28
2	30	1.9
20	30	2.32
PFP theory	30	2.62

Figure 10C shows an evaluation of the critical diameter as a function of the depth position in the device. The evaluation shows a very small deviation in the critical diameter between the distribution acquired at the lowest position, 1 μm from the channel bottom, and the one acquired at center of the channel, at a depth of 5 μm . The resulting critical diameters were $D_{c,1}=8.91 \mu\text{m}$, $D_{c,2}=8.97 \mu\text{m}$, $D_{c,3}=9.02 \mu\text{m}$, $D_{c,4}=9.04 \mu\text{m}$ and $D_{c,5}=9.05 \mu\text{m}$ respectively. These small deviations could very well be introduced by the finite mesh grid and could be investigated in future studies by varying the mesh definitions, however, this would require very powerful computers.

3.3 Device design

The optimum design of a DLD device depends strongly on its final application, for example, depending on whether the goal is to achieve separation or enrichment of particles. Also factors such as the size-range of the particles present in the sample and any size restrictions to the final device will all be needed to be weighed in when determining the final device design.

For separation of particles in a DLD device there are generally three types of categories of device designs, which are shown in *Figure 11*. They all have their respective benefits and drawbacks, as noted in the figure, and careful consideration has to be given to what application the device is intended for. Multiple inlet devices, for example, can take advantage of a secondary particle-free stream to which the particles to be separated, blue in this example, can be steered and as a consequence the background particles in the purified fraction will be minimized. An enrichment-separation device can be achieved using two steps where the first one deploys a small critical diameter acting to enrich all particles in the sample into a narrow stream close to the side of the channel. This is followed by a section with the reverse displacement direction and a critical diameter larger than the background particles resulting in a lateral displacement of only the desired particles. This device would only utilize a single inlet, negating the need for advanced pressure control (which most likely a multiple inlet device would need), and still achieve a high sensitivity. However the throughput would be decreased while the device length would be increased.

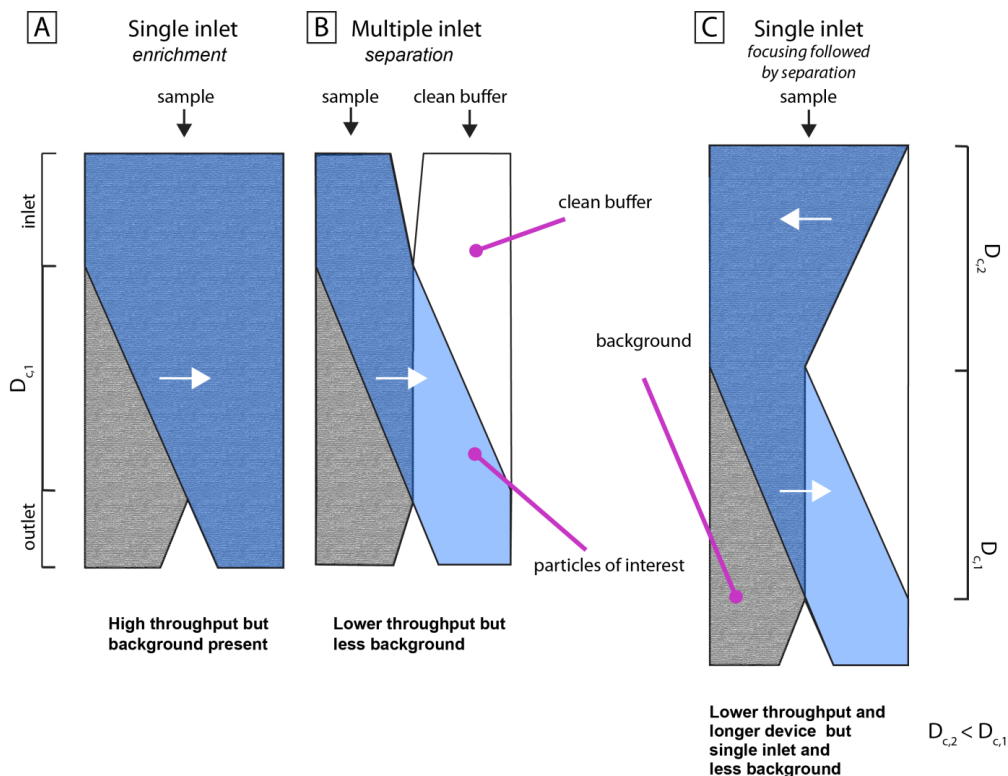


Figure 11. Different designs of DLD devices to achieve particle separation. The desired particles are colored blue while the background is gray. Every design has its specific advantage and drawbacks as shown in the figure. Careful consideration needs to be taken depending on what properties are important to the final application.

Instead of utilizing a single critical diameter, DLD devices often have several critical diameters, see *Figure 12*. This extends the simple binary separation to the possibility of achieving multiple fractions at the end of the device. The benefit could solely be to separate different types of particles having different sizes. But it could also be a powerful tool in the case where one does not have information about the particle sizes. By analyzing them in a device of multiple critical diameters one would obtain the distribution of particle sizes present. This could be a typical scenario for a diagnostic microfluidic device aimed at detecting pathological changes to the morphology of blood cells.⁴² With several critical diameters one would obtain a vast amount of additional information, the exact distribution of particles present, and would have the ability to draw specific conclusions about the state of the patient as

different diseases has been shown to affect blood cell differently.⁴³ Techniques of dynamically adjusting the critical diameter in a DLD device has shown great promise^{44, 45}, but, depending on the final application, it could be difficult to implement.

A static device with several critical diameters can be constructed by either having an array of varying periods or varying the gap size (or a combination of the two) as can be seen in *Equation (25)*. Decreasing the gap size to achieve a lower critical diameter might require some modifications of the design to take care of any particles which are too large to enter the proceeding section. Often, extra outlets are constructed into which these large cells can be guided, as exemplified by Inglis *et al.*⁴⁶ These extra outlets will need to be carefully designed in order to receive the same pressure drop as the remaining array in order to maintain the symmetric flow.

A device which only varies the period would be simpler to construct and operate due to the lower sensitivity to pressure differences between the different outlets. However, the size range of particles which can be sorted, or dynamic range of the device, would be decreased.

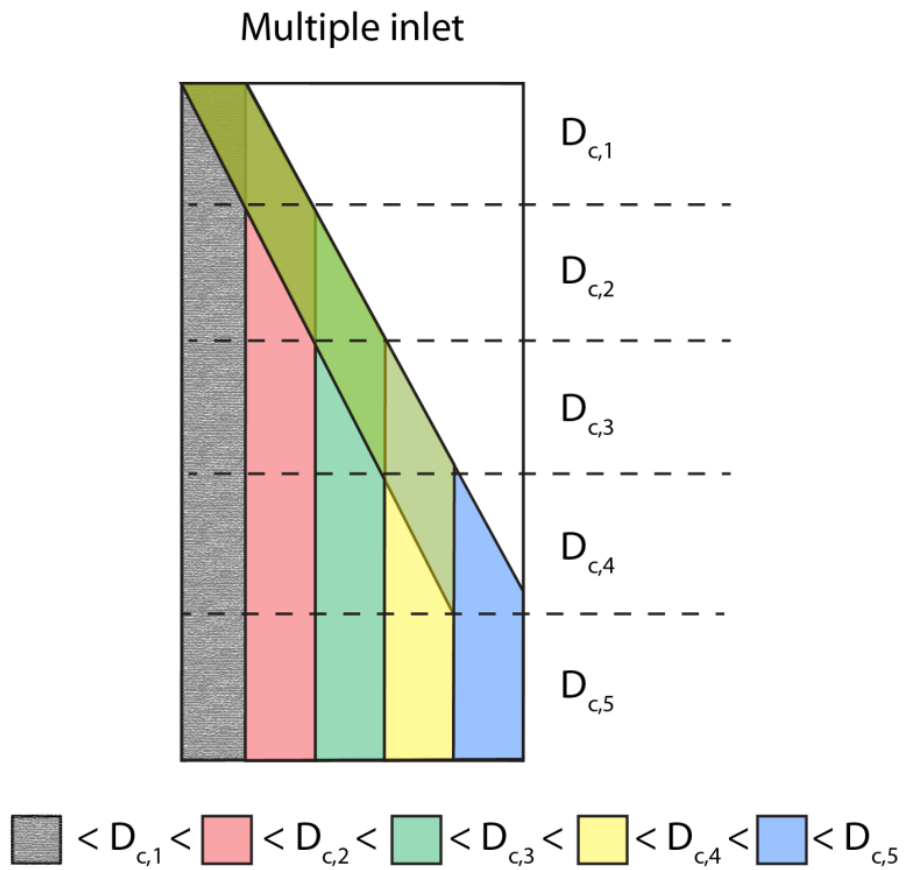


Figure 12. DLD device of several critical diameters making possible the fractionation of a sample containing particles of several different sizes. The change in critical diameter can be induced by either decreasing the gap size or the period. Changing the gap size would result in a greater dynamic range of the device, but on the other hand it would require a more advanced design in order to sort out any particles larger than the proceeding region.

3.4 Dynamic range

The particles which can be analyzed in a specific device, or the dynamic range of the device, can be illustrated by considering the fractionation of a sample consisting of three different spherical particles: $1\mu\text{m}$, $3\mu\text{m}$ and $20\mu\text{m}$ in diameter.

The device could either be one of decreasing gaps or decreasing period, in both cases there needs to be two different critical diameters

such that $20\mu\text{m} > D_{c1} > 3\mu\text{m} > D_{c2} > 1\mu\text{m}$. If the gap size is constant throughout the device, it would need to be larger than any particle present in the sample. However with a constant period the gap size can be altered after sorting out the largest particles in the sample. The benefit of decreasing the gap after sorting out the largest particles can be shown by rewriting *Equation (25)* to reflect the period, or number of rows, needed to obtain a certain critical diameter with a specific gap.

$$N = \left(\frac{1.4G}{D_c}\right)^{\frac{1}{0.48}} \quad (26)$$

The length of this section is hence given by

$$L_s = \lambda \cdot N = \lambda \cdot \left(\frac{1.4G}{D_c}\right)^{\frac{1}{0.48}} \quad (27)$$

This is illustrated in *Figure 7* where the relative lengths are shown as a function of the gap-to-critical diameter ratio.

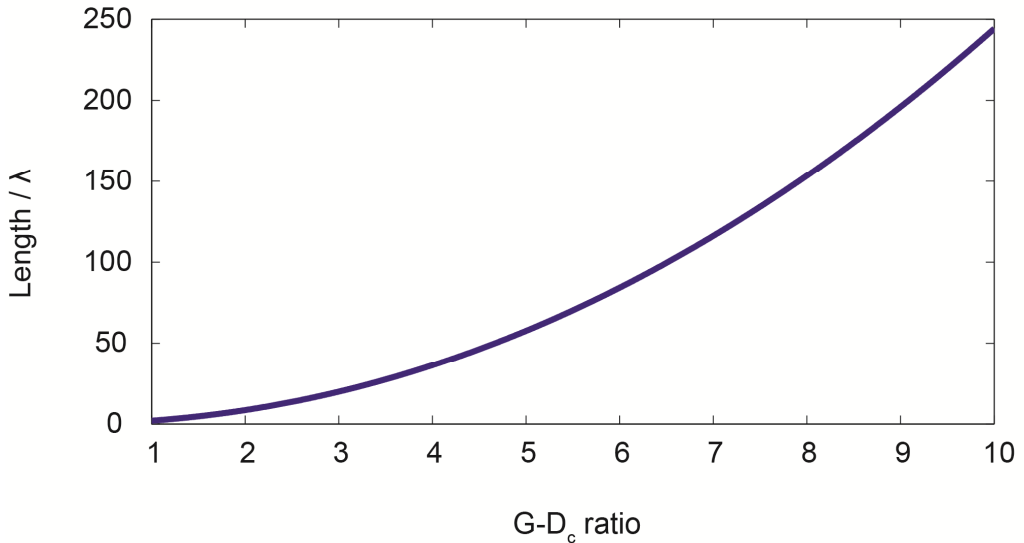


Figure 13. Length of one period as a function of the gap-to-critical diameter ratio. The exponential growth together with stochastic processes such as diffusion generally results in a maximum G-D_c ratio of around 6, equaling a period length of almost 80.

As can be seen in *Figure 13* the period needed to laterally displace the particles with a size above the critical diameter a distance of one λ from its initial lateral position increases roughly as the square with the gap-to-critical-diameter ratio. What should be noted is that an increased gap size not only increases the period, but it will also increase λ making the square scaling of the length in terms of the number of λ result in a cubic scaling in terms of the absolute numbers. In the specific case of separating the sample mentioned earlier appropriate parameters for a DLD device with multiple arrays of varying gap could be $D_{c,1}=15\ \mu\text{m}$, $D_{c,2}=2\ \mu\text{m}$, $G_1=25\ \mu\text{m}$, $G_2=5\ \mu\text{m}$, $P=20\ \mu\text{m}$. When comparing the lengths of this device of varying gap with a device of varying period, one can note that the first array in both devices have the same parameters and both would be equal in length, $263\ \mu\text{m}$ per period. The second section would however differ significantly due to the different G -to- D_c ratios. The device with a constant gap would be $17\ 500\ \mu\text{m}$ per section while the device with a smaller gap would accomplish the same separation in $340\ \mu\text{m}$, less than $1/50$ of a device with varying period. A short array length is beneficial not only to overcome any size restrictions in the processing steps during manufacturing, but also a shorter device would decrease the significance of diffusion and increase the throughput.

The strong dependence between device length and Gap -to- D_c ratio imposes a limit on the dynamic range of the device. Even though devices with large N have been shown,¹⁶ the separation efficiency at these high periods are severely limited due to the stochastic diffusion acting to suppress the performance of the device. This effect can be shown by considering that the Péclet number, discussed in *Chapter 2*, scales as $Pe \propto \frac{1}{N^2}$. Consequently, a period of around 50 is generally considered to be a good rule of thumb for the maximum period.^{37,39} At the same time, the particles need to be small enough to not only avoid clogging of the device but also avoid larger disturbance of the symmetric flow. This can be estimated to around $N=4$. With $N=50$ equaling a critical diameter of around $0.15 \cdot G$ while $N=4$ gives $0.51 \cdot G$

the maximum dynamic range of a DLD device of varying period, or chirped DLD device, would therefore be around 3.4. The work by Louthback *et al.* addressed this issue by utilizing an array of triangular posts,⁴⁷ acting to alter the parabolic flow profile to achieve a lower critical diameter with the same period. Further, Beech *et al.*⁴⁴ utilized dielectrophoresis to increase the dynamic range of DLD devices. This method would also be sensitive to the particles inherent dielectrophoretic properties, which could further allow for separation of otherwise indistinguishable particles or be used to orient the particle for shape-based sorting.

For the work presented herein, the chirped device design with a constant gap and varying period was chosen due to its simpler design and handling. To be able to analyze a wide range of particle sizes, three separate devices were manufactured as will be further discussed in *Chapter 6*.

3.5 Sorting based on shape

As mentioned above DLD, together with other microfluidic particle sorting techniques (discussed in *Chapter 1*) have been shown to be able to separate particles based on size. However, as biological particles come in many different forms, in many cases the sample often involves more complex particles with non-spherical shapes. Separation based on size alone, would not be able to discriminate between cells with small differences in shape. The separation of cells of complex shapes in a DLD device is one example. *Figure 14A* shows four different particles which all have the same length of their smallest dimension. It is known that the shear fields of the fluid flow act to minimize the particles' effective size in passive hydrodynamic separation techniques⁶. It would therefore be difficult to discriminate between the particles shown in the figure in a conventional DLD.

Recently Beech *et al.* showed how the disc-shaped RBCs, behaved differently in a deep and a shallow DLD device, opening up for separation based on shape⁴⁸. This work presents the continued

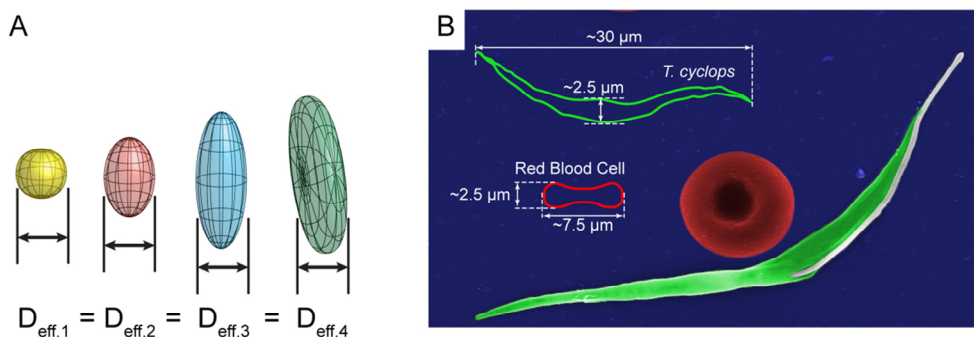


Figure 14. (A) Particles of different shapes but with the length of their smallest dimension in common. In a conventional DLD device with only size-based particle separation, the shear field of the fluid would act to align the particles against the pillars and hence the resulting effective size of the different particles would be equal with little or no separation as a result. (B) For the diagnosis of sleeping sickness the separation of RBCs and trypanosome parasite is crucial. Shown is an SEM micrograph of an RBC and the trypanosome parasite used herein, *T. cyclops*. The illustration shows how these two cells both share their common smallest diameter making separation in a traditional DLD device difficult. From reference¹ - Reproduced by permission of The Royal Society of Chemistry.

investigation of this behavior and also the application of this effect to the specific case of separating parasites from human blood, a task which would be very inefficient in a conventional DLD device separating on size alone. As with the particles exemplified in *Figure 14A*, the smallest dimension of the RBCs is very similar to the smallest dimension of the trypanosome parasite, which causes HAT, *Figure 14B*. The RBC, which is the cell in focus for separation as it accounts for ~98% of the blood cells, has a biconcave shape approximately 7.5 μm in diameter with a thickness of 2.5 μm. The trypanosome parasite has the same thickness; however, it has a long slender, worm-like body approximately 30 μm in length.

3.6 Existing shape-sensitive sorting devices

The great advantage with shape-based particle sorting is not hard to comprehend, extending the traditional size-based sorting to also

include non-spherical particles would provide an additional parameter which can be used to either extract information about the particles in an analytical device or to open up for novel separation schemes in a preparative device. These advantages have resulted in a great interest in shape-based sorting recently. A few successful attempts have been made to separate particle based on shape. Sugaya *et al.*⁴⁹ recently showed how single spherical particles could be distinguished from twins or triplets of the same spherical particles. The work was based on hydrodynamic filtration which like DLD devices discriminate particles based on if they are able to fit within certain flow streams or not. The smallest dimension of the twins and triplets were similar to that of the single particles, however, by utilizing the rotation of non-symmetric particles as shown in *Figure 15*.

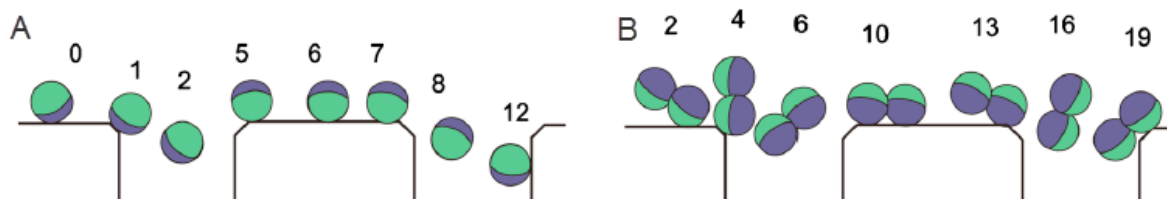


Figure 15. Illustration of the rotational behavior of spherical and non-spherical particles exploited by Sugaya *et al.*⁴⁹ to achieve separation based on shape. Even though both particle types share the same smallest dimension, separation could be achieved. Reprinted with permission from reference⁴⁹. Copyright 2011, American Institute of Physics.

The behavior of larger non-spherical particles were also studied by Hur *et al.*⁵⁰ Here, the behavior of particle focusing in straight channels at elevated Reynolds number was investigated. Different particle shapes and sizes were used and the particles' resulting lateral equilibrium position across the channel was found to be closely related to their rotational diameter but at the same time not affected by the particles' aspect ratios. The technique therefore has potential of being in use in sorting of non-spherical particles, but it would have difficulties in resolving the smallest dimension of, for example, an RBC. This dimension would be its thickness, and a change of this almost exclusively affects its size-ratio and not its rotational diameter.

However, the technique would have a great potential in resolving RBCs of different diameters as this would significantly affect the rotational diameter.

4. Human African Trypanosomiasis

A report from the World Health Organization (WHO) announced that 40 000 cases of Human African Trypanosomiasis (HAT) had been diagnosed in 1999⁵¹. This number stands in stark contrast to the estimated number of infections which, at the same time, was estimated to around half a million⁵² and still increasing in parts of the continent⁵³. This discrepancy is characteristic of HAT, which attacks the poorest countries of the poorest continent. Only around 3 million people of the 60 million at risk were either actively screened or had access to a health center where diagnostics and treatment were available. Apart from the shortened life expectancy in endemic areas the disease is estimated to cause damages worth \$4 billion annually⁵⁴. With this in mind it is not hard to see why HAT is considered one of the world's most neglected tropical diseases in urgent need of new tools for rapid, easy and cheap field detection in the rural areas of endemic foci.

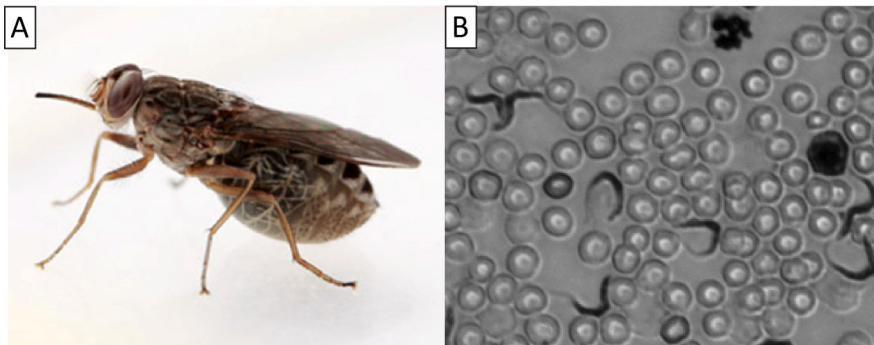


Figure 16. (A) Photograph of a tsetse fly, the vector of both variants of the HAT disease. With its size of 6-14 mm it largely resembles a normal house fly, however, the tsetse fly can be far from harmless depending on whether it is carrying the trypanosome parasites or not. Image used with permission from FAO/IAEA.⁵⁵ (B) Blood smear stained with Giemsa showing *T. brucei* parasites next to red and white blood cells. Used with permission from F. Giordani, University of Glasgow.

4.1 Variants

The disease is caused by one of the two forms of the inter-cellular protozoan parasites; *Trypanosoma brucei gambiense* or *Trypanosoma brucei rhodesiense*. Around 90% of the cases are believed to be caused by the West African version of the parasite *T. b. gambiense*⁵⁶. For this variant of the parasite, the disease progresses relatively slowly and as the symptoms can take several months to fully develop many infected individuals are simply not aware of the fact that they are infected with the parasite. The East African specie, *T. b. rhodesiense* gives rise to a disease which is characterized by a much faster disease progress, which is also likely to be the reason why the disease is not as prevalent as the West African strand. With infected individuals rapidly dying, the risk to spread the disease further will be lower.⁵⁷ The final stages of both these versions of HAT, or sleeping sickness (SS) as it often is referred to, consist of the central nervous system (CNS) being attacked giving rise to an almost constant state of unconsciousness. Both versions of HAT require rapid and correct diagnosis as the chances of survival decline rapidly as the disease progresses.

4.2 Endemic foci

Because the two different trypanosome subspecies share the common vector, the tsetse fly, the disease only occurs in areas where the tsetse fly is present. However, for reasons not known the opposite is not true, in some areas where the tsetse fly is found, the disease does not occur.⁵⁸ The black line in *Figure 17* depicts roughly the main areas of prevalence of the two different types. This segregation of the two strains is reflected in the commonly occurring names of their respective diseases: West African trypanosomiasis for the disease caused by *T. b. gambiense* while *T. b. rhodesiense* causes East African trypanosomiasis.

Actions have been taken in order to prevent the spread of the disease by trying to exterminate the tsetse fly vector. There have been some success in this project, such as in the island of Zanzibar.⁵⁹ With this

smaller area, the disease can more easily be controlled and the re-invasion pressure from surrounding areas is far less. In the mainland of Africa the disease is much more difficult to control and a complete eradication is unlikely. However, some progress has been reached locally with insecticide spraying from planes and use of baited traps with insecticides. Lately a project known as sterile insect technique (SIT) was launched. As female tsetse flies only mate once during their lifetime this project aims at controlling the spread by releasing a large number of male tsetse flies which has been rendered sterile by irradiation. These sterile tsetse flies will then compete in the wild with the natural tsetse fly and act to decrease tsetse populations.⁶⁰

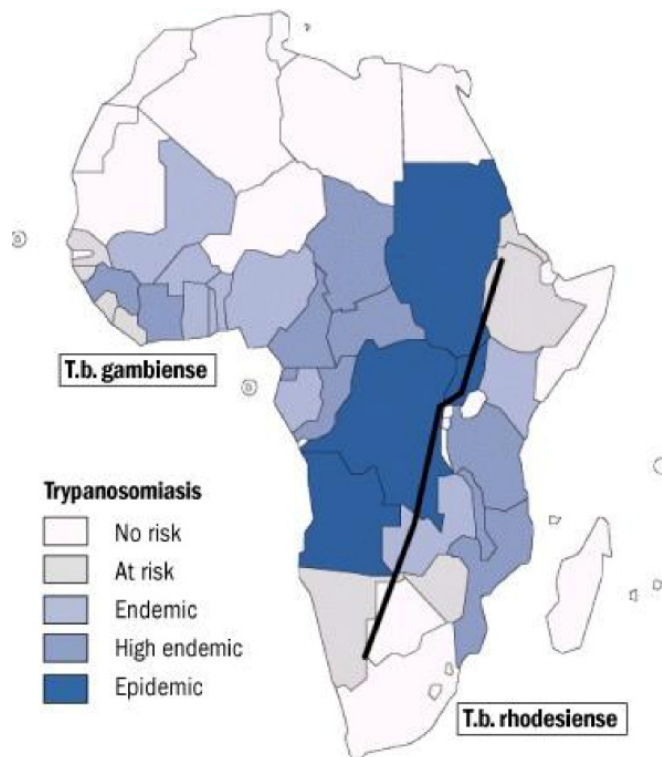


Figure 17. Map showing endemic areas of the two different strands of Human African Trypanosomiasis, *Trypanosoma brucei gambiense* and *Trypanosoma brucei rhodesiense*. It is estimated that 90 % of the infected individuals are infected by the West African *T. b. gambiense* strand. Image used with permission from World Health Organization⁶¹

4.3 Treatment

Treatment is dependent on whether the disease is in its first or second stage. The latter is characterized as having trypanosomes present in the central nervous system (CNS). In the first stage of the disease the patient is given Pentamidine (for West African- trypanosomiasis) or Suramin (for East African- trypanosomiasis). While in the second stage of the disease the patient is given Melarsoprol or Eflornithine. Out of these four drugs only Eflornithine has been developed in the last sixty years, again highlighting the disease status as a highly neglected disease. The first stage treatments are more effective and give slightly milder side effects compared to treatment during the second stage of the disease. Side effects are still severe, however, and are exemplified by a reported 1% mortality rate for the drug Pentamidine⁶². The most commonly used drug for second stage treatment has been Melarsoprol. This drug is an arsenic derivative and the treatment is basically a titration of this arsenic compound through the patient while hoping that the parasite die before the patient does. In fact reports are showing a mortality rates around 4-12 % due to this highly toxic treatment. The newer Eflornithine is believed to have a lower mortality rate but is not used in practice in the first line of treatment in most areas due to its high cost and difficulties related to administration of the drug.^{52, 58} These severe side effects provide a strong justification of the need for diagnosis during the first stage of the disease where milder treatments are available while suppressing false positives due to the harsh treatments.

Diagnosis of the disease relies on finding the parasite in the blood. However, to classify when the disease has progressed to the acute second stage with a need for a more severe treatment, the WHO has recommended that a positive diagnosis should be defined as one of the following: Trypanosomes in the cerebrospinal fluid (CSF), a white blood cell count over 5 cells/uL or a plasma protein concentration exceeding 370mg/L. The migration of trypanosomes across the blood brain barrier (BBB) is believed to be accomplished in an intricate way

facilitated by a cysteine protease. This enzyme which is expressed by the trypanosomes and acts to interfere with the oscillatory pattern of calcium ions in the endothelial tissue of the BBB leading to a disruption of their normal function allowing the trypanosomes to reach through to the CNS⁶³. The time to develop the second stage disease for *T. b. gambiense* is several months while, as discussed above, *T. b. rhodesiense* has a much faster progress with trypanosomes being detectable in the CSF after around two weeks.⁶⁴

4.4 Trypanosome life cycle

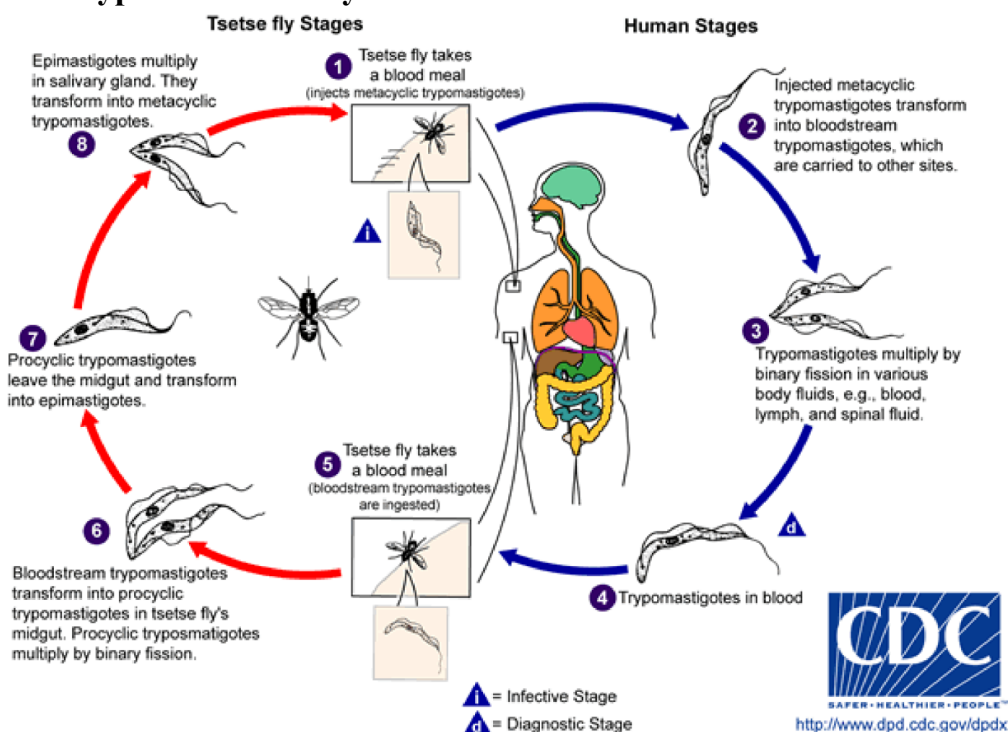


Figure 18. Life cycle of the *T. brucei* parasite. Left side of image shows the vector-based phase of the cycle while the right side is shows the host phase. Image used with permission from Centers for Disease Control and Prevention (CDC).⁶⁵

As shown in *Figure 18*, the life cycle of a trypanosome starts with an infected tsetse fly taking a blood meal of the host (1). The trypanosomes multiply subcutaneously at the site of entry for a few days, which in some cases gives rise to a visible large red sore on the skin, a chancre. The protozoan continues by entering the blood stream

and the lymphatic system in which it is distributed throughout the body (2). It multiplies through binary fission increasing its concentration (3). The spread of the disease may be continued by another tsetse fly taking a blood bite from the infected human (5). After subsequent multiplying in the midgut of the fly (6) the epimastigote form of the parasite is able to leave the midgut and travel to the salivary glands (7). Here they multiply further and are transformed back to their original trypomastigote form waiting to be transferred into a new host. (8). As shown, the trypanosome parasite is capable of surviving many harsh environments and can adapt easily to a new phase in their life cycle by transforming into another form.

4.5 Characteristics of *Trypanosoma brucei*

The morphology of *T. brucei* in the blood stream can vary considerably. Figure 4 shows four commonly occurring forms ranging from long and slender to short and stumpy.

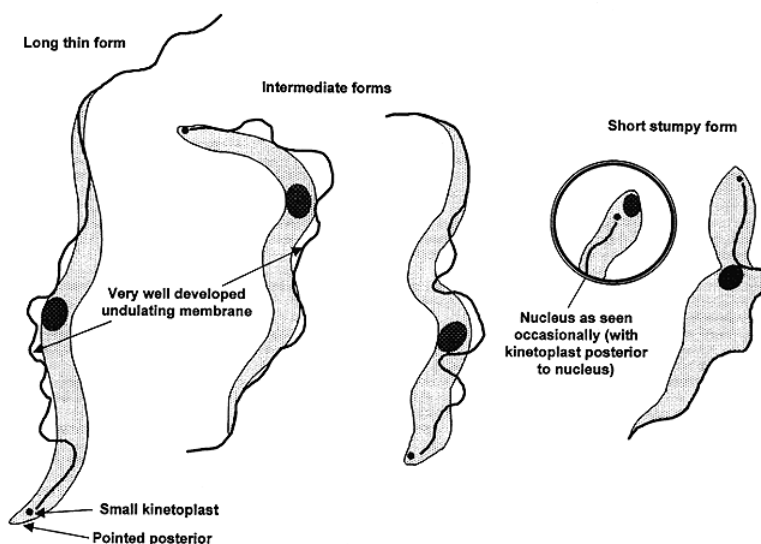


Figure 19. Different shapes of *T. brucei* parasites found in the blood stream. During the course of infection the shape of the parasite changes from long and thin to short and stumpy. This is due to a change in the respiration of the parasite which makes it possible to adapt to a new environment. The short and stumpy form, which is characteristic of late-stage HAT disease is able to survive in the tsetse fly midgut, while the long and thin form is better suited for fast proliferation in the human blood stream. Used with permission from the Food and Agriculture Organization of the United Nations.⁶⁶

The lengths range from around 30 μm for the slender form to 17 μm for the short and stumpy form. The width of the body ranges from 1.5 to 3.5 μm ⁵⁶. While all forms can be taken up by the tsetse fly however only the short and stumpy form is able to survive the complex life cycle in the midgut of the fly.⁵⁶ The motility of the parasites has been described as highly directional (e.g. in the same direction for a long period of time.) and their flagellum is able to generate a speed of up to 20 $\mu\text{m}\cdot\text{s}^{-1}$.⁶⁷

4.6 Immune response evasion of *Trypanosoma brucei*

When the parasites are transferred from the tsetse fly vector to the human host they will trigger an immune response of the host. Normally the human body would be able to produce specific antibodies against the pathogen and suppress the infection within roughly two weeks through the humoral immune response (HIR); however the trypanosome parasites have evolved an intriguing way to circumvent the host's defense mechanism. One of the symptoms characterizing trypanosomiasis is cyclic fevers. Fevers are initiated by the immune system both to increase its function but also to counteract a pathogen. When the fever decreases the immune response has accomplished its task and freed the body from the foreign substance. However this is not the case in trypanosomiasis due to the variable surface glycoproteins (VSG) coating of the parasites, which enable them to evade the immune system. They have an ability to express an enormous range of different types of VSGs, in fact 10% of their total genome codes for these glycoproteins, nevertheless only one glycoprotein is present at the surface of the parasite, and at the same time the vast majority of trypanosomes present within a host all express the same one.⁵⁶ However there is a small fraction of the trypanosomes which have a different VSG and this is also the key in their success of evading the immune response. The antibodies mediated by the humoral immune system will be directed towards the common form VSG, eliminating the larger fraction of trypanosomes. The smaller fraction is however not recognized by the humoral immune system and is allowed to

continue to multiply, growing in numbers, until another immune response is triggered. This is the mechanism behind the cyclic fevers and chronic condition of trypanosomiasis as well as the fluctuating numbers of parasites found in the blood of the patients.⁶⁸ The normal concentrations found in the body (e.g. in lymph node aspirate, CSF or blood) are reported to range from between more than 10 000 trypanosomes/mL to less than 100 trypanosomes/mL.⁵⁶

4.7 Detection and diagnosis

Several methods for detection of trypanosome parasites have evolved in the last couple of decades. Some require a large scale laboratory; some can be used in the field. Some are very sensitive while others merely are a pre-step to another method which can be used for detection. A good method for the diagnosis of HAT needs to fulfill several criteria at once. Some of the more important are

- high sensitivity
- high specificity
- low cost
- high speed
- easy to use
- ability to perform field diagnostics

Several statistical measurements are commonly used to describe the outcome of any binary test. Sensitivity is the percentage of those detected as positives which are truly positive. A higher sensitivity results in fewer individual which may need to undergo the harsh treatment describe previously. Specificity is the percentage correctly diagnosed as healthy individuals; a higher number leads to fewer people which have the disease without getting treatment. Positive predictive value and negative predictive value reflect the percentages of patients with a positive and negative test result respectively who are

correctly diagnosed. These measurements will be used throughout this thesis and they can be summarized as follows:

$$\text{sensitivity} = \frac{\text{true positives}}{\text{true positives} + \text{false negatives}} \quad (28)$$

$$\text{specificity} = \frac{\text{true negatives}}{\text{true negatives} + \text{false positives}} \quad (29)$$

$$\begin{aligned} \text{positive predictive value (PPV)} \\ = \frac{\text{true positives}}{\text{true positives} + \text{false positives}} \end{aligned} \quad (30)$$

$$\begin{aligned} \text{negative predictive value (NPV)} \\ = \frac{\text{true negatives}}{\text{true negatives} + \text{false negatives}} \end{aligned} \quad (31)$$

4.7.1 Card Agglutination Test for Trypanosomiasis

The card agglutination test for trypanosomiasis (CATT) is an antibody-based detection method. It relies on the antibodies produced by the humoral immune response, which are specific to the surface epitopes of the common VSG form of the parasite. The method is able to detect the parasite after 3-4 weeks of infection due to the delayed production of antibodies in the immune system. A large drawback with this method is its specificity due to the relatively large number of false positives. These cases are known to occur both due to antibodies from previous infections which can persist in the body for up to 3 years after successful treatment⁶⁹ and cross-reactions with other types of infections. The cross-reaction are known to occur in patients suffering from malaria and other protozoan parasite including transient infections of non-human trypanosomes.⁷⁰ Further the test is only sensitive to *T. b. gambiense*, the West African variant of the disease.⁵²

4.7.2 Blood-film examination

The simplest way of diagnosing HAT is to place a drop of the patient's blood on a glass slide and examine it in a microscope. It is an uncomplicated technique but very time consuming and suffers from a high detection limit. Usually one trypanosome per 200 microscope fields is considered the detection limit of this method, which equals 10 000 parasites per mL.⁷¹ Even so, this is a widely used method to detect trypanosomiasis. The technique can be improved slightly by staining the samples according to Giemsa or Field, which results in a sensitivity increase to around 5000 trypanosomes/mL.

4.7.3 Lymph node aspirate

As an alternative to examining the blood films, a sample can be drawn from the central lymph nodes through a lymph node aspirate (LNA). This technique is possible when enlarged lymph nodes are present indicating a buildup of parasites in the nodes making detection slightly easier. The WHO advises field workers to carry out this test when possible after every positive CATT test.⁵⁶

4.7.4 mini-Anion-Exchange Centrifugation Technique

Mini-anion-exchange centrifugation technique (mAECT) utilizes the lower electrical surface charge of trypanosomes with respect to red blood cells to increase the concentration using ion-exchange chromatography. The eluate of the column is then subjected to low-speed-centrifugation before examination by microscope.^{72, 73}

4.7.5 Micro-hematocrit centrifugation technique

The micro-hematocrit centrifugation technique (MHCT) originates from the 1970's, where a small capillary tube which is filled with the blood of the patient is subject to high speed centrifugation. The cells are fractionated according to their sedimentation coefficient with the RBCs in the bottom followed by what is known as a buffy coat. This layer consists normally of the leukocytes and is also where any possible trypanosomes would end up. Therefore, the buffy coat is examined to detect any occurring trypanosomes.⁵⁶

4.7.6 Quantitative Buffy Coat

Quantitative buffy coat (QBC) combines a high-speed centrifugation step with fluorescent staining by acridine orange. This allows for better discrimination with respect to non-nucleated cells.⁷⁴

Table 3. Comparison of different techniques at detecting HAT

	<i>Detection limit (mL⁻¹)</i>	<i>Sensitivity (%)</i>	<i>Specificity (%)</i>	<i>Positive</i>	<i>Negative</i>
<i>CATT</i>		87-98 ⁵⁶	13-67 ⁵²	easy, high sensitivity	only gambiense, low specificity
<i>mAECT</i>	100-600 ^{56,75}	75.3 ⁷⁶		High specificity	Need trained personnel. Low storage time of materials
<i>WBS</i>	10 000			easy, high specificity	time consuming, detection limit
<i>LNA</i>		40-80 ⁵⁶		Simple, cheap	Low sensitivity, only possible with enlarged CLN
<i>mHCT</i>	500 ⁵⁶	<75 ⁵⁶			uses fluorescent staining
<i>QBC</i>	450 ^{56,74}	75-95 ^{56,76}			involves several processing steps

Due to the combination of high sensitivity and lower specificity for the CATT technique it has been recommended by the World Health Organization (WHO) to use this technique solely for mass screening programs of HAT where positive results are verified using a secondary method of higher specificity. There have also been initial trials with an antibody-based technique, which detects circulating antigens released by the trypanosomes instead of the antibodies released by the humoral immune response of the host. The technique, known as Card Indirect Agglutination Test for Trypanosomiasis (CiATT), showed initially an excellent sensitivity exceeding 95%⁷⁷ but questions of its specificity have later been raised.⁷⁸

4.8 *Trypanosoma cyclops*

Due to the risk, and as a consequence, the strict regulations involved with working with *T. brucei* the work in this thesis has been carried out with a relative to the pathogenic *T. brucei*, namely *T. cyclops*. *Trypanosoma cyclops* is like *Trypanosoma brucei* a member of the *Trypanosoma* genus. However, it resides in South-East Asia where its natural hosts include the common chimpanzee and several macaque species. It is not pathogenic to humans, due to the presence of blood factors which act to lyse the parasites, making experimental work easier to carry out with less safety regulations. Due to its close evolutionary relationship to *T. brucei* their morphologies are very similar, making the *T. cyclops* an ideal model organism to the pathogenic variant. As a consequence, all experiments described in this thesis were performed using *T. cyclops*.

5. Blood

There are a large number of functions, many crucial for survival, which rely on the blood system in the human body. It supplies all of the approximately $3 \cdot 10^{13}$ cells of the human body with the essential nutrients and oxygen as well as removing their waste products such as carbon dioxide and lactic acid. It also acts to maintain homeostasis by regulating the pH and core body temperature. It defends the body from foreign compounds using antibodies and white blood cells (WBCs) and at the same time it has its own self-repairing mechanism carried out mainly by the platelets. Due to the vast number of functions that blood fills it contains a wealth of information about a person's health, making blood the most common sample in diagnostics.

In this thesis blood is important because our method is targeted at separating the scarce number of parasites present in an enormous background of blood cells. Knowledge of the dynamics of the RBCs and their behavior in the DLD devices needs to be established in order to acquire the knowledge of how we can achieve the greatest difference in behavior, and consequently the most sensitive separation, between RBCs and the trypanosome parasite in our DLD devices.

5.1 Composition

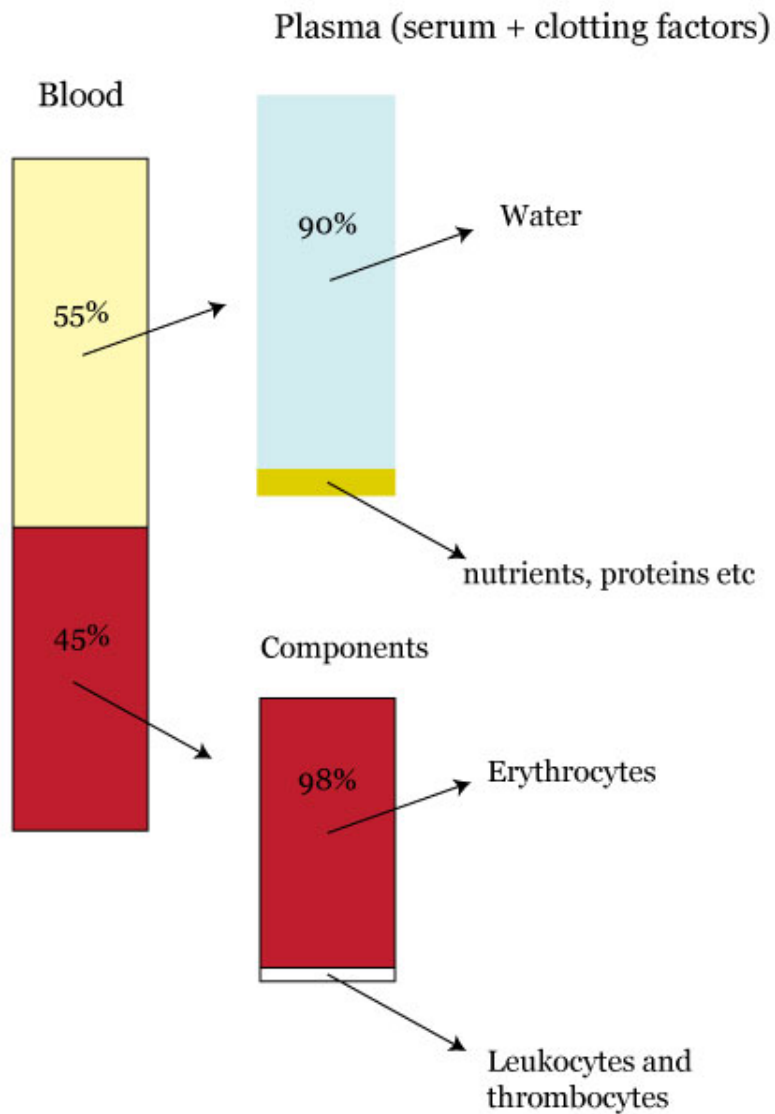


Figure 20. Normal volumetric relationship between the different constituents of blood. Noteworthy is the large cell fraction of erythrocytes (RBC), 98%. Blood is a very densely packed fluid with less than half of its constituent made up of water.

Due to the many functions of blood, it has a rather complex composition with many different constituents as can be seen in *Figure 20*, the whole blood is divided into blood plasma and blood components. The main part is the blood plasma with 55% (v/v) while the cellular components make up the remaining 45%. Blood plasma is the fluid in which the components flow, 90% of its volume is water while the 10 remaining percent are made up of dissolved molecules such as glucose, minerals, nutrients, the major part of the excreted carbon dioxide and several kinds of plasma proteins. The two major groups of proteins are albumins and globulins, with around 60% and 35% of the total number of plasma proteins respectively. Albumin has several important roles including pH buffering and transporting non-soluble molecules. The globulins comprise several different transport proteins and immunoglobulins. Transport proteins are vital for the body as they ensure that molecules are able to reach their targeted destination. This can be molecules which are water-insoluble or molecules which normally would be filtered out by the kidneys. Another important function of the plasma proteins is to retain the oncotic pressure; this is the osmotic pressure of the blood vessels which counteracts the tendency of fluids to leak out of the capillaries. The proteins are able to maintain this pressure merely by their larger size, which makes them able to withstand being filtered through the endothelial tissue lining the vessels.

The other part of the blood, the components – or blood cells, comprises 45% of the total blood volume and a vast amount of this fraction is made up of the erythrocytes, the red blood cells. These cells are responsible for supplying all of the cells of the human body with oxygen and also transporting back a significant portion of the carbon dioxide which is produced by the cellular respiration. The small remaining portion of the blood components consists of the leukocytes (white blood cells) and platelets. The white blood cells are part of the immune system, and comprise many different cell types. Their common task is to eliminate pathogenic components, which could

enter the body. The platelets are one of the key factors in the hemostasis, the process of maintaining the blood inside of a damaged tissue.

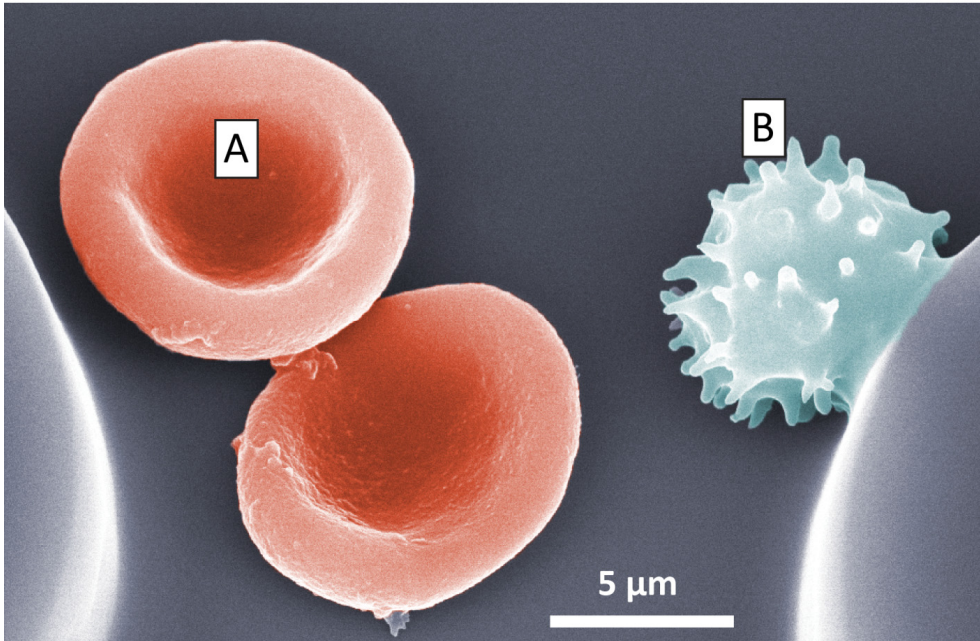


Figure 21. A color-enhanced SEM-micrograph of (A) Red blood cells, with their typical biconcave shape. And (B) a white blood cell, most likely a neutrophil due to its size of around $8\ \mu\text{m}$ in diameter. The WBC is more spherical than the RBC and has a typical spiked surface. Used with kind permission from Jason Beech.

The normal resting sizes of the different blood cells and their concentrations are given in *Table 4*. The cells normally experience high shear stresses in the blood stream giving rise to extensive deformations. Consequently, the shapes and sizes given are only valid for resting, stationary, cells. Further, both the sizes and the concentration can be altered due to a person's health, gender and also environmental factors, the size can also be changed to the age of the cell. Additionally, the sizes of the different blood cells of a single individual occurs normally within a fairly broad range, acting to further increase what values can be considered normal.

Table 4. Morphology and concentration of the blood components

<i>Cell type</i>	<i>amount (μl^{-1})</i>	<i>size (μm)</i>	<i>number fraction</i>	<i>volume fraction</i>	<i>visible surface</i>
RBCs	$5.1 \cdot 10^6$	7.2-8.4	0.93	0.98	0.99
WBCs	7000		$13 \cdot 10^{-4}$	0.01	$3.0 \cdot 10^{-3}$
<i>Lymphocyte</i>	2185	6-8 ⁸⁰	$40 \cdot 10^{-5}$	$8.4 \cdot 10^{-4}$	$3.5 \cdot 10^{-4}$
<i>Neutrophils</i>	4150	9-16 ⁸⁰	$76 \cdot 10^{-5}$	$9.1 \cdot 10^{-3}$	$2.2 \cdot 10^{-3}$
<i>Eosinophils</i>	165	12-17 ⁸⁰	$30 \cdot 10^{-6}$	$5.6 \cdot 10^{-4}$	$1.2 \cdot 10^{-4}$
<i>Basophils</i>	44	10-14 ⁸¹	$81 \cdot 10^{-7}$	$8.5 \cdot 10^{-5}$	$2.1 \cdot 10^{-5}$
<i>Monocytes</i>	456	12-20 ⁸²	$84 \cdot 10^{-6}$	$2.1 \cdot 10^{-3}$	$3.9 \cdot 10^{-4}$
Platelets	350 000	2-3 ⁸³	0.064	$8.4 \cdot 10^{-3}$	$7.3 \cdot 10^{-3}$

Three different fractions of the blood components have been defined based on their size and shape, and are presented in *Table 4*. They are the number fraction, volume fraction and visible surface fraction. with the values are the fractions of the blood components, to get the fraction of whole blood the numbers should be multiplied with 0.45. The calculated fractions all have their own importance during both analysis and sorting of blood. The visible surface fraction has been produced to show the cell's significance when examining a blood smear through a microscope, the most commonly used technique to detect the trypanosomes parasites in the field.

5.2 Red blood cells

A normal person has around five liters of blood depending on body weight, gender and age. This, together with the fact that red blood cells constitute 45 % of the total volume of blood, makes them a major cell type in the human body. In fact, around one tenth of the total number of cells in a human body is believed to be RBCs.⁸⁴

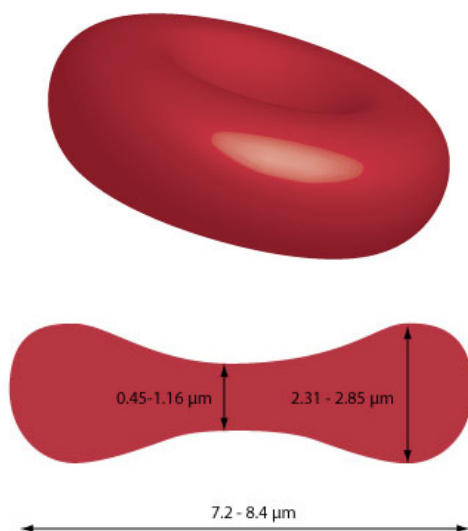


Figure 22. An illustration of the biconcave red blood cell and its cross-section. Showing typical reference ranges of the sizes.⁸⁵ The size and shape can change naturally due to cell age or due to other factors such as genetic mutations, e.g. stomatocytosis, or diseases such as malaria.

One of the main functions of the red blood cells (RBC) is to transport oxygen from the pulmonary capillaries lining the alveoli of the lungs to tissue surrounding the capillary beds. This is facilitated by the hemoglobin (Hb) molecule of the RBCs. Hb is found in copious amounts within the cells. The most common form, hemoglobin A, consists of two α and two β subunits, which come together to form a tetramer. Each subunit is linked to a heme group, which consists of a heterocyclic ring with an iron ion in the center. Each iron ion is capable of binding one oxygen molecule, making each Hb able to carry four oxygen molecules. Its ability to bind oxygen, the oxygen affinity, is a function of the interaction between the subunits through cooperative binding as well as the potential hydrogen- (pH) level in the Bohr effect. Cooperative binding means that the oxygen affinity increases upon one of the subunits binding oxygen while the Bohr effect decreases oxygen affinity at low pH which occur in tissues with increased metabolic rate.

The production of red blood cells, erythropoiesis, starts with the same type of pluripotent stem cell as all of the other blood components, the hemocytoblast. After several subsequent differentiations an immature red blood cell is produced; known as the reticulocyte. It is the first stage in the development towards the erythrocyte, which enters the blood stream. The name stems from the mesh-like network of ribosomal RNA which becomes visible upon staining with *e.g.* methylene blue. The cells circulate the vasculatory system for about 24 hours before completing the maturation and becoming indistinguishable to the other red blood cells. As the average life-time for an erythrocyte is 120 days,⁸⁶ the normal fraction of reticulocytes in the blood should be 0.83 percent. A higher reticulocyte count could be a sign of anemia, due to the increased production of new RBCs.

Considering the normal life span of an RBC of 120 days, as previously mentioned, if a person has five liters of blood and 5.1 million red blood cells per microliter of blood, the mean production to maintain the total number of erythrocytes in the circulatory system would be around two and a half million per second. Further, it might seem like a short lifespan for these cells, and it is comparing to other cell types. However, a normal cycle in the circulatory system takes about 60 seconds and a mean distance travelled in one cycle could be estimated to roughly 2 meters. This makes the red blood cell acquire a total distance of almost 350 km in densely packed blood vessels where the cells are subject to large mechanical stresses both from the walls and the other cells, and there are no repair mechanisms available for these cells either. As the RBCs age their deformability decreases and consequently they are sorted out by the macrophages in the liver, spleen and bone marrow for a more effective recycling of the hemoglobin.

5.3 Red blood cell deformability

As has been discussed previously, separation in a DLD device could have the ability to separate between particles of different softness.

Hence, studying the deformability of the RBCs could open up for separation between RBCs and the trypanosome parasites, given that their deformability differs.

The strength and flexibility of the erythrocytes is in large part attributed to their cytoskeleton which is made up of a dense network of spectrin molecules. This is a long fibrous protein which consists of two dimeric subunits.⁸⁷ The spectrin molecules line the inside of the cell membrane in a manner reminiscent of spokes and hubs. In *Figure 23* the blue molecules is the spectrin tetramer whose midpoint is attached to the cell membrane through what is known as the ankyrin complex. Even though it is not visible in the picture the endpoints of several molecules are attached to a hub, which also is connected to the cell membrane. It has been shown that this design is able to give the cell membrane an elasticity which allows it to be elongated to 15% before it reaches its point of rupture.⁸⁸

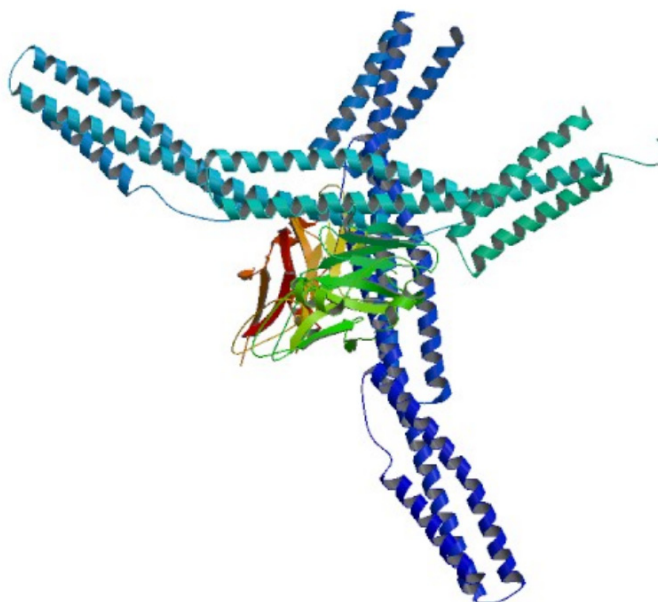


Figure 23. The spectrin tetramer complex and its attachment to the ankyrin complex acting to give the RBCs both a great deformability and stability. Reprinted with permission from the Research Collaboratory for Structural Bioinformatics. Protein was deposited in 2009 by Ipsaro, J.J. and Mondragon, A.^{89, 90}

The RBC has normally a biconcave shape with the size outlined in *Figure 21*. Its unique shape is advantageous due to its higher surface area-to-volume ratio. This increases the exchange of gases with the environment enabling a higher amount of oxygen and carbon dioxide to be transported. A second effect of its higher SAV-ratio is the increased deformability, which is vital in its ability to squeeze through the smallest passages of the circulatory system. The capillary beds of the microcirculation can have diameters down to $3 \mu\text{m}$ ⁹¹ while the passages in the sinusoids can be even smaller. The sinusoids are found in the liver, spleen and bone marrow and are used to effectively sort out the less deformable aging blood cells⁹². The large surface area can be illustrated by considering the normal volume of a resting RBC in its discoid shape, 90 fL. The surface area is at the same time $163 (\mu\text{m})^2$ ⁹³. If the RBC instead was a sphere encapsulating the equal amount of volume it would have a lower surface area. The radius and surface area of a sphere encapsulating 90 fL is as follows.

$$r = \left(\frac{V \cdot 3}{4\pi}\right)^{\frac{1}{3}} \rightarrow A = 4\pi r^2 \rightarrow A = (36\pi V^2)^{\frac{1}{3}} \quad (32)$$

$$= (36\pi(90 \cdot [\mu\text{m}]^3)^2)^{\frac{1}{3}} = 97\mu\text{m}^2$$

This results in an excess surface area of $66 \mu\text{m}^2$ or 68 % for the biconcave RBCs, which in large part is responsible for the RBCs ability to deform heavily when passing the capillary beds and sinusoids.

Two other factors are also important to the deformability of the RBC, namely the intrinsic viscosity of the cell and the viscoelastic properties of the cell membrane. Different techniques are available to measure the deformability however as the techniques differ in their sensitivity to the different underlying parameters the results of different methods are complicated to compare. Further, several of the techniques rely on bulk measurements of the hemorheological properties to measure the erythrocyte deformability. This does not provide information about the underlying heterogeneity of the samples and would instead produce a

measurement of the average in the sample. Further, the measurements will be affected by additional parameters of the sample, such as the hematocrit, plasma viscosity and erythrocyte aggregation.⁹⁴

5.3.1 Erythrocyte filtration

Filtering the erythrocytes through a membrane is a common way of measuring the deformability.^{95,96} The most common mode of operation of this method is to register the time required to flow a certain volume through the membrane. The diameters of the pores in the membrane are usually in the range from 3 to 5 μm . As all constriction-based methods the largest drawback is that larger cells or other aggregates are able to block the pores, which can affect the measurements. At constant pressure, the flow will decrease with every clogged pore. It is also a bulk measurement method where the final result is affected by several parameters, including the hematocrit and the cell rigidity. Consequently, the sample needs to undergo further testing in order to give any conclusive results.

5.3.2 Ektacytometry

In Ektacytometry (EC), or laser diffracted ellipsometry (LDE) which is another name for this technique, the erythrocytes are subjected to well-defined shear stresses in polyvinylpyrrolidone (PVP), a high-viscosity medium.^{97, 98} A laser is pointed at the suspension and produces a diffraction pattern which is registered and analyzed to give information about how the cell shapes. It does not experience clogging, but the measurement is an average of the whole sample population. One advantage is the relatively fast time in which a stress-strain curve can be achieved.

5.3.3 Micropipette aspiration technique

In the micropipette aspiration technique (MAT) glass capillaries with diameter of 1-5 μm are used to aspirate single erythrocytes.⁹⁹⁻¹⁰¹ The pressure needed to aspirate the cell reflects the deformability of the cell. Even though much information about the viscoelastic properties of single cells membranes are acquired. The technique is however

seldom used in standard practice due to the fact that it is time consuming and difficult to carry out. Further it has been shown that aspiration of RBCs can induce changes in the membrane, giving a source of error during measurements.¹⁰²

5.3.4 Erythrocyte sedimentation rate

One of the most well-known blood test is the erythrocyte sedimentation rate test (ESR), or the Biernacki reaction¹⁰³. It is not sensitive to deformability, however, it is a very common line of first screening at hospitals around the world as a nonspecific indicator of inflammation and tissue injury. The procedure is carried out by measuring the length of the plasma pillar which has developed after a blood sample has been allowed to stand for one hour. The sedimentation rate may be increased by an alleviated concentration of polar proteins such as fibrinogen. Due to their polarity, the fibrinogen will act to decrease the zeta potential of the blood giving rise to rouleaux formations.¹⁰⁴ These stacks of RBCs will sediment faster. The zeta sedimentation rate (ZSR)¹⁰⁵ gives a similar measurement but is less affected by the hematocrit, giving a more reliable measure of a possible inflammation.

5.4 Microfluidic methods for red blood cell deformability analysis

As has been discussed in *Chapter 1* and *2*, there has been a great increase in the number of both preparative and analytical microfluidic devices in the last decade. Devices aimed for analysis of specific parameters of the blood, providing cheap and rapid point-of-care devices, as well as preparative devices used to sort out specific cell for further analysis. Examples from the everyday life include the glucose monitors of diabetes patients and home pregnancy test; both have acted tremendously to decentralize medical technology. The many benefits these methods offer in comparison with how the same procedures were carried out in earlier days, such as the radioimmunoassays pregnancy tests demanding expensive and specialized equipment coupled with

trained personnel, makes them highly desirable. Besides the lowered cost per test, they can exploit the microfluidic phenomena, which stems from the increased surface area-to-volume ratio, and maybe most importantly they offer single-cells measurements revealing any underlying sample heterogeneity. There exist a tremendous amount of microfluidic devices; in this section a few methods which can be compared to the aforementioned traditional blood cell analysis methods will be described. Several good reviews of analytical and preparative microfluidic devices focused on the handling of blood have been published where the interested reader can find more information.^{14, 106-108} In this section a few examples of both preparative and analytical microfluidic device will be presented.

5.4.1 Restriction based microfluidic devices

Restriction based microfluidic devices have been used to a great extent to study the RBC dynamics. The technique is relatively similar to MAT which also forces the RBCs in to a constriction, but the advantage with the microfluidic devices is how the dynamic behavior of the cells can be studied and, in addition, this can be done in a repeatable manner. Several different types of devices have been constructed; examples include membranes with small pores, narrow channels and weir structures. Narrow microfluidic constrictions can act to mimic blood capillaries making them ideal for studying the RBC behavior in the body, this was done *e.g.* by Sutton *et al.*¹⁰⁹ who used parallel channels of varying widths coupled to automated detection of transit times, *Figure 24A*. Brody *et al.*¹¹⁰ studied the behavior of RBCs through an array of small constrictions, 2-4 μm in widths, *Figure 24B*. Interestingly they did not see a clear correlation between RBC diameter and the flow speed of the individual cells through the constrictions, instead what seemed to determine the speed to a great extent was the internal calcium content of the cell, which could be measured by introducing a calcium binding dye, fluo-3 AM. The shear forces exerted by the fluid were believed to activate calcium gates which, in turn, activated the cytoskeletal actin and spectrin network

which caused a great increasing in the cortical cell rigidity. Gifford *et al*¹¹¹. used wedge shaped confinements to study the areas and volumes of single erythrocytes, *Figure 24C*. By measuring the position of the leading end and the trailing end, these values could be derived. Mean corpuscular volume (MCV) are often used during regular medical diagnosis, provided as the hematocrit divided by the RBC concentration. Here, the actual volume distribution of single cells is given, providing far more information and, consequently, a more accurate diagnosis.

5.4.2 Laser-based microfluidic devices

Optical tweezers have been used to study the deformability change induced by *plasmodium falciparum* infection, *Figure 24E*. The technique works by having a small portion of the RBC surface attached to a cover slip while the diametrically opposite side of the cell has a Con-A coated polystyrene microsphere attached. By using the optical tweezers one can derive force-displacement values of the cell which can be used to derive the corresponding shear modulus.¹¹² Optical stretchers have also been incorporate in microfluidic channels to continuously test the deformability of individual RBCs, *Figure 24D*.¹¹³ By having two divergent lasers in a microfluidic laser a trapped cell will be stretched along the laser axis with a force which corresponds to the laser intensity. Another method for studying the dynamics of the RBCs was presented by Wakasa *et al*.¹¹⁴ where a high speed flow was used to impinge red blood cells on the microfluidic channel walls and study the shape response upon impact, *Figure 24F*. Both deformability was studied and the dynamics of hemolysis at very high shear rates.

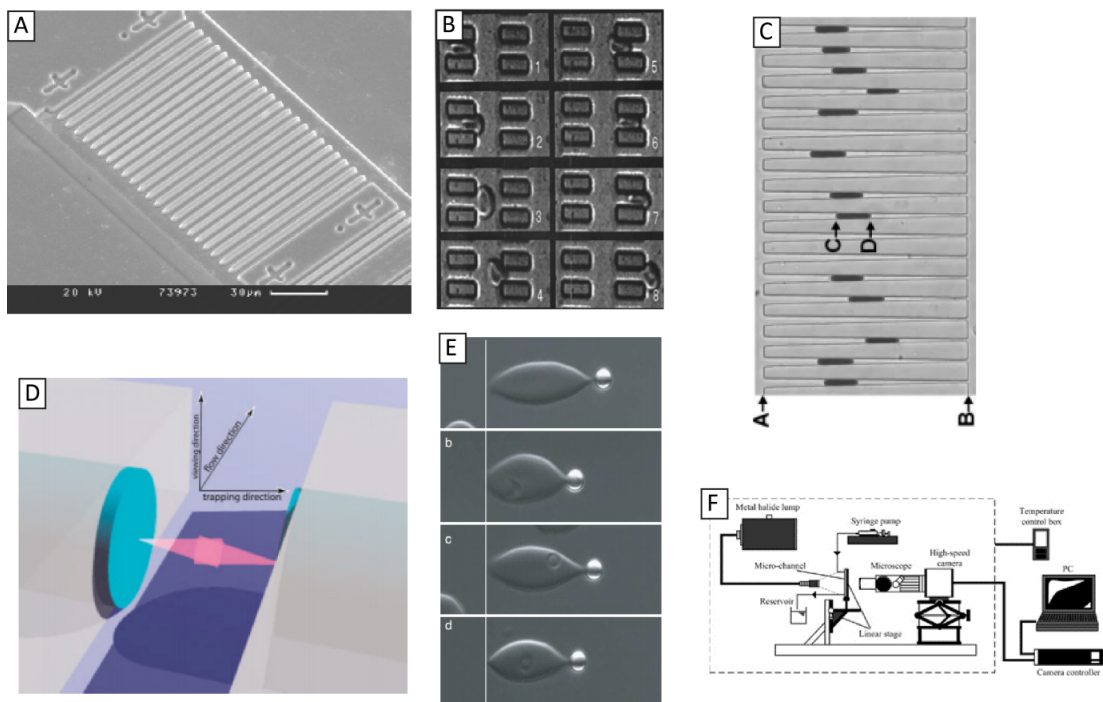


Figure 24 Different techniques which have been shown to be capable of analyzing the size and deformability of single red blood cells. (A) Parallel channels of varying widths coupled to automated detection of transit times was used by Sutton et al.¹⁰⁹ Image used with permission from the Royal Society of Chemistry (B) Brody et al.¹¹⁰ studied the dynamic behavior of RBCs through an array of small constrictions, 2-4 μm in widths (C) Gifford et al.¹¹¹ instead was using wedge-shaped constrictions in order to study both the surface area and the volume of single RBCs. (D) Optical tweezers have been used to study the deformability change induced by plasmodium falciparum infection.¹¹² By having one side of the RBC immobilized to a surface while stretching the other side a force-displacement curve could be derived. (E) Optical stretchers have also been incorporated into microfluidic channels to continuously test the deformability of individual RBCs.¹¹³ (F) Another method for studying the dynamics of the RBCs was presented by Wakasa et al.¹¹⁴ where a high speed flow was used to impinge red blood cells on the microfluidic channel walls and study the shape-response upon impact

5.5 Anemia

As previously discussed, the wealth of information contained within the blood makes it an ideal target for the first screening of patients. Very accurately defined intervals exist for a wealth of parameters of the blood, including the mean corpuscular volume (MCV), the mean corpuscular hemoglobin concentration (MCHC), the hematocrit (Ht) and the red blood cell distribution width (RDW).¹¹⁵ Careful analysis of these parameters and detection of any sample outside the given reference ranges gives a clear indication of the persons health state. When weighing all the parameters together a more confident diagnosis can be given and the specific disease causing the behavior could be determined, in some cases the diagnose given by the microfluidic blood analysis test can be followed up with a tests specific to certain diseases. A microfluidic diagnostics device would be very capable of making up the first line of diagnosis in order to detect different blood diseases. Anemia is a group of blood diseases which all result in a lowered amount of blood cells. Different reasons may be the cause for this; often lowered deformability and/or shape-changes act to sort them out in the spleen or liver by the same mechanisms as sorts out old blood cells in healthy individuals.¹¹⁶

5.5.1 Sickle cell anemia

Sickle cell anemia is caused by a variant hemoglobin gene, HbS instead of the normal Hb. Even though the trait is recessive it is still prevalent in Africa and can also be found in areas of the middle east, Mediterranean and India.⁷⁹ The reason is that people affected with this trait are less likely to be infected with malaria the endemic areas of which overlap those of the sickle cell anemia.¹¹⁷ The altered hemoglobin molecules will cluster together and form long fibers when they are deoxygenated. These long fibers will distort the cell shape and at the same time decrease its deformability. This will make the sickle-shaped red blood cell more likely to undergo hemolysis in the capillaries as well as being filtered out by the Kupffer cells of the spleen, liver and bone marrow.

5.5.2 Thalassemia

Thalassemia is another anemia which affects the Hb of the RBCs. It is a recessive genetic disorder which targets either the α or β -chain of the hemoglobin. The prevalence of the type of mutation varies between different populations. In large, the genetic disorder targeting the β chain of the hemoglobin is more frequent in the Mediterranean while the one targeting the α chain is more common in Africa, Middle East and Asian countries. Both of these mutations can either lead to thalassemia minor or thalassemia major, depending on if the individual is heterozygous or homozygous respectively for the trait. The aforementioned is less severe with patient having smaller erythrocytes than normal resulting in lower oxygen delivery. The major type will result in death within a few years if left untreated with erythrocytes being smaller and abnormally shaped, due to the lower amount of hemoglobin content.¹¹⁸

5.5.3 Pernicious anemia

An anemia which does not stem from a hemoglobin deficiency is pernicious anemia. Instead, it is due to an autoimmune destruction of the cells which secrete intrinsic factors which are crucial for absorption of vitamin B12 in the ileum of the small intestines. The lack of vitamin B12 affects the body's ability to synthesize DNA. This results in an abnormal erythropoiesis which acts to develop larger RBCs, macrocytes, than normal.

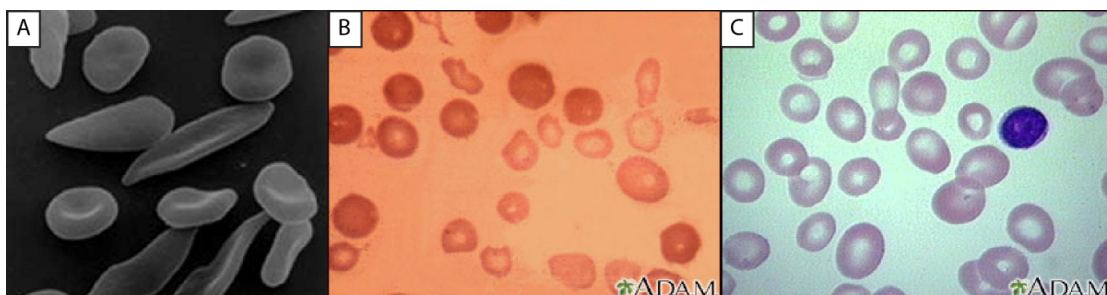


Figure 25 Three different forms of anemias. (A) Sick cell anemia which is due to a genetic mutation of (Hb) resulting in hemoglobin molecules which cluster together forming long fibers acting to distort the RBCs. (B) Thalassemia is also a genetic disorder of the hemoglobin allele, instead of an abnormally functioning hemoglobin it is due to a lower

hemoglobin content in the RBC. (C) In Pernicious anemia an autoimmune destruction of the cells secreting intrinsic factors. This leads to distortion of the erythropoiesis which results in anomalous large RBCs.(A) Used with permission from Scientific American¹¹⁹, (B-C) Used with permission from Medline Plus^{118, 120}

5.6 Anemia and HAT

Even though the focus of this project is sorting and detecting of trypanosomes the study of blood has been equally, or even more crucial for the progress of the work. Understanding of the cell dynamics of blood and its behavior in a DLD device has been crucial. As has been shown, during diseases the morphology and concentration of blood can be affected. A study by Thuita *et al.*⁵⁷ has shown that there might be a relationship between *Trypanosoma brucei rhodesiense*

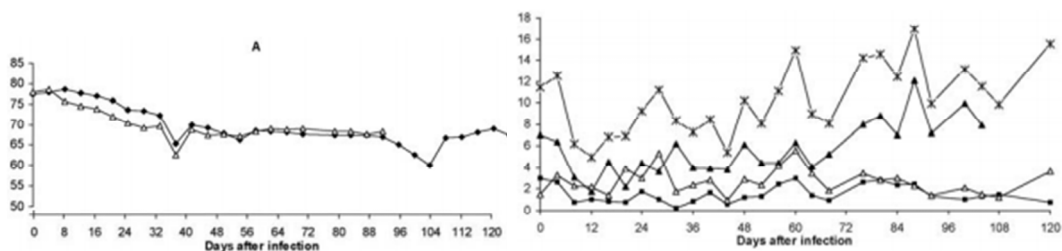


Figure 26. Graph showing the relationship between *T. brucei rhodesiense* infection and (A) mean corpuscular volume (MCV) and (B) the differential lymphocyte count. During the early stages of the disease granulocytes and lymphocytes are approximately equal in concentration, however as the disease progresses the granulocytes decline in number. (X - Total WBC, ▲ - lymphocytes, △ - Granulocytes, ■ - Monocytes). Images used under Creative Commons License from Public Library of Science².

infection of vervet monkeys and the change in these parameters of the blood, as can be seen in *Figure 26*.

6. Experimental Details

The experimental part of this thesis involves many different steps. Starting off with the first ideas of the device design together with computational analysis performed with COMSOL Multiphysics 4.0 which is presented in Chapter 3. Following this is the processing of the device in order to acquire a functional final device able to analyze the samples. This device was then subject to careful characterization of both its internal critical structures as well as its performance in separating samples of interest. The separation performance was characterized by analyzing the trajectories of spherical polystyrene beads of known sizes in the device. After the characterization of the device the behavior of blood was examined. This was done at different channel depths, different pressures and different osmolarities (salt concentrations). It has been shown that changing the channel depth can have an effect on the particle behavior.¹²¹

Increasing the pressure would most likely result in a different trajectory through the device of the cells as they are soft biological cells, *i.e.* they would have a smaller effective size. The changes to the osmolarity of the solution were also done in order to study if the behavior of the RBCs could be modified. After examination of the different methods used to change the behavior of the RBCs, the one which worked the best was chosen to be used in order to maximize the sorting efficiency of a sample containing both blood and trypanosomes. The method which worked the best was the optimization of depth and after the initial characterization of the behavior of trypanosomes at different depths the channel which resulted in the largest difference in behavior was chosen and a final measurement with whole blood in the device at this optimized depth was carried out.

The details of the experimental methods are given here in **Chapter 6**, which include everything from how the devices were processed to how the measurements were carried out and the result determined. Further, both the handling and characterization of the biological samples are given.

The designing of the device, what parameters were important for this project and the initial characterization and calibration with hard polystyrene microspheres are presented in **Chapter 7**.

The blood experiments are presented in **Chapter 8**. As stated above, the behavior of blood was examined at different pressures, device depths and osmolarities in order to manipulate the effective size of the RBCs. Different pressures give rise to a change in soft particles due to the shear forces acting to compress the cells. Different channel depths can act to orient the cells and consequently, in for example a shallow device, force the effective size to be equal to the diameter of an RBC. By altering the osmolarity of the surrounding medium water will either flow in or out from the cell. Consequently there will be a change in effective size (both due to an actual size change but also due to a morphology change).

In **Chapter 9** the behavior of the trypanosome parasites are characterized at different depths, the method which was determined to be the best for controlling the behavior of RBC in **Chapter 8**, of the device to study how the rotational freedom, or hindrance, act to alter its effective size. This is followed by analysis of samples containing both blood and parasites at the specific depth where the behavior of trypanosomes and RBCs are expected to differ the most and consequently the separation efficiency will be maximized.

6.1 Device fabrication

As has been discussed previously the process of manufacturing a complete DLD device involves many different steps. However, the introduction of techniques such as soft lithography and fluidic

simulations by computational fluid dynamics (CFD) act to decrease the turnaround time into a couple of days. Consequently, the time from the first idea to the final analysis of an experiment has decreased considerably. An outline of the different steps involved in the making of a complete working DLD device is shown in *Table 5*.

Table 5. *Device processing*

Step number	Description of step	Typical time needed
1	Drawing of the device (with consideration taken to e.g. the number of inlets and outlets, number of different arrays needed and their corresponding critical sizes)	~3 days
2	Flow simulations of parts of the intended device design in Comsol Multiphysics	~1/2 day
3	Finalization of the drawing of the device using L-Edit 11.02 (Tanner Research, Monrovia, CA USA)	~1 day
4	Production of the device design by laser ablation of blank masks. The masks we used were 4 inch chrome on quartz plates which were manufactured by Delta Mask, Enschede, Holland, by the use of Heidelberg DWL 200 Laser Beam Pattern Generator.	~2 days including shipping
5	The mask is used in UV-lithography in a mask aligner (Karl Süss MJB4, Munich, Germany) to pattern a 3" wafer with SU8 (MicroChem, Newton, MA, USA) at different viscosities, ranging from SU8-2005 to SU8-2050. This step together with the following is also shown more in detail in <i>Figure 27</i> . After a photolithographic mask has been produced the device can be produced in multiple copies (>50).	~1/2 day
6	The fabricated master is used in soft	~2 hours

lithography¹²⁷, where a polymer is poured on the master to create a copy of the pattern in a process known as replica molding.

7 The cured polymer is (together with a blank PDMS slab) subsequently exposed to oxygen plasma treatment (Plasma Preen II-862, Plasmatic Systems Inc., North Brunswick, NJ, USA). The two PDMS slabs are bonded together in a condensation reaction. Inlets and outlets are attached to finalize the device. ~1 hour

8 Experiments and subsequent analysis of the results can take place

Total time

~1 week

The drawing of the UV-lithographic mask in L-edit is often a very time-consuming effort in the making of DLD devices, especially if many sections of different critical diameters are used. The exact positioning of each post is crucial to the final device performance. In the side of the arrays the positioning of the post is a bit more complex than in the center. A method which allows for a linear change in fluid flux from row to row was used in order to maintain symmetric flow through the device. With higher symmetry of the flow comes improved separation efficiency. As described by Inglis *et al.*¹²⁸ the gap size of the boundary on the zigzag side of the array is given by

$$g_n = G\sqrt{n/N} \quad (33)$$

where g_n is the gap in row number n . In the same manner the boundary on the bump-side of the device is given by *Equation (34)*.

$$g_n = G\sqrt{2 - n/N} \quad (34)$$

To actual implement this in L-edit takes very long time and is prone to result in some error along the way. Therefore an automated java program which was used to create the design file was written and can

be seen in *Appendix 5.2*. The in-parameters of this software included the manufacturing grid, the number of fractions to separate the particles into and the smallest and largest critical size. The finalized L-edit file was sent to Deltamask for manufacturing of the chrome on glass photolithographic mask. This mask can be reused many times to make several different molds in SU8.

The whole process from having the photolithographic mask until having a finalized device ready for measurements is shown in *Figure 27*. The first step in the device processing, performed in a clean room laboratory, is to bake an uncontaminated silicon wafer in the oven at $\sim 200^{\circ}\text{C}$ to evaporate any residual water layer on the surface or organic compounds. Following this, the SU8 is deposited on the wafer. The thickness of the SU8 layer, which corresponds to the final channel depth, is varied by choosing the correct viscosity of the SU8 resist and the appropriate spin speed. Higher viscosity and lower spin speed results in a thicker resist, while lower viscosity and higher spin speed results in thinner resist. As can be seen in *Figure 28* the spin time, and even the wafer size, can have an effect on the final thickness of the resist.

The addition of inlet and outlet reservoir where sample was added and collected was done by using $\sim 10\text{mm}$ long tubing which was glued to the final PDMS device. For the later devices in this project, which was used to analyze samples containing both trypanosomes and RBCs, the inlet and outlet reservoirs were introduced directly into the PDMS before curing in step 8 in *Figure 27*. This allowed for a device where the glue, which contained the toxic chemical toluene, could be removed from the process completely.

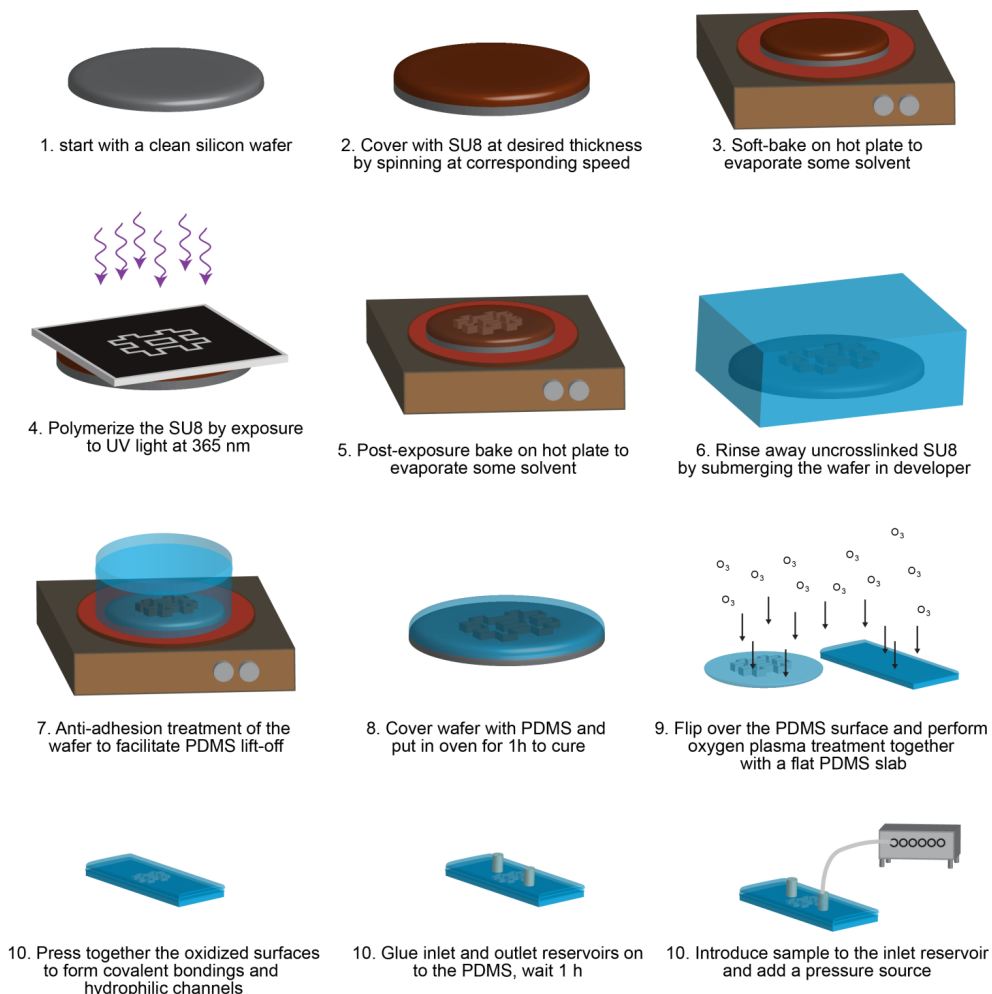


Figure 27 UV-lithography followed by soft lithography. (1) Starting from a clean 3 inch silicon wafer which is (2) covered with SU8 at the desired thickness. After (3) soft baking the wafer the SU8 is polymerized by (4) UV-light in a pattern defined by a photo mask. Following this is first a (5) post exposure bake step to remove solvent and (6) the development step where the wafer is submerged in developer, mr-DEV-600 (Micro Resist Technologies GmbH, Germany) to remove non-cross-linked SU8. (7) Silanization of the surface makes the (8) PDMS easy to peel off. (9) Oxygen plasma treatment makes the PDMS slabs possible to (10) bond together in a covalent condensation reaction. (11) Adding of reservoirs and applying the (12) sample and pressure source makes a final device ready for the experiment.

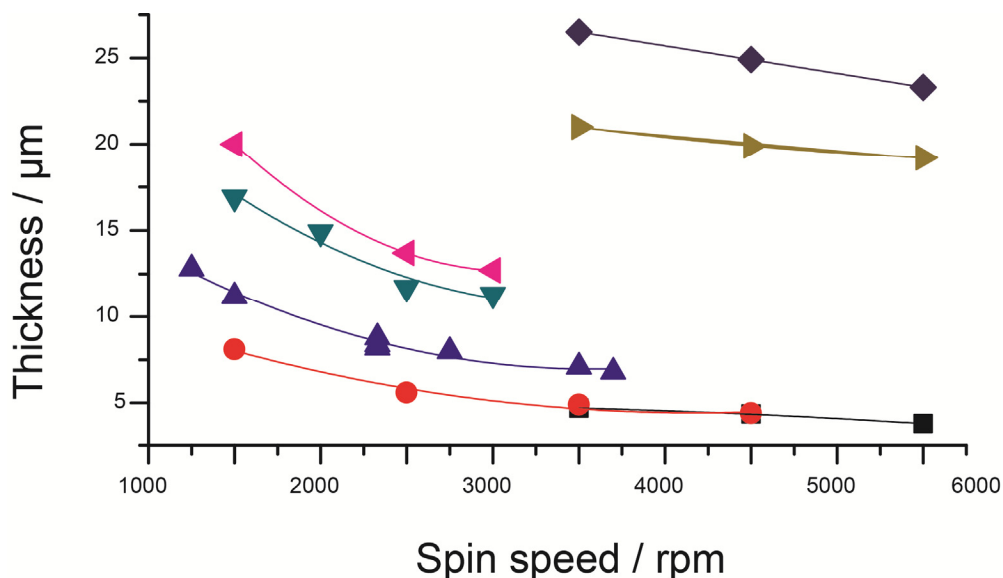


Figure 28 Some of the measured SU8 layer thicknesses in this project. Especially for the experiments conducted to analyze the behavior of cells at different channel depths, the spin curves were tremendously important. Several tests were conducted to acquire a good understanding of how what factors affected the final layer thickness. Apart from different SU8 solutions of varying viscosity and the spin speed, the other parameters which had an impact on the thickness was concluded to be the wafer size and the spinning time, as can be seen in the graph. All layers created by spinning for 45 s on a 3" wafer with fresh (<6 months old) SU8 if not stated otherwise. ■ new SU8-2005 ● 2 years old SU8-2005 ▲ SU8-2007 ▼ SU8-2015 ◀ SU8-2015 2" wafers ▶ SU8-2050 60s spin time ◆ SU8-2050 45s spin.

Our first generation of devices was bonded to glass slides as is commonly done. In these devices we observed a high concentration of echinocytes (deformed RBCs). We discovered later that this is due to the proximity to the glass surface consistent with the observations by Lim et al.¹²⁹ In order to avoid this problem we fabricated devices entirely in PDMS. The patterned PDMS slab was then bonded to a blank PDMS slide, step 9-10 in *Figure 27*, after the surface had been treated with oxygen plasma (Plasma Preen II-862, Plasmatic Systems Inc., North Brunswick, NJ, USA).

A pressure gradient was used to drive flow through the DLD devices. Outlets were kept at atmospheric pressure and the overpressure at the three inlets was controlled individually using an MFCS-4C (Fluigent,

Paris, France). This made it possible to hydrodynamically focus the sample into a stream of $\sim 10\mu\text{m}$ in width. All images were taken through an inverted Nikon Eclipse TE2000-U microscope (Nikon Corporation, Tokyo, Japan) using an Andor Luca EMCCD camera (Andor Technology, Belfast, Northern Ireland). Differential Interference Contrast (DIC) was used to ensure adequate contrast of blood cells and trypanosomes. For work with blood and *T. cyclops*, surfaces were treated to minimize adhesion. Immediately after O_2 plasma treatment and bonding, devices were filled with 0.2% PLL(20)-g[3.5]-PEG(2) (SuSoS AG, Dübendorf, Switzerland) in DI water and allowed to rest for at least 20 min before rinsing with phosphate buffered saline (PBS) for another 20 min.

6.4 Result analysis

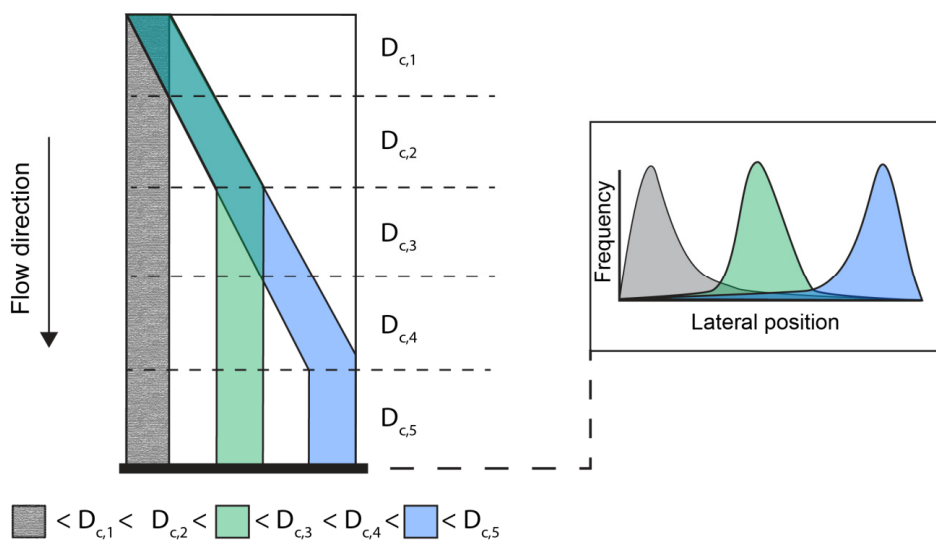


Figure 29 Schematic view of a device, the black line represent the position at the outlet where the particles positions are recorded. A typical graph showing the distribution of the particles are also shown. The small particles which constitute the background are not displaced in any of the sections while the larger green is displaced in 2 sections and the even larger blue particles are displaced in 4 sections. Images of the outlet are captured and the displacement of each particle is determined and the result is used to construct a frequency plot.

To analyze the result of an experiment, the lateral displacement of particles at the end of the device was measured, the black line in see *Figure 29*. By extracting the amount of lateral displacement of each single particle we could conclude in how many sections of the device which the specific particle had been displaced and consequently its effective size in the device. As the behavior of particles is not truly deterministic, some stochastic processes exist, such as diffusion and non-symmetric flows due *e.g.* device flaws or particle-flow interactions. The stochastic processes together with the size-distribution of the actual particles act to disperse the otherwise sharp peaks. For good statistics of the behavior, the lateral position of a very high number of particles needs to be determined. Manual

measurements are very time-consuming and also enable mistakes to be made. Consequently, a particle tracking software was written in MATLAB 2009b (The Math Works, Natick, MA, USA).

6.4.1 Particle tracking software

The tracking program was based on available MATLAB code¹³⁰ which accurately could register the pixel position of particles in an image. This served as the core in our tracking program which was optimized for our specific setup and had a graphical user interface (GUI) added, as shown in

Figure 30. The software was able to accurately track many particles in a field of view when the signal-to-noise ratio was sufficiently high and when the concentration was low enough to avoid particle overlap. This made it possible to obtain readings of particle trajectories of several hundreds or even thousands of cells per experiment. The code which was written for this project is given in *Appendix 5.1*. The GUI enabled the user to change input parameters and see the result instantly. By tweaking these parameters, which include how the background should be removed using fast Fourier transform (FFT), the particle size and the frames per second (FPS), accurate and quick analysis of the experiments were enabled.

This software was used to analyze all experiments in this work except the final measurements of undiluted blood and trypanosomes where the high concentration resulted in particle overlaps. Here instead ImageJ 1.43 (National Institutes of Health (NIH), Rockwell, ML) was used to evaluate the separation. By removing the static background and generating binary images, a time-integrated micrograph could be constructed which closely matched the actual distributions. While this method is able to deal with higher particle concentrations than the automated particle tracker, it has the drawback of underestimating the number of cells in regions of high concentrations due to particle overlap rendering distributions with larger variances with no sharp peaks. Further, a particle flowing slower will be weighed higher than a

particle flowing faster due to the time integration of the particles. This was not an issue in the tracking program which actually counts the number of particles and not their intensity.

An actual analysis carried out by the automated tracking software is shown in

Figure 30B. Here, the trajectories of many thousands of particles are detected during a time of around 12 minutes. This is shown at three different times, where the different trajectories getting a color code going from purple to green depending on the time when they enter the field of view. In the final time step at 725 s the line where the measurement is carried out is shown, producing the graphs which are found in the proceeding chapters.

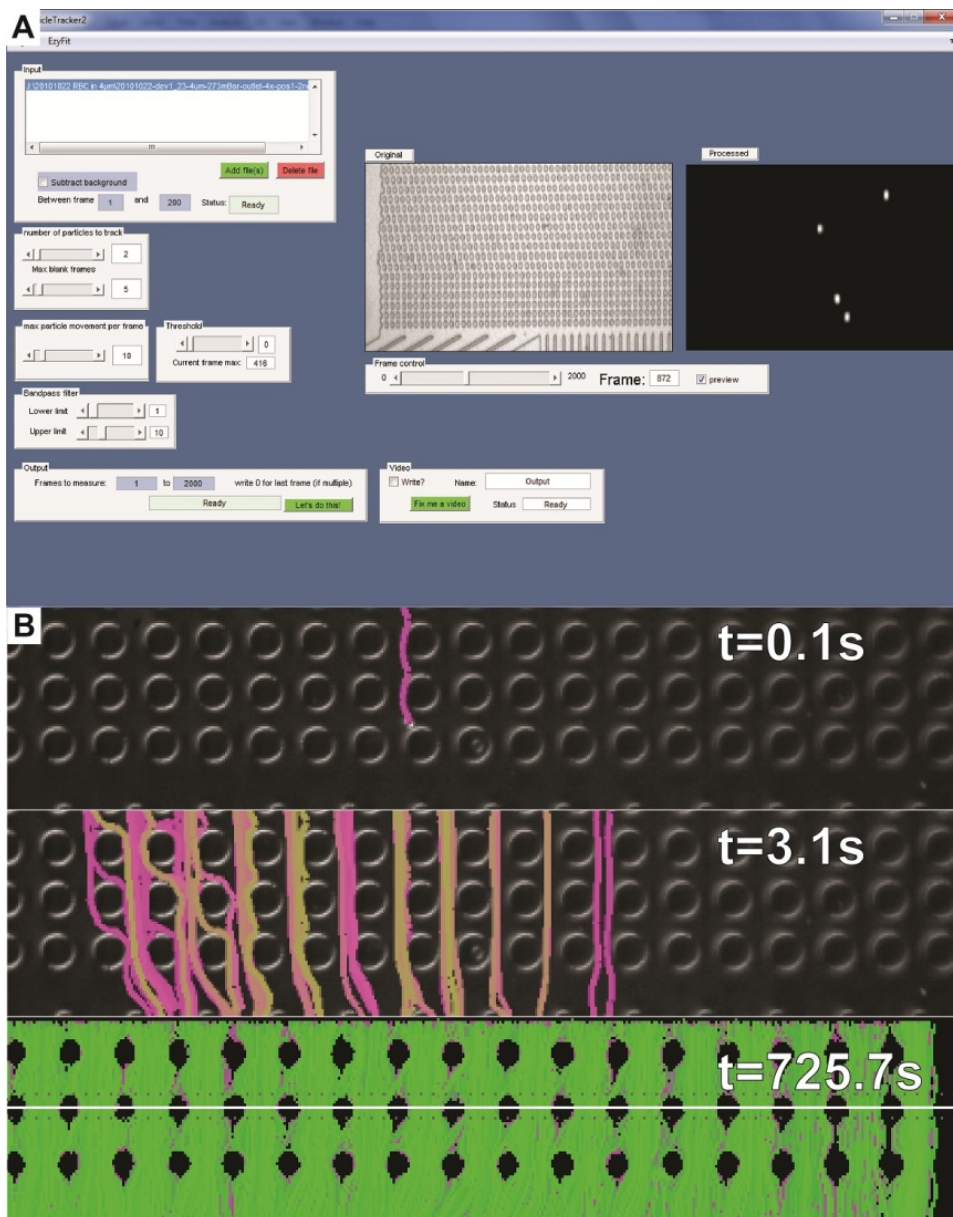


Figure 30. (A) Graphical interface of the MATLAB program used to evaluate the experiments. The original movie acquisition is shown in the center with the enhanced image with the background removed to the right. (B) Three different time steps during the analysis are shown. The particles get color-coded based on the time they enter the FOV. After the complete movie is analyzed, at 725 seconds, the measurement or the lateral displacement of the particle is conducted at the position given by the horizontal white line.

6.5 Biological methods

In the work presented in this thesis several different biological samples were used. Whole blood, washed blood, trypanosomes and samples containing a mixture of these. Careful handling is always needed for work involving biological particles as they are not static. A change in the environment, such as the surrounding medium or the temperature, can give rise to changes in *e.g.* size or shape of the cells which consequently would affect their behavior in the DLD device. All biological work was therefore carried out in a manner which would preserve the *in-vivo* characteristics of the cells as much as possible, avoiding any change in parameters such as shape, deformability or size.

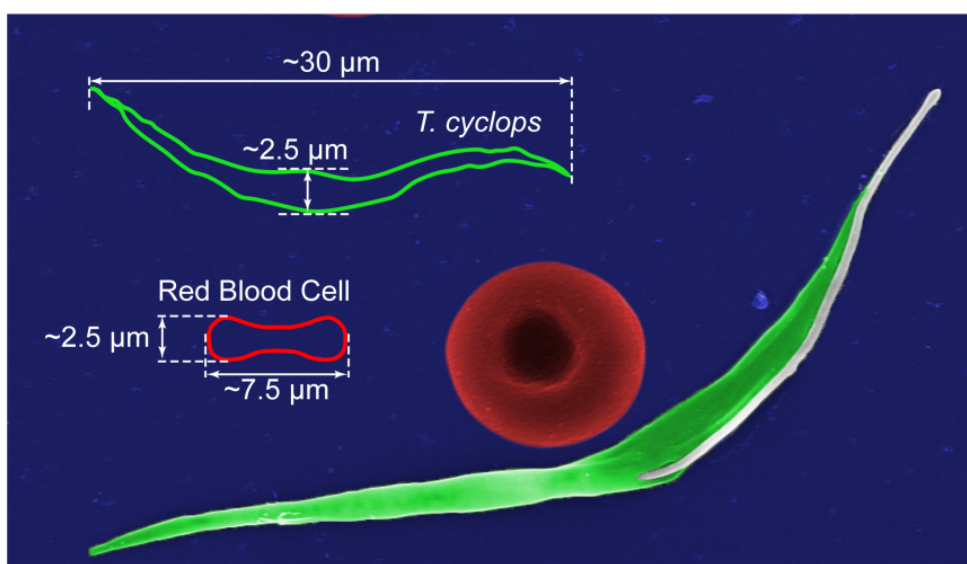


Figure 31 A colour-enhanced scanning electron micrograph of an RBC (red) and a *T. cyclops* (green), both of which are representative of the most common size and shape. The dimensions of these two are also given in the image.

6.5.1 Hematological methods

For the work involving blood, finger pricking of healthy volunteers was used. Haemic HAEMOLANCE low flow finger pricking

devices were used to puncture the tip of a finger. Around 10 μL was commonly aspirated in a pipette tip which had been dipped in a solution of autoMACS® Running Buffer (#130-091-221, Miltenyi Biotec, Bergisch Gladbach, Germany). The blood was in most cases diluted 20 times in this buffer which had been sterile filtered prior to use. The buffer contains 1% BSA to prevent unspecific adsorption, 0.09% sodium-azide for preventing bacterial growth and 2.5 mM EDTA as an anticoagulant in PBS buffer of physiological tonicity.

Different anticoagulants can be used to prevent the blood from clotting. Common substances used include heparin, EDTA and citrate which all have their own benefits and drawbacks. However, K_2EDTA have shown good performance for drawing of smaller blood samples at concentrations around 3-5 mM¹²², and consequently this would be a good anticoagulant to use in this project. The 2.5 mM EDTA in autoMACS® Running buffer was estimated to be high enough for these experiments and no addition of extra EDTA to the buffer was done.

6.5.2 Trypanosome handling

As has been discussed previously, in *Chapter 4*, trypanosomes is a taxonomic group which include, the for human pathogenic, *Trypanosome brucei* but also several other protozoan parasites which are infectious to other species. Given the high risks and regulatory constraints of working with the pathogenic *T. brucei* the work presented herein was done using a related specie, namely *Trypanosoma cyclops*¹²³. This specie is not infectious to humans, but instead the macaque monkey, *Macaca*, of South East Asia.

Cultivation of the *T. cyclops* was done at 28° C. This temperature act to promote a change on the parasites to proliferate as epimastigotes (the procyclic form found in the insect vector). This form has been described as being 33.5 μm long and 2.5 μm wide which is in agreement with the length described in the literature of *T. brucei*, 30 μm long and 1.5-3.5 μm wide.⁵⁶ The morphological similarities and the evolutionary closeness together with the much lower risks and

regulations associated with working with *T. brucei* makes *T. cyclops* an ideal model system for this work presented herein. It could be possible that properties, such as surface charge and flagellum wave form, for example, differ between *T. cyclops* and *T. brucei*, however, the method of separation in a DLD device rely primarily on the cell shape and size. Therefore, we believe that *T. cyclops* represent a legitimate model organism for the pathogenic *T. brucei* in demonstrating the separability of trypanosomes from human blood using a DLD device.

The cultivation of the trypanosomes were carried out in Cunningham's medium¹²⁴, which is a modification of the more commonly known Grace's insect medium (Invitrogen, 11605-102) to mimic the natural occurring amino acid composition of the blood stream of the vertebrate host. Splitting of a sample were done at a ratio of around 1:15 by diluting around 2 μL of trypanosomes in 23 μL of Cunningham's medium supplemented with 5 μL of fetal calf serum (FCS). The suspension was stored in culture flasks with closed lids to minimize any contamination. The internal volume of the flasks was deemed to have a large enough extra volume that the exchange of compounds with the solution is not affected during the time between splitting.

Figure 32 shows a growth curved which was obtained by counting the number of trypanosomes in a Bürker chamber. The time $t = 0$ is the time of culture splitting. After splitting the now lower concentration of trypanosomes starts to recover. In the first few days the concentration maintains fairly constant. This is usually referred to as the lag phase, a period where the cells sense the lower concentration of cells in relation to the available nutrition and are reprogrammed for growth. After this period the log phase starts with a rapid growth. A growth which continues until the plateau phase is reached. Here, the cell concentration remains steady until the nutrition in the container is depleted and the number of cells would decrease again. Usually the splitting of cells was carried out every 2 weeks, which should correspond to when the culture is in the end of the log phase. At this

time the cells should be have their highest metabolic rate and consequently they would have the maximum ability to withstand the change in environment during culture splitting.

During experiments involving samples containing both blood and trypanosomes we noticed that the trypanosomes were not motile and in fact lysed. This was found out to be a consequence of the human blood plasma which has shown capable of lysing this strand of trypanosomes. This was found to have been discussed in the work by Weinman *et al.*¹²³. To circumvent this problem and enable simultaneous measurements of blood and trypanosomes we decided to simply replace the blood plasma with the growth medium of the trypanosomes, the Cunningham's medium.

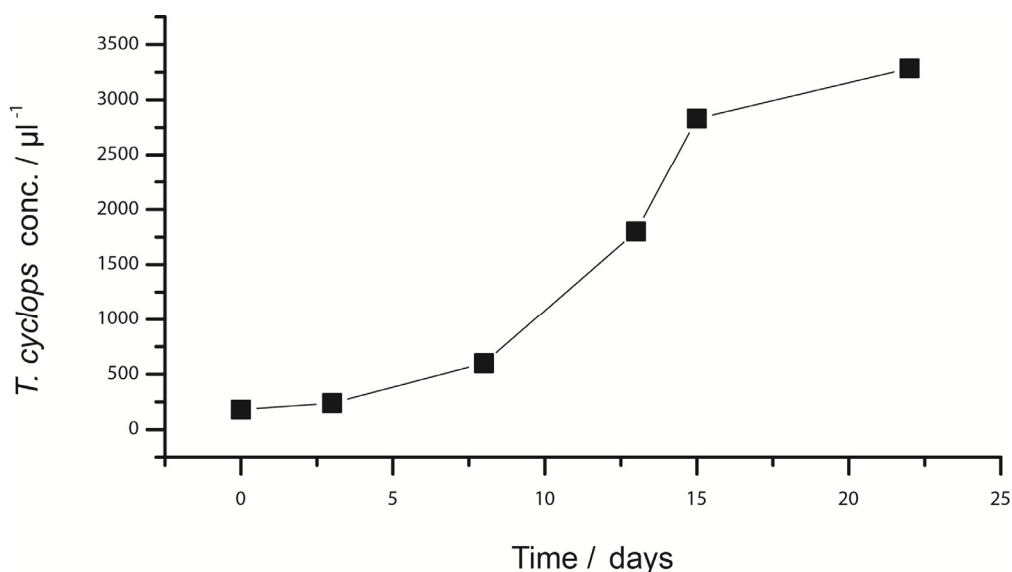


Figure 32. Plot showing a typical growth curve of the trypanosomes. After splitting of the cultivated sample at a ratio of around 1:20 the population starts to recover. The first few days the concentration maintains fairly constant, a phenomenon referred to as lag phase. After this period the log phase starts, here the large amount of available nutrition in relationship to the low concentration of trypanosomes starts a rapid growth. The growth continues until the plateau phase where the cell concentration remains steady until the nutrition in the container is depleted and the number of cells would decrease again. Usually the splitting of cells were carried out every 2 weeks, which should correspond to the end of

the log phase, this is also where the cells are strongest and most able to withstand a change of medium.

A portion of the *T. cyclops* was cryopreserved according to *Appendix 2* as a protection against any unforeseen events resulting in the loss of the culture (e.g. contaminations, medium evaporation and nutrition depletion). The procedure of freezing the parasites is advised to take place 3-5 days *post* inoculation when they are in their log-phase growth¹²⁶. This is when they are the strongest and thus most likely to survive the -80°C freezing, a state in which they can be kept stable for a long time.

6.5.3 Characteristics of *T. cyclops*

The literature reports a mean size of 33.5 µm in length and 2.5 µm in width when cultivating at 28°C. This type is most probably the epimastigote form of the parasite meaning that it is the form present in the vector and not in the host. If instead *T. cyclops* would be inoculated at 37° C in blood agar they would develop into the blood form, trypomastigote, which are characterized by having a length of 43 µm and a width of 4 µm. With the size of the most prevalent blood form of the pathogenic *T. brucei* being around 30 µm it is more equivalent to the epimastigote form of *T. cyclops* than the trypomastigote form. To mimic the *T. brucei* the *T. cyclops* was cultivated at 28° C, this had the benefit of slower maturing parasites leading to longer lifetimes and lower maintenance (e.g. longer times between changing of the media and splitting the cultures). The reported times to reach full maturation of a culture was found to be 7 (at 37° C) and 16 (at 28° C) days.¹²³

To characterize the morphology of our *T. cyclops* the lengths and widths of 160 trypanosomes cultivated for 14 days in Cunningham's medium at 28° C were examined by optical microscopy. The results are presented in *Figure 33***Error! Reference source not found.** The average measured lengths were 30.0 ± 4.4 µm, and the widths were found to be 2.5 ± 0.4 µm. The correlation between length and widths was found to be very low with a correlation coefficient of 0.14.

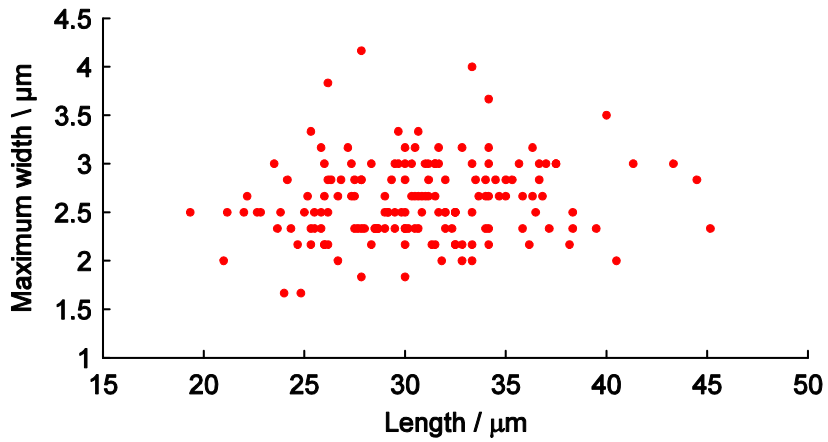


Figure 33. Scatter plot of our size measurements of 160 *T. cyclops* parasites cultivated for 14 days at 28° C. The results indicate a low correlation between length and size. The results show that it most likely is mainly epimastigotes present in the sample; however some trypanosomes are larger and could be trypomastigote.

7. Device design and characterization

As discussed in *Chapter 3*, there exists a wide range of different DLD designs, each with their own benefits and drawbacks. For the work presented here the chirped device was chosen. This device consists of several regions of increasing critical diameter. The lateral position of a particle at the end of this device is a function of its effective size.

Small flaws in the device or particle-flow interaction can give rise to stochastic effects which could lead to particles with an effective size above the critical diameter avoid being displaced. To counter this detrimental effect each section is repeated 5 times, giving rise to a more accurate separation between particles of different effective sizes. Theoretically the displacement of a particle is given by *Equation (35)* where n is the total number of sections in the device, D_{eff} the effective size of the specific particle and $D_{c,n}$ the critical size of section n . The inner parenthesis is a Boolean function equaling 1 if true and 0 if false.

$$\sum_{i=1}^n (5\lambda \cdot (D > D_{c,n})) \quad (35)$$

7.1 Device design

When designing the different arrays in the device consideration had to be taken to the limits in dynamical range which was discussed in *Section 3.4* of this thesis. The final device, with inlets and outlets, had to be able to fit on a 3 inch wafer. At the same time, the critical diameters should be of sizes relevant to the biological samples used in this work. The largest cells of the blood are the macrophages which are around 20 μm . Consequently, this was set as the upper limit of the critical diameters in the device. The lower limit was set to 1 μm giving

a dynamic range of 20. As previously mentioned, devices with dynamic range above 4-5 will be unpractically long due to the cubic relationship between the gap-to-critical size ratio and the length of the device. The result of a long device would be both that separation takes a longer time and also that the particles are exerted to stochastic effects such as diffusion and imperfect flows to a larger extent which may affect the separation efficiency negatively. Therefore, we chose to construct three separate devices with a limited dynamic range. Their parameters are listed in *Table 6* to *The final* design of the arrays is shown in *Figure 34*, with the length of the separation array differing between the devices with 45 mm for device 1 to 68 mm for device 3. The flow is from left to right with the two side inlets being used for buffers while the center inlet is for the sample acting to provide hydrodynamic focusing of the sample into a stream of around 10 μm . Before entering the actual DLD array in the device the sample flows through a filter which removes any particles which otherwise would clog the device, the filter consists of posts with the same gap size as in the array, however, clogging of the filter is much more advantageous than clogging of the array which could affect the flow symmetry.

Table 8. device 3, $\lambda=43\mu\text{m}$, $G=25\mu\text{m}$

. Each device contains several different sections, with increasing critical diameter; each section is repeated five times. For every section a large particle will be laterally displaced 1λ . Particles with an effective size larger than the critical diameter of that section will consequently be laterally displaced around 5λ . As the period is not always an integer the average displacement will sometimes deviate from being exactly 5λ .

Table 6. device 1, $\lambda=26\mu\text{m}$, $G=6\mu\text{m}$

Section	$\Delta\lambda/\mu\text{m}$	N	Rows	$D_C/$	Disp. /
1	0.4	65.3	325	1.13	129
2	0.8	32.5	160	1.58	257
3	1.4	18.5	90	2.07	383
4	2.0	13.0	65	2.45	513
5	3.0	8.7	40	2.98	633
6	4.2	6.2	30	3.50	759
7	5.6	4.6	20	4.02	872
8	7.0	3.7	15	4.47	977

Table 7. device 2, $\lambda=32\mu\text{m}$, $G=12\mu\text{m}$

Section	$\Delta\lambda /$	N	Rows	$D_C /$	Disp. / μm
1	0.8	36.71	200	2.86	160
2	1.2	26.67	130	3.47	316
3	1.6	20.00	100	3.99	476
4	2.0	16.00	80	4.44	636
5	2.6	12.31	60	5.04	792
6	3.2	10.00	50	5.56	952
7	3.8	8.42	40	6.04	1104
8	4.4	7.27	35	6.48	1258
9	5.2	6.15	30	7.02	1414
10	6.0	5.33	25	7.53	1564
11	6.8	4.71	20	7.99	1700
12	7.8	4.10	20	8.53	1856
13	8.8	3.64	15	9.04	1988

The final design of the arrays is shown in *Figure 34*, with the length of the separation array differing between the devices with 45 mm for device 1 to 68 mm for device 3. The flow is from left to right with the two side inlets being used for buffers while the center inlet is for the sample acting to provide hydrodynamic focusing of the sample into a stream of around 10 μm . Before entering the actual DLD array in the device the sample flows through a filter which removes any particles which otherwise would clog the device, the filter consists of posts with the same gap size as in the array, however, clogging of the filter is much more advantageous than clogging of the array which could affect the flow symmetry.

Table 8. device 3, $\lambda=43\mu\text{m}$, $G=25\mu\text{m}$

Section	$\Delta\lambda$	N	Rows	D_c	Disp. /
1	2.0	22.5	110	7.85	156
2	2.6	17.3	85	8.91	314
3	3.4	13.2	65	10.13	471
4	4.0	11.3	55	10.95	627
5	4.8	9.4	45	11.95	780
6	5.8	7.8	35	13.09	924
7	6.6	6.8	30	13.93	1065
8	7.8	5.8	25	15.09	1203
9	8.8	5.1	25	15.99	1360
10	10.0	4.5	20	17.00	1502
11	11.2	4.0	20	17.95	1662
12	12.6	3.6	15	19.00	1795
13	15.9	2.7	10	19.98	1914

Figure 34 shows specifically device 2, and consequently it consists of 13 sections. The trajectories of two particles have been drawn. First a small particle ($< 2.86\mu\text{m}$) has been drawn in red displaying no lateral displacement at all. The larger particle ($> 9.04\mu\text{m}$) is laterally displaced throughout the device, with its trajectory drawn in yellow. Each of the three outlet regions consists of two smaller regions, if the outlet is placed in the center of the three outlet regions then the sample is only fractionated into the three outlets, however with outlets placed in all of the six smaller regions a greater fractionation of the sample can take place, which could prove useful in the further analysis and processing of the sample.

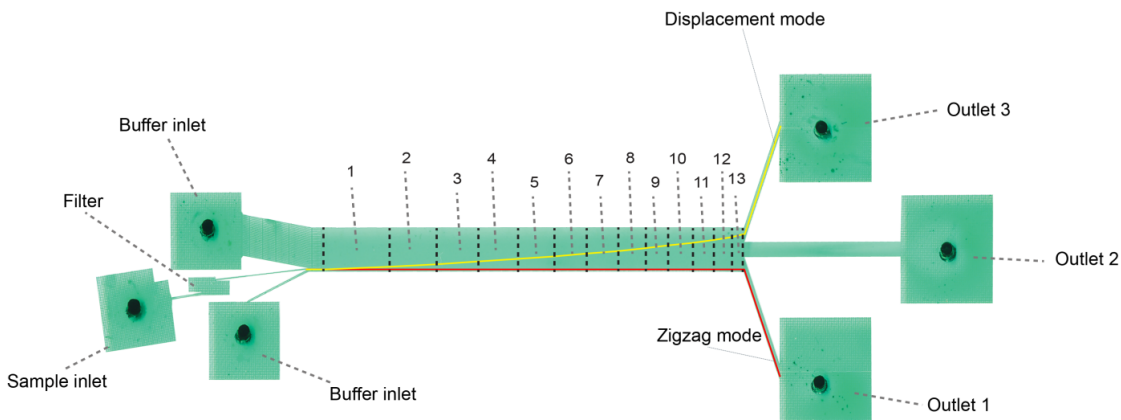


Figure 34. Device overview taken by filling a finalized device with food coloring and acquire an image by utilizing a flatbed scanner. The flow is from left to right in the image with two buffer inlets on the side of the sample inlet acting to provide hydrodynamic focusing of the sample into a stream of around $10\ \mu\text{m}$. Before entering the actual DLD arrays in the device the sample flows through a filter which act to remove any particles which otherwise would clog the device. This specific device consists of 13 sections and the trajectories of a small particle have been drawn in red, the particle is in zigzag-mode and a large particle which is in bump-mode shown in yellow. Each of the three outlet regions consists of two smaller regions; in the device shown above the outlet holes have been placed in the center of the outlet regions, acting to connect the two smaller regions. If one would like to fractionate the particles in more than three fractions for further processing the holes, up to six holes could be realized by placing the hole on each side of the barrier in each outlet region. The length of the device is around 57 mm, allowing it to fit on a normal glass slide.

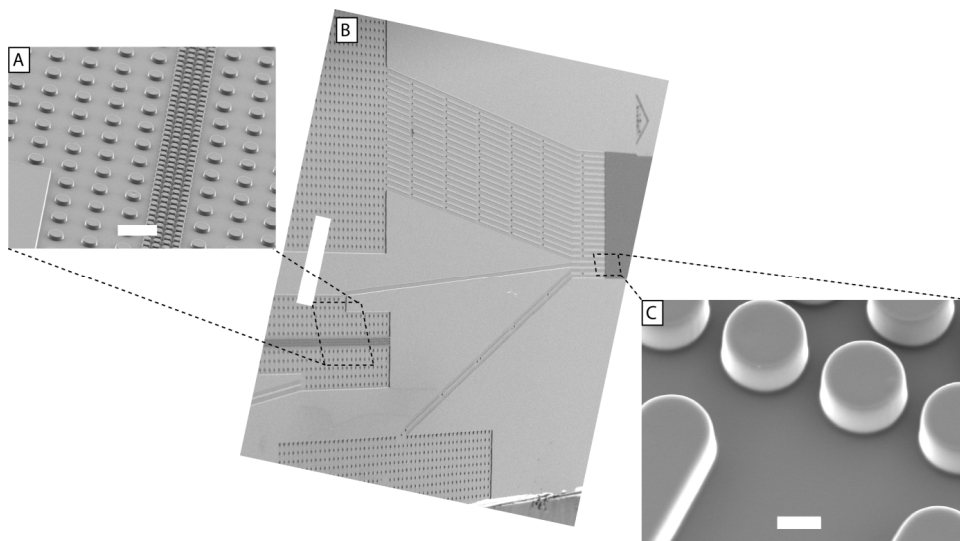


Figure 35. SEM micrographs of the device. (A) overview of the filter acting to remove any particle which otherwise would clog the device. Scale bar is $100\ \mu\text{m}$. (B) The entrance to the DLD array from the two buffer inlets on the side and the sample inlet going through the filter in the center. Scale bar is $1\ \text{mm}$. (C) Start of the array showing a close-up of the cylindrical posts. Scale bar is $10\ \mu\text{m}$.

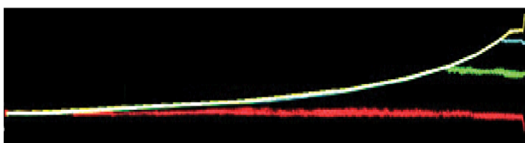
7.2 Characterization of the device performance

After finalizing the processing of the device, careful characterization of its sorting abilities was needed. In order to obtain values for what particles are displaced and what are not displaced in each section measurements of polystyrene microspheres of specific sizes were carried out. The rotation of these spherical beads does not have an effect on their behavior, unlike non-spherical particles, and further, these polystyrene particles are relatively hard compared to biological particles and consequently they should not be affected by the flow velocity, and instead their effective size is equal to their diameter.

The trajectories of five different polystyrene beads were measured in the device used for the work herein and four other polystyrene beads were used to characterize the device referred to as device 1. The result is given in *Figure 36* which has been constructed by a mosaic overlay of around 200 time integrated micrographs of the behavior of different beads. As can be seen the beads of different sizes follows the same path until they reach a section where the critical diameter is larger than

the specific bead's diameter. The devices have been compressed a factor of 10 in the horizontal direction, in reality the angles at which particles are displaced are much lower.

Device 1



Device 2

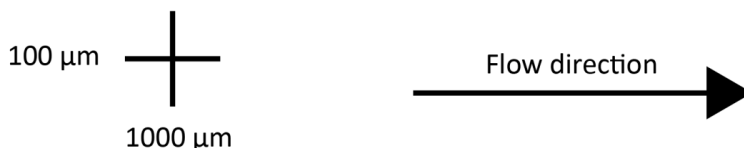
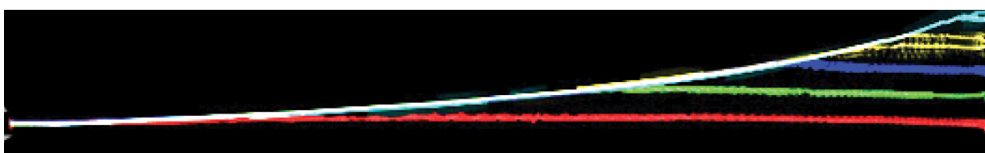


Figure 36. Mosaic overlay of around 200 time integrated micrographs showing the behavior of spherical polystyrene micro-beads in device 1 and device 2 (the device used for the remaining work presented herein). In device 2, small particles, below 3 μm, are not laterally displaced while the larger particles above 10 μm in diameter are laterally displaced in every section of the device.

Most focus has been put on device 2 as this one has the correct critical sizes for sorting of blood (3-9 μm). Consequently, the displacement of the five different polystyrene beads were measured in the outlet of the device, the results are shown in *Figure 37*. Here, a lateral displacement of 0 means that the particle has not been laterally displaced at all in the device, and consequently they end up at the same lateral position as they were introduced into the device. Above the graph is the theoretical value of the sections given. In this device with critical diameters ranging from 3-9 μm any particle below 3 μm in diameter should have a final lateral displacement of 0. At the same time a particle with e.g. a

diameter of $3.7\ \mu\text{m}$ have a diameter larger than the critical size of the first ($3\ \mu\text{m}$) and second ($3.5\ \mu\text{m}$) section. The particle should consequently end up with a lateral displacement of around $2 \cdot 5 \cdot \lambda = 320\ \mu\text{m}$ which is noted by the vertical grey line labeled $3.5\ \mu\text{m}$. If the particle was $4.3\ \mu\text{m}$ it would end up at the next vertical grey line labeled $4.0\ \mu\text{m}$ at a lateral displacement of around $3 \cdot 5 \cdot \lambda = 480\ \mu\text{m}$. The exact displacements are given in *The final* design of the arrays is shown in *Figure 34*, with the length of the separation array differing between the devices with $45\ \text{mm}$ for device 1 to $68\ \text{mm}$ for device 3. The flow is from left to right with the two side inlets being used for buffers while the center inlet is for the sample acting to provide hydrodynamic focusing of the sample into a stream of around $10\ \mu\text{m}$. Before entering the actual DLD array in the device the sample flows through a filter which removes any particles which otherwise would clog the device, the filter consists of posts with the same gap size as in the array, however, clogging of the filter is much more advantageous than clogging of the array which could affect the flow symmetry.

Table 8. device 3, $\lambda=43\mu\text{m}$, $G=25\mu\text{m}$

with small deviations due to non-integer periods.

Theoretically, in a truly deterministic device the particles can only be laterally displaced in the whole section of the device or completely flow in the general flow direction, depending on if the particle's effective size is above or below the critical size of that section. Consequently, all particles should end up at any of the lateral displacement indicated by the vertical lines in *Figure 37* which show how many sections the particles have been laterally displaced in. However, what we see is a dispersion of the outlet distribution of the particles. This is due to stochastic effects such as particle-particle interaction (which increase with increasing particle concentration), non-perfect symmetric flows (an effect of particle concentration and also the particle size and any design flaws) and diffusion (dependent on the residence time in the device).

Further, each of the different-sized beads is manufactured with a distribution of sizes. Hence, the particle sizes are given by a mean size and the corresponding standard deviation of the size distribution. In *Figure 37B*, the vertical error bars show the standard deviation for each particle size while the horizontal error bars indicate the standard deviation in the lateral displacement. It can be seen that a larger spread in the bead sizes gives rise to a wider distribution in the final lateral displacement, as expected. The specific sizes of the beads used in characterizing the device used for the work presented herein was $4.87\pm 0.12\mu\text{m}$, $6.19\pm 0.20\mu\text{m}$, (Polysciences Inc., Warrington, PA; 18340, 19102), $3.00\pm 0.15\mu\text{m}$, $7.00\pm 0.91\mu\text{m}$ and $10.00\pm 1.20\mu\text{m}$ (Duke Scientific Corp. Palo-Alto, CA; R0300, 35-2, 36-3).

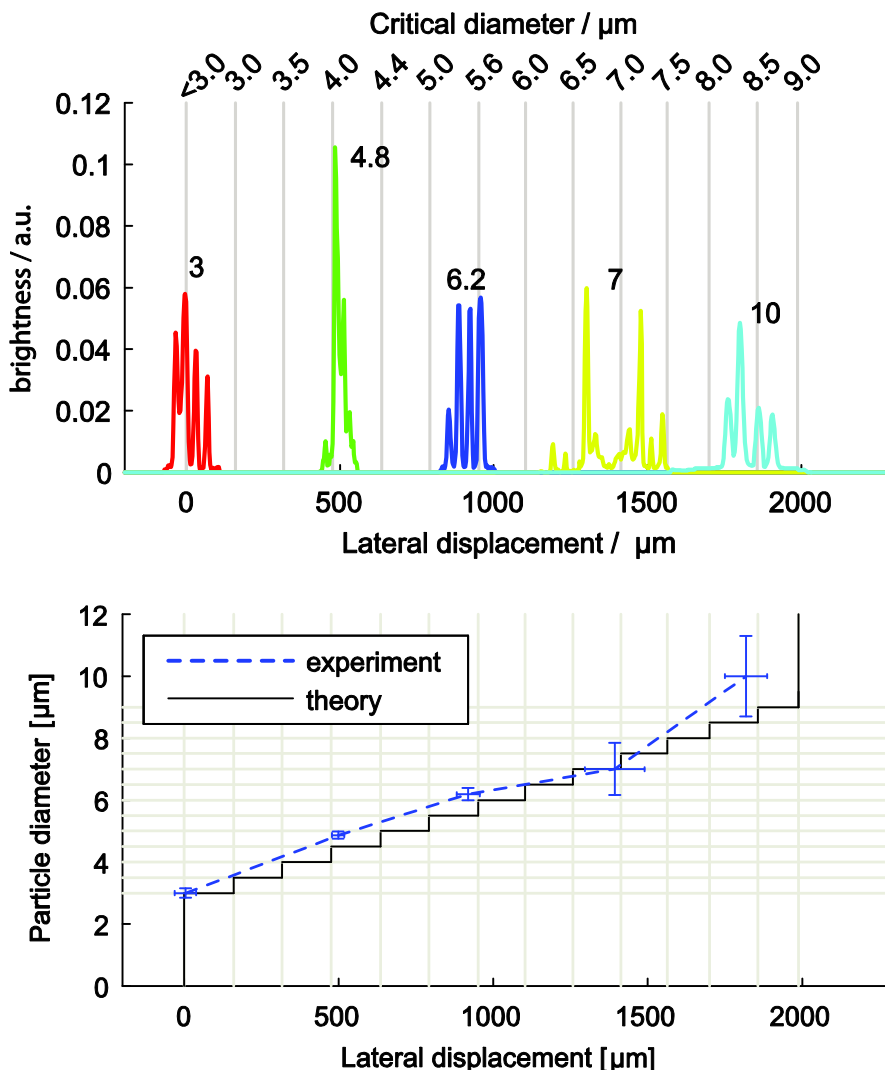


Figure 37. Characterization of the device used for the remaining work presented herein using spherical polystyrene beads of specific sizes. (A) Showing the lateral displacement distribution at the end of the device for each particle size. In general the particles are displaced less than expected by the theory, this is most notable for the large 10 μm sized particle which mean lateral displacement is corresponding to a particle of 8.5 μm . This could be an effect of the large particle-to-gap ratio which induces a large flow disturbance when it passes a gap. The 7 μm sized beads seems to split up into two different populations which could be an effect of the large size spread of this particular bead, $\text{std} = 0.91 \mu\text{m}$. The result seems to be that the critical diameter of the ninth region lies around the center of the actual bead size distribution.

When comparing the actual displacement of the particles with the calculated critical diameters it can be seen that in general the particles

are expected to be displaced further when comparing to the theory. This can be seen clearly in *Figure 37B* where the step function shows the theoretical critical diameters of the device while the blue striped line shows the experimental results. This effect seems to be most notably for the larger particles, especially the 10 μm spheres which end up with a lateral displacement of around 1900 μm , at a critical diameter of less than 8.5 μm . This could be an effect of the large particle-to-gap ratio which induces a great flow disturbance when a particle passes through a gap which in turn also could have a significant effect on surrounding particles. These large particles occupy $\sim 83\%$ of the gap, a considerable number which clearly has an effect on the flow profile of the gap.

The three smallest particles all have a mean lateral displacement which lies one section lower than expected. For example the 4.8 μm sized beads are expected to, on average, be displaced until the fifth section with a critical diameter of 5 μm . The same is true for the 3 and 6.2 μm beads, which both end up being displaced one section less than expected. The 7 μm beads have a more complex distribution where its resulting distribution is much wider with two distinct peaks. This is most likely a result of the large polydispersity of the beads with a coefficient of variation (CV) of 13%, or standard deviation (SD) of 0.91 μm . Considering this large size spread it is natural, even though from the same batch of beads, that some are displaced much further than others. The mean lateral displacement of the 10 μm beads deviates significantly from its expected lateral displacement. The mean lateral displacement is 1853 μm compared to its expected 2080. The lateral displacement corresponds to the expected displacement of an 8.5 μm sized spherical particle. This could, as has been discussed before, be an effect of the large particle-gap ratio which would induce a large disturbance to the flow field. Earlier examinations of the sizes of the polystyrene beads have shown that their distribution is not Gaussian.

8. Blood analysis

The main focus of this thesis is to detect trypanosomes in a sample. One could believe that most work should be focused on these parasites. However, careful analysis of the behavior of both blood and parasites are needed in order to achieve separation. As has been discussed earlier, the separation of RBCs and parasites would be impossible in a conventional DLD device due to their identical smallest dimension. By studying how blood behaves at different channel depths, different driving pressures and at different osmolarities of the buffer it could be possible to achieve a separation if the RBCs react differently to any of these changes in the device. Blood is a complex fluid, as has been described in *Chapter 4*, with many different constituents of varying sizes, shapes and softness. Due to the great number of RBCs in blood, and the amount of background these constitute in HAT diagnosis, these were the main focus of the work presented herein.

In the blood measurements we investigated the effects of changing the buffer, varying the pressure and varying the channel depth. The buffer was changed in order to measure how different osmolarities affect the RBCs and their behavior in the DLD device. When changing the osmolarity of the buffer, the osmosis will act to transport water either in to the cells or out from the cells depending on if the osmolarity is decreased or increased respectively. This would consequently affect the effective size of the cell and, in turn, the behavior in the DLD device. The pressure was investigated due to the fact that RBCs are highly deformable cells. A higher pressure, or driving force of the fluid, will act to increase the fluid shear forces in the device and the effective size of the RBCs are expected to decrease. The depth of the device was investigated in order to understand if the orientation of RBCs can be steered in a controlled manner. The RBCs are disc-

shaped cells with a diameter of $\sim 7.5 \mu\text{m}$ and a width of $\sim 2.5 \mu\text{m}$. A shallow channel could have the possibility of constraining the cells into a specific orientation and consequently we could have the possibility of performing shaped-based sorting.

8.1 Effect of channel depth

The same device design was used to fabricate many different devices of different channel depths, by altering the viscosity of the SU8 and the spin speed as discussed in *Chapter 6*. The behavior of blood cells was analyzed in these devices at moderate pressure ($\sim 100 \text{ mBar}$). The result of these measurements is collected and presented in *Figure 38*. It can be seen how the distribution of the RBCs are gradually changed. From having the smallest effective size in the deepest device to the largest effective size in the shallowest device. In a deep device the shear forces of the fluid is thought to align the RBCs with the posts acting to decrease their effective size. In a channel which is $12 \mu\text{m}$ deep the RBCs are allowed to rotate freely due to the diameter of the RBCs being on average $7.5 \mu\text{m}$. However, already in a device of $8 \mu\text{m}$ depth the RBCs are laterally displaced considerably. This result indicate that the alignment of particles is not a simple effect of only the channel and particle geometry but secondary effects, such as wall interactions and the aforementioned large particle-gap ratio, could induce flow disturbances. For channels shallower than the diameter the effect of increasing effective size seems more intuitive. However, many of these experiments involve relatively high flow speeds, up to $0.3 \text{ mm}\cdot\text{s}^{-1}$, yet the RBCs show no severe deformation or folding which otherwise could occur. This means that by having a shallow channel the behavior of the red blood cell is almost entirely determined by the diameter. This technique could be utilized in order to measure different dimensions of a particle and further, the deformability across the disc of a RBC and across its width can be measured separately as well as the membrane flexibility when the RBC is bent in a channel of intermediate depth.

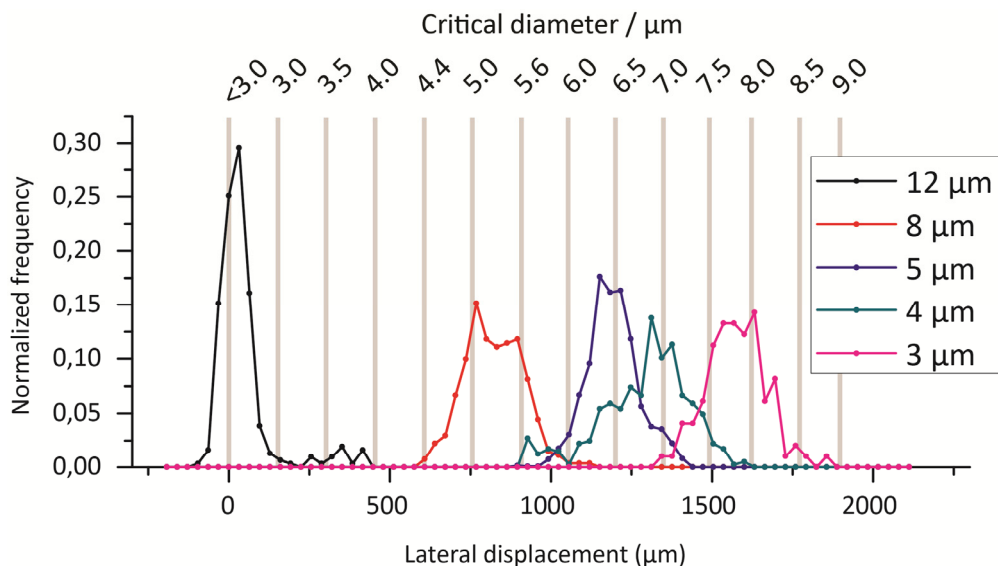


Figure 38. Outlet distribution of RBCs at different channel depths at moderate pressures ~ 100 mBar. It can be seen how the gradual increase in the RBCs effective size act to increase their lateral displacement. The increase in lateral displacement is already clearly notable at depths of around $8 \mu\text{m}$ which should be larger than the majority of the blood cells' diameters. This could be an effect of the particle-wall interaction.

8.2 Effect of pressure

Increasing the pressure difference across the device will increase the flow which in turn increases the shear stress exerted on the cells in the device. Due to the high deformability of the RBCs, one characteristic feature which increases the gas exchange as they flow through the small capillaries of the blood system, they will be compressed and consequently have a lower effective diameter. The results of these measurements are presented in *Figure 39*. Here, the depths are 5 and $8 \mu\text{m}$ respectively. At both these depths the RBCs are slightly tilted, as a result the decrease in effective size is most likely contributed to both a compression of the cell also a bending of the cell membrane, both attributed to the increased shear forces of the fluid. The effect of different depths and pressure is expected to result in the RBCs morphologies and orientations as shown in *Figure 40*.

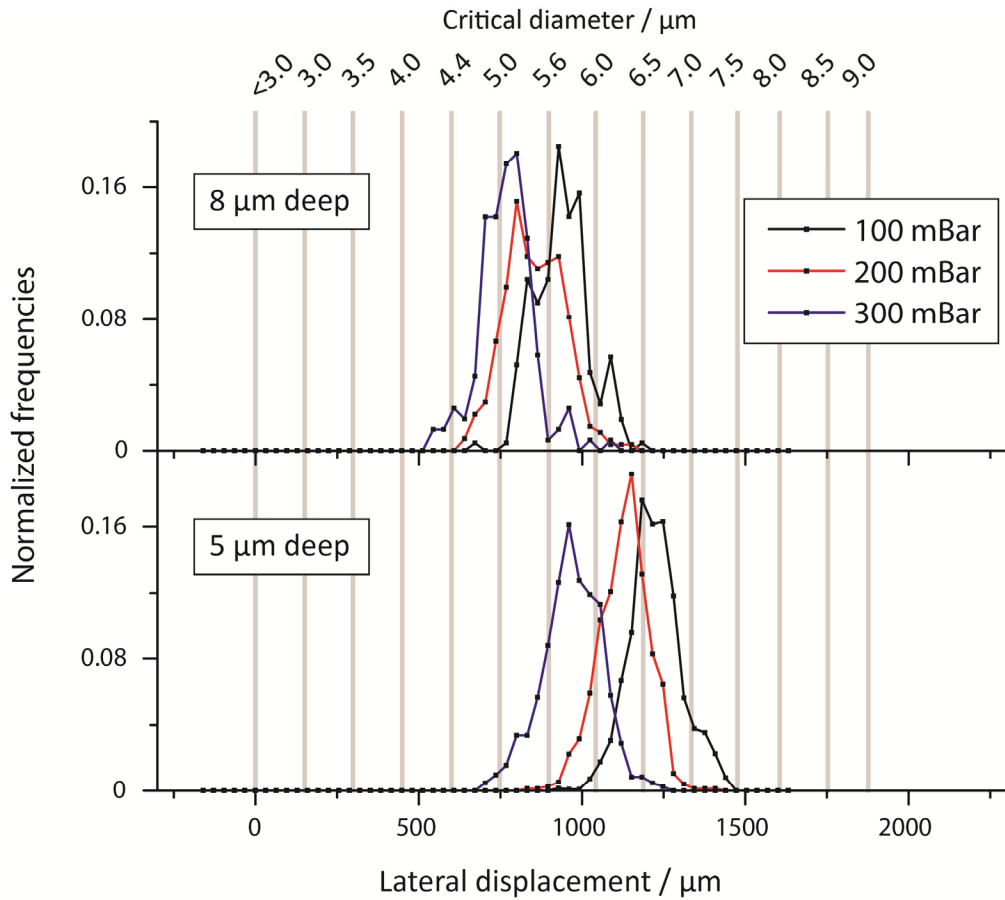


Figure 39. The effective size of soft RBCs decrease with increasing pressure difference across the device. Increasing flow speed result in an increase of the shear stress which act to compress the cells.

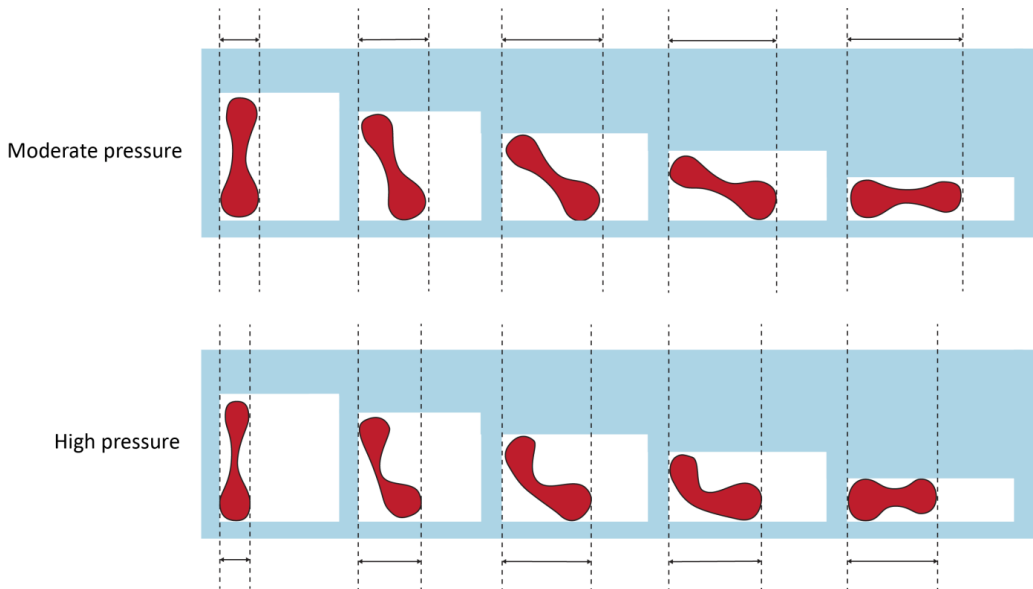


Figure 40. The expected effect of channel depth and pressures on the RBC morphology and orientation. In a device deeper than any of the cells diameter the cells tend to align themselves in the orientation which gives them the smallest effective size. For a disc-shaped cell, minimizing the channel depth gives the cells a maximized effective size. The result is that the compression of the cell occurs in different directions, which could be a valuable tool in cell diagnostics. Further, between these endpoints, deformation of these tilted cells will also result in bending of the membranes which also has been shown important in cell diagnostics.

8.3 Osmolarity measurements

In this section both the characterization of RBCs in solutions of varying osmolarities and the result of DLD analysis of these non-isotonic RBCs are presented.

8.3.1 Osmolarity and RBC morphology

To alter the effective size of cells we can manipulate them by changing the salt concentration of the solution, the osmolarity. By decreasing the osmolarity water will flow in to the cells, due to osmosis, by decreasing the osmolarity water will instead flow out of the cells. Systematic measurements were conducted of an osmolarity-range which spanned from half the osmolarity of human blood to twice the osmolarity of human blood. In a healthy person the osmolarity of the blood stream, which is often referred to as plasma osmolarity has a reference range of around 275-310 mOsm/L, or around 0.9% (w/v) NaCl. The range to be examined was hence determined to range from 140 to 600 mOsm/L.

This experimental part was carried out by measuring the size of 20 randomly chosen cells in each of the 32 different blood samples. All of the samples were freshly drawn at a volume of around 10 μL . The pipette tips were filled with 500 μL of buffer containing EDTA before pooling the sample to prevent coagulation. The sample is thereafter put into an Eppendorf tube

containing another 500 μL of the buffer supplemented with the appropriate amount of NaCl necessary to reach the target osmolarity. More detailed descriptions of the procedures are found in *Appendix 4*.

The width and diameter of a red blood cell in isotonic solution is easy to determine, the diameter across the disc is around 7.5 μm and the width of the disc around 2.5 μm . However, altering the osmolarity can result in large deformations of the cells and consequently there is sometimes no clear disc shape with a measurable diameter. Instead, during the measurements the length and width were acquired were the length was defined as the longest diameter of the cell while the width was defined as the shortest diameter of the cell. For an ideal spherical cells these parameters would be identical. For the isotonic RBCs the length is the diameter and the width would be the natural width of the disc. As the fluid flow results in a constant rotation of the cells they could be visualized from several angles and the longest and smallest diameter could be determined correctly. The longest and shortest dimension would be the two most important factors in a DLD device. The shortest diameter is expected to coincide closely with the effective size of the particle in the device while the longest diameter can have secondary effects on the effective size as well as this parameter constitute the smallest features of the device in order to avoid clogging. In *Figure 42* two common cells from the osmolarity measurements are shown. In *Figure 42A* a biconcave normal RBC at isotonic osmolarity is shown, with its diameter as the longest dimension and the width of the disc as the smallest dimension. In *Figure 42B* the decrease in osmolarity to hypotonic condition results in stomatocytes, a bowl-shaped cell. At very low osmolarities a large deformation can occur and what was formerly the longest dimension across the cell can now be the smallest dimension across the cell. Ten measurements for both the largest and the smallest dimension were registered at each of the 32 different osmolarities osmolarity. The mean and standard deviation were calculated and the result is shown in *Figure 42*.

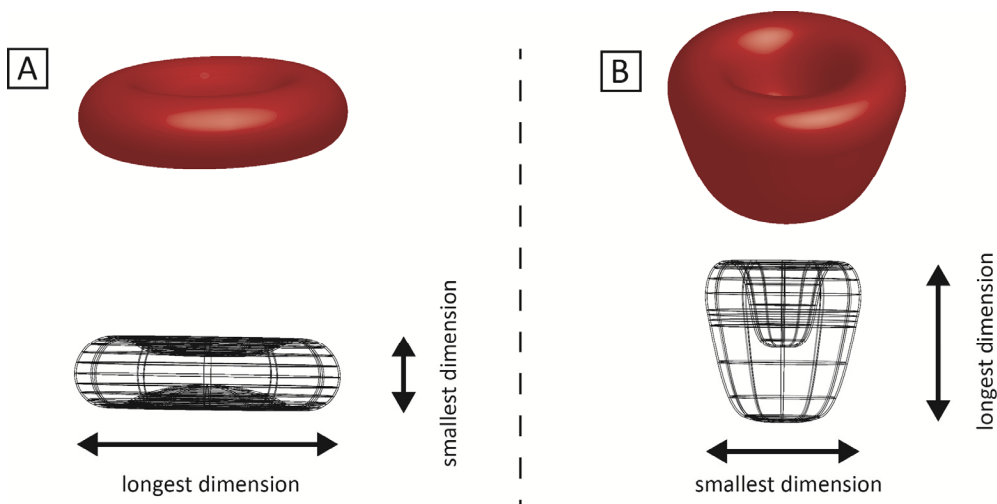


Figure 42. During the size measurements of the RBCs the longest and smallest dimension was measured. Due to heavy deformation at high or low osmolarities the resulting cell can often be non-symmetric and the former measurements of width and diameter cannot be put to use. The longest dimension is at isotonic conditions in (A) the diameter across the disc. While the smallest dimension is the width of the RBC. In (B) the hypotonic condition acts to force water into the cell acting to form stomatocytes which longest and smallest dimension does not have any relation to the initial cell. By capturing videos of rotating cells the different dimensions could be revealed and the size correctly determined.

During the examination of the different samples, it was clear that the different RBCs were affected differently by the osmolarity change as the resulting morphologies many times varied considerably within the same sample. In fact, even the isotonic sample (300 mOsm/L) had some RBCs with a morphology which resembled that of the stomatocytes or echinocytes more common in hypotonic and hypertonic samples respectively. Further, some blood cells seemed to be able to withstand the changes in osmolarity far better than the general population. These blood cells had often adhered to the glass surface which seemed to act as a solid support for the cell membrane which consequently gave rise to the ability to withstand osmolarity changes to a larger degree. These cells were not common, however they were excluded from this measurement, as only the cells free in a solution will be able to flow through and analyzed in a DLD device and hence they are the only cells which would be of importance for the work presented herein.

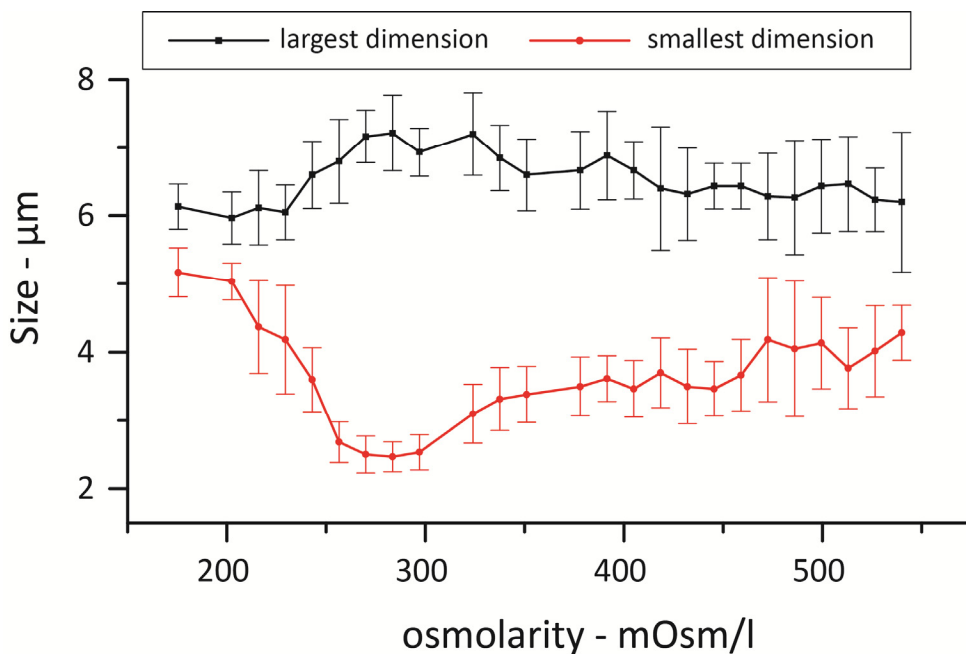


Figure 43. Our measured sizes of red blood cells in solutions of varying osmolarities as measured by direct observation in an optical microscope. Error bars represent one standard deviation in each direction.

At osmolarities below 150 mOsm/L or above 600 mOsm/L the RBCs appear as ghost cells, these are cells whose membrane has ruptured and been emptied of the cytosolic fluid and components resulting in empty membrane sacks.

The results show that at normal plasma osmolarity of 300 mOsm/L the width of the RBCs is the smallest ($\sim 2.5 \mu\text{m}$) and the diameter is the largest ($\sim 7.5 \mu\text{m}$) of all the osmolarities. Altering the osmolarity results in an increase in the width and a decrease in the diameter, *i.e.* the cells become more spherical. Especially a decrease in the osmolarity results in a rapid increase in width. While the hypertonic samples need an increase of 300 mOsm/L or twice that of isotonic conditions to reach a smallest dimension of $4 \mu\text{m}$, the mean of the hypotonic samples needs a decrease of 150 mOsm/L or half that of isotonic conditions to reach a smallest dimension of $5 \mu\text{m}$. The size distributions can be seen to generally increase with increasingly non-isotonic condition. The

manual measurements of the cell dimension can be estimated to have an error less than 0.2 μm , which is mainly attributed to the finite pixel size. Instead the size variations of the samples come from different subpopulations of erythrocytes. This is especially apparent in the hypotonic environment where the stomatocytes have a low size-variation however the error bars are large especially around 230 mOsm/L where there are essentially two different cell populations. Percentage-wise the width can be much more modified than the length; the mean width is maximally increased 107 % while the mean length is maximally decreased 17 %. This corresponds to 2.7 and 1.2 μm

8.3.2 Red blood cells analysis in deterministic lateral displacement devices under non-isotonic conditions

After initial analysis of how RBCs are affected by osmolarity changes in the surrounding medium experiments of RBCs suspended in a non-isotonic buffer in a DLD were carried out. The solutions did have a relatively low amount of NaCl (in the case of hypertonic sample) or water (in the case of hypotonic sample) added, this was both to avoid the creation of ghost cells and also to examine if the different populations could be sorted. The osmolarities to be examined were 380 mOsm/L for the hypertonic and 250 mOsm/L for the hypotonic samples. The results are presented in *Figure 44* and *Figure 45*.

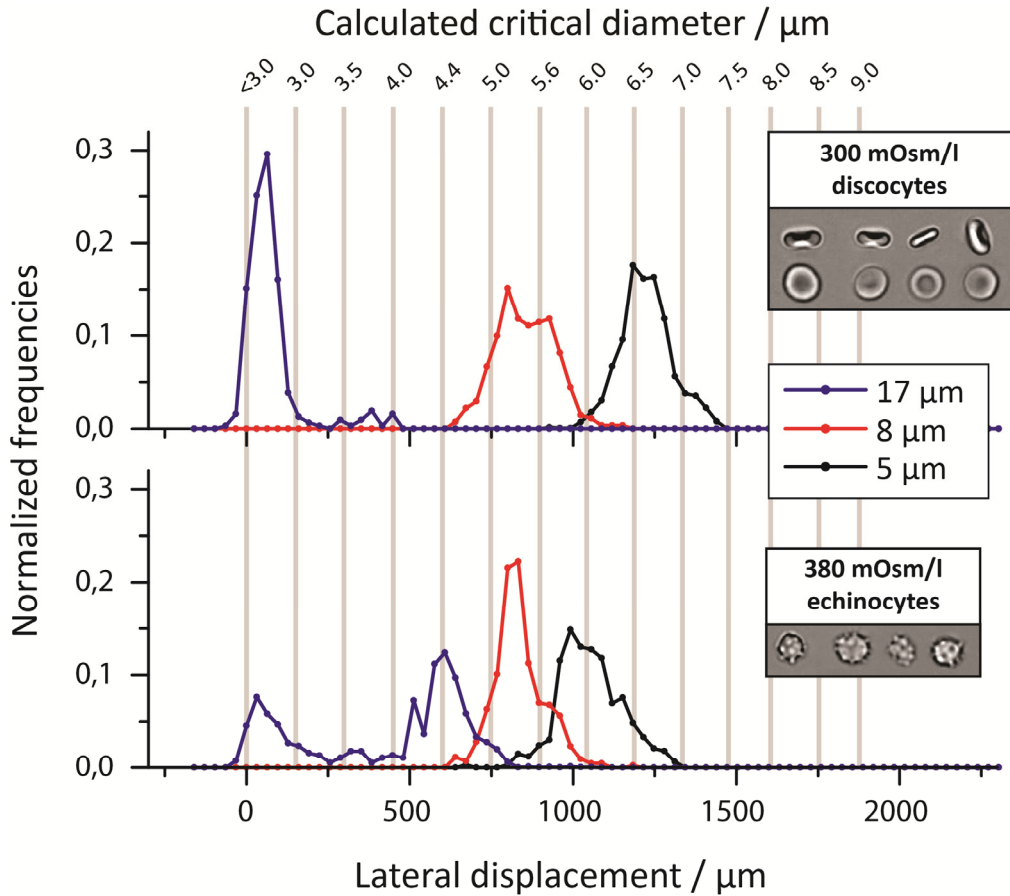


Figure 44. Isotonic (top graph) and hypertonic (bottom graph, 360 mOsm/L) samples at different depths. It can be seen how the hypertonic sample results in spiked almost spherical cells - echinocytes. The fact that they are almost spherical can be seen by how the depth of the device matters to a lesser degree on the sorting than on the isotonic discocytes. With spherical cells the orientation has no importance and consequently the behavior of the cells will not depend on the depth.

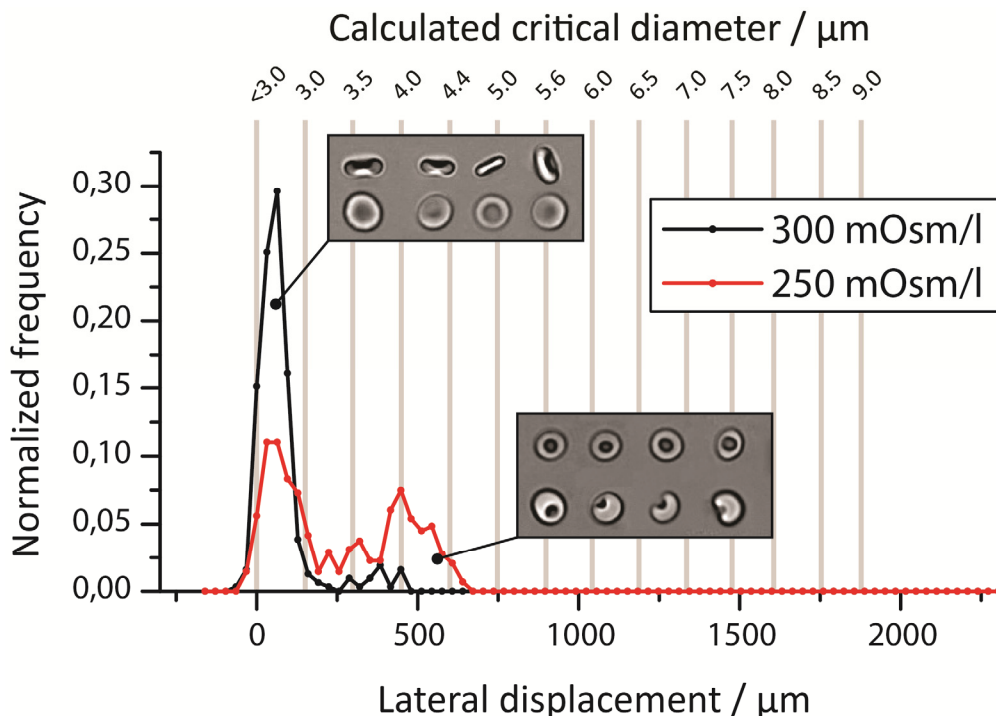


Figure 45. Isotonic and hypotonic RBCs in a 17 μm deep device. Lowering the osmolarity to 260 mOsm/L results in an increase in stomatocytes. However as has been noted before, the population is not homogenous, in fact almost half the cells are still discocytes. Decreasing the osmolarity further could have an effect on the population homogeneity. The isotonic population can be seen having a tail in the range 250-500 mOsm/L; this is mainly due to the closeness to a glass surface which has been shown of having an echinocyte-inducing effect.

Altering the osmolarity of the medium often act to result in, not only one, but two different subpopulations. Apart from the normal biconcave RBCs, which sometimes can be present even under high non-isotonic conditions, hypotonic echinocytes or stomatocytes are formed. In the DLD device it is possible to separate between these subpopulations, in *Figure 44* this can best be seen in the deep 17 μm device. This also shows how the orientation affects the effective size. For the almost spherical echinocytes in this figure the effective size is fairly close, ranging from around 5 to 6 μm . However for the disc-shaped isotonic RBCs the effective size is strongly affected by the channel depth. In a deep channel the width of the RBC determine its trajectory while in a shallow device the trajectory is determined by its

diameter. Consequently to achieve a large separation between biconcave RBCs and spherical echinocytes a deep device should be used. In *Figure 45* it can be seen how the hypotonic condition of 250 mOsm/L gives rise to a fraction of stomatocytes while around half of the population remain discocytes. The effective size of the discocytes is smaller than $\sim 3.5 \mu\text{m}$ while the effective size of the stomatocytes is around 4-5 μm . The process of filtering out old erythrocytes relies to a large extent on sorting out less-deformable cells. Old RBCs get stiffer and cannot squeeze through the small capillaries in the sinusoids of the spleen. Older and stiffer RBCs might also have an ability to withstand osmolarity changes to a larger extent than the elastic RBCs, hence the measurements would be able to discriminate based on cell age. The large part of the stomatocytes have been laterally displaced in three sections of the device giving an effective size of around 4.5 μm . Comparing with the sizes of RBCs of different osmolarities given in *Figure 43* the cells of 250 mOsm/L are in between the smallest and largest dimension of the cells. The mean smallest dimension is 3.7 μm while the largest is 6.7 μm . It was expected that the smallest dimension would equal the effective size of the cell; instead the effective size was 20% larger than the smallest size. This could be an effect of the low flow rate. A lower flow rate results in lower shear forces acting on the cells. The low shear forces might not be enough to dominate over the effect of sedimentation. Sedimentation of cells act to align the largest dimension with the channel bottom, an effect which counteracts that of the shear forces which align the smallest dimension with the pillars. More measurements conducted at higher flow rates could be done in order to verify this behavior. Also in a final device where maximizing the effective size of blood cells is needed, a decrease in osmolarity would result in a more homogenous sample with almost only stomatocytes.

9. Proof-of-principle trypanosome sorter

The initial experiments with RBCs alone, presented in *Chapter 8*, showed that osmolarity changes in the surrounding medium will affect the morphology of the RBCs and consequently have an effect on their behavior in the device. However, as also was shown, changing channel depth can also affect the behavior of RBCs in the device, and this without the need for pretreatments of the sample. It was also shown that channel depth has a greater potential in controlling the behavior of the RBCs. Changes in depth resulted in effective sizes ranging from ~ 2.5 - $8 \mu\text{m}$ and this with smaller distribution in the final lateral displacements. Consequently, the method of choice for separation of trypanosomes from blood was to optimize the device depth in order to accentuate the morphological differences to achieve the largest difference in behavior and, consequently, the highest separation possible. The experiments were carried out in two stages. First, experiments were conducted with samples of relatively high concentration of parasites ($\sim 10^6/\text{mL}$) and samples of relatively low concentration of RBCs ($\sim 10^8/\text{mL}$), in order to enable automated particle tracking and acquire good statistics of the behavior of the difference cells. The purpose of this step was to find the device depth which maximizes separation of RBCs and parasites. Once the optimum depth was found a second series of measurements was performed in order to verify that the device would also function with whole blood. The results of the first series of measurements are shown in *Figure 46*

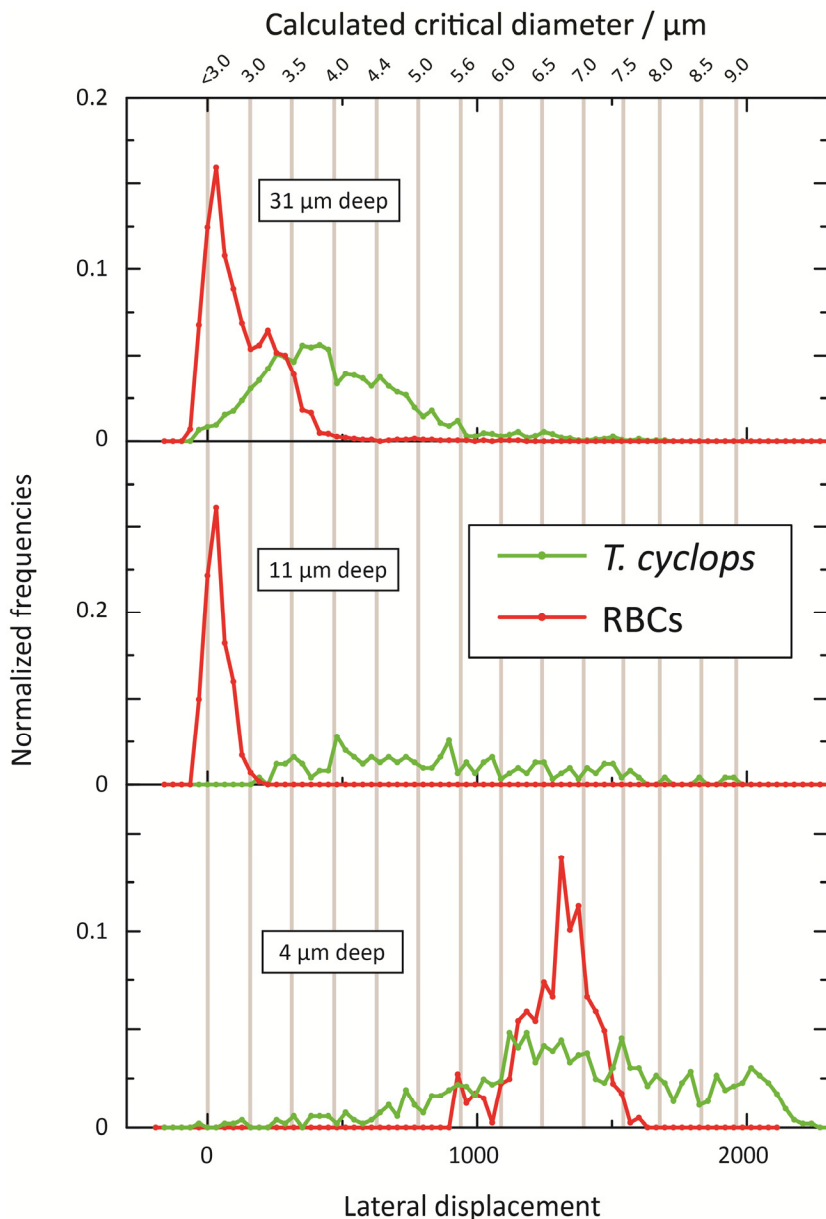


Figure 46, Graph showing the behavior of trypanosomes and RBCs at different depths. From the top in a 31 μm deep device the RBCs and trypanosomes displaced only to a certain degree and overlap to a great extent, much of the displacement is likely attributed to the smaller gaps due to imperfect SU8 processing. In the shallow 4 μm deep device in the bottom graph the RBCs and trypanosomes are both maximum laterally displaced, and also here there is a great overlap between the cell types. The center graph at 11 μm shows a minimal displacement for the RBCs due to the depth being larger than the largest dimension of the cells. At the same time this depth is smaller than the length of the trypanosomes whose rotation will be hindered and consequently they will have an increased effective size leading to a separation of the two populations.

The results show that trypanosomes in the deep device have a low effective size; most of them are being laterally displaced in the first few sections of the device, with a low critical diameter, only. However, the yet small lateral displacement which is present is believed to be an effect of the device processing which acted to create posts which were larger than normal, most likely due to overexposure or swelling of the SU8, resulting in a device with lower critical diameters than the intended. Consequently, for a device with the intended parameters at this depth, the cells are expected to be even less laterally displaced.

In the shallow device of 4 μm a considerable increase in effective size of the trypanosome can be seen. This is similar to the behavior RBCs display in shallow channels; however, for the morphologically complex trypanosomes it is not entirely an effect of the orientation of the cell. In general three different types of modes with which the trypanosomes travels through the device can be identified, shown in *Figure 47*.

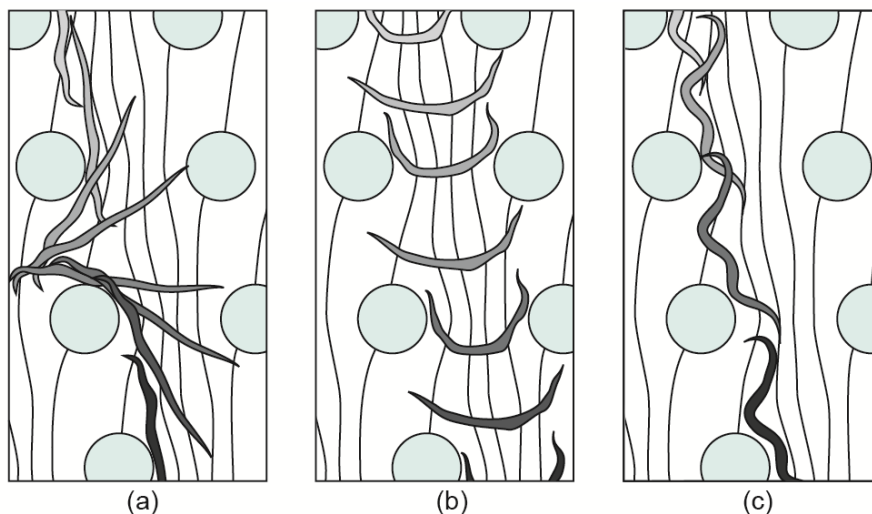


Figure 47. Trypanosome modes leading to an increase in their effective size. Flow is downwards in the image. (A) Due to their great length and their, to some extent, stiff body they will be affected by several flow stream, even though their width is smaller than the first flow stream nearest the posts. (B) The trypanosomes can get trapped in a U-shaped mode with which they can travel through the whole device getting laterally displaced in every section. (C) The constant undulation of the parasites can act to shift their hydrodynamic center of mass into the second flow stream, also resulting in an increase lateral displacement. Used with permission from the Royal Society of Chemistry.

Comparing the results from analysis of the trypanosomes behavior in the deep and the shallow device with the sorting of blood in these devices shows that neither of them are able to separate RBCs and trypanosomes efficiently. In the deep device, blood is following the overall flow direction making their outlet distribution overlap the one of the trypanosomes to a great extent. For the shallow device blood is laterally displaced in most sections of the device, ending up with a mean displacement of around 1600 μm , however, the large distribution of the trypanosomes act to suppress separation.

In the final run with whole blood spiked with trypanosomes, in an 11 μm deep device, the separation was maintained highly sensitive, as can be seen in *Figure 48*. What also can be seen is the separation of white blood cells, who seem to be, in large part, separated from the

trypanosome fraction. This could be used to further increase separation efficiency in the future.

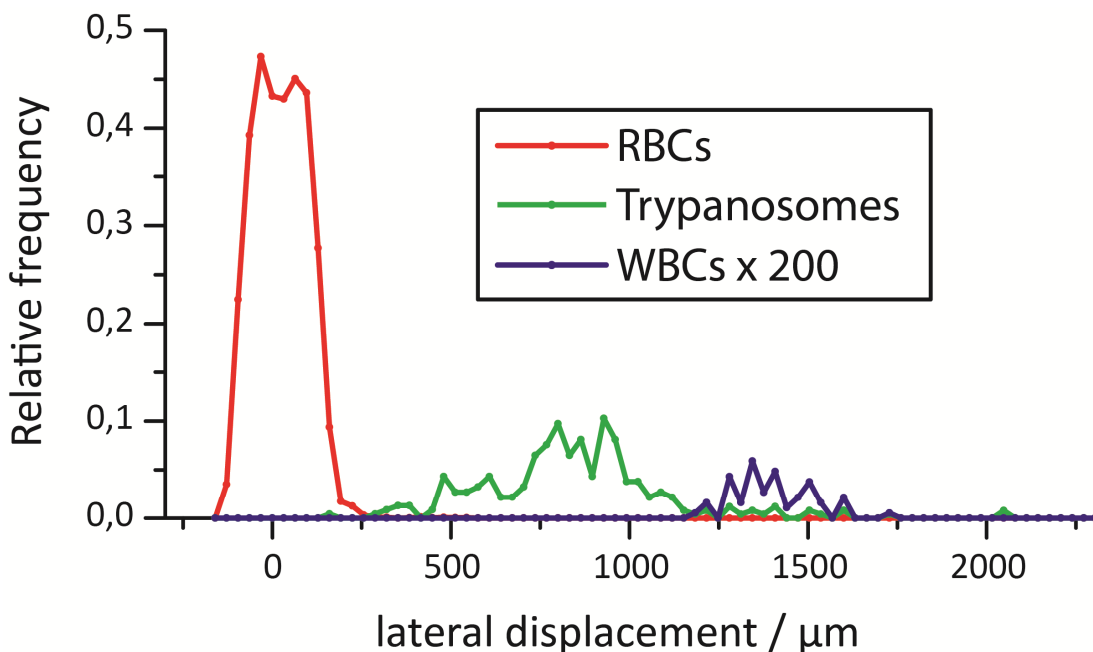


Figure 48. Experiments involving parasites in whole blood in an 11 μm deep device. It can be seen that the high concentration of RBCs act to increase the distribution slightly, however, the trypanosome display a displacement in agreement with earlier measurements and the separation efficiency is maintained at a high level.

It was evident from these initial tests that the trypanosomes would not be laterally displaced less than the RBCs, another approach was instead used where the depth was as shallow as possible, to maximize the displacement of the trypanosomes, while still being larger than the largest dimension of the RBCs, $\sim 7.5 \mu\text{m}$. This was tested and the result is shown in Figure 46B, where the behavior of blood and parasites at a depth of 11 μm is shown. All the trypanosomes were found to be laterally displaced to some degree. By superimposing the displacement of the RBCs in the same graph it can be found that the overlap is far less at this depth. The first section in the device seems to have a critical diameter which is able to separate the biconcave RBCs from the trypanosomes. Every detected trypanosome (out of >3000) was displaced in this section while only 0.8% of the RBCs were laterally

displaced more than 320 μm . It would also be possible to detect cells being displaced in at least two sections; in this case no RBCs were present (out of > 6000) while 98.3 % of the trypanosomes were detected. It would just be necessary to analyze a larger sample volume in order to account for the loss of a small fraction of the trypanosomes; a 2% larger volume would be enough to compensate for the lowered sensitivity.

The detection limit of trypanosomes with simple microscopic methods is 5000/mL as shown in *Table 3* and the concentration of trypanosomes in the body ranges from 100 to 10 000 per mL. The increase in concentration which needs to be done should reflect the chances of finding it in a blood smear given the visible surface fraction calculated in *Table 4*. As different cells in the blood take up different areas in the blood smear, a large WBC is better to sort out than a smaller thrombocyte to get the best detection. This needs to be accounted for in the calculations which can be done by estimating the visible surface of a trypanosome to $60 (\mu\text{m})^2$, which is slightly larger than the visible surface of the RBCs. If the detection limit is 5000 trypanosomes per mL blood then the lowest visible area fraction which has to be occupied by trypanosomes is given the area of 5000 trypanosomes divided by the total amount of area in the 1 mL of blood smear. The area fraction which need to be achieved is 0.13%, which can be compared to the fraction which the trypanosomes take up at 100/mL, 0.0025%. This means that the visible area fraction of the trypanosomes needs to be increased 52 times in order for a sample of a trypanosome concentration of 100/mL to be able to be detected under a normal microscope.

If we assume that we are only sorting the RBCs from the trypanosomes, which is an underestimation, we can use *Equation (36)* to calculate the fraction of RBC needed to be sorted out

$$S = \frac{51}{52} \frac{(A_i + A_t)}{A_{RBC} \cdot C_{RBC}} \quad (36)$$

Where A_i is the initial visible area per volume of blood and A_t is that of the trypanosomes, A_{RBC} is the visible area per RBC and C_{RBC} is their initial concentration. This gives that if no other cell types are being sorted out 99.1% of the RBCs need to be removed. As discussed above, no RBC ended up at a displacement corresponding to being laterally displaced in both of the first two sections.

Assuming Poisson statistics, at 100 trypanosomes per mL the volume needed to be analyzed for having a maximum of 1 false negative per million positive is 137 μL , or 140 μL when taking the trypanosomes which cannot be detected into account as mentioned above, see *Figure 49*.

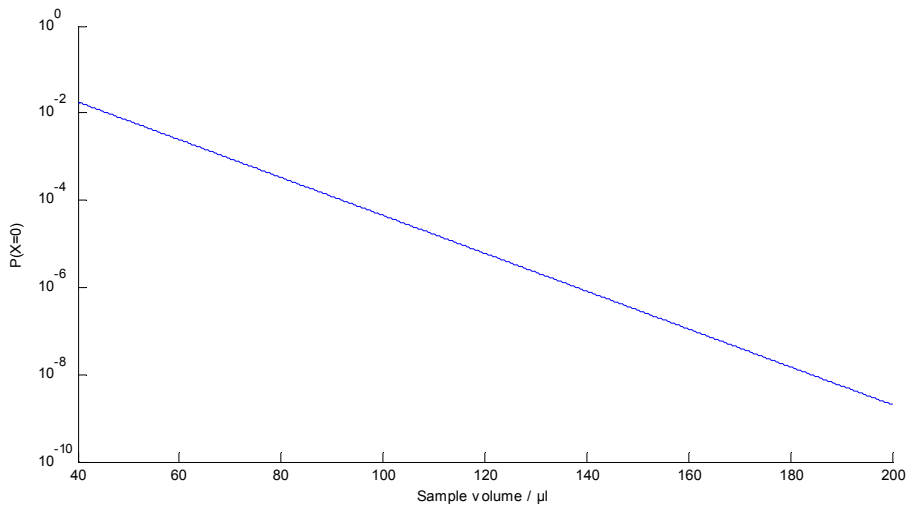


Figure 49. Assuming Poisson statistics, the probability of a false positive given a certain volume of blood is analyzed. The larger volume the lower is the risk of giving a wrong diagnosis. For one false negative per 1 million positive the required volume to analyze is 137 μl .

10. Conclusions

The successful separation of parasites and human blood was achieved without the need for pretreatment of the sample or changes in the osmolarity of the solution in order to induce shape changes to the cells. Instead, the method which was chosen as the best option for separation was to optimize the channel depth. This was used in order to accentuate the morphological differences of the cells to achieve efficient separation. The device depth which gave the cells the largest difference in behavior was slightly above the diameter of the RBCs, 11 μm . This was the shallowest depth tested where the RBCs still displayed their smallest effective size. This effective size was below the critical diameters of all the different sections in the device and consequently they were not laterally displaced to a significant degree. The orientation of the longer trypanosome parasites is however, at this depth, hindered and consequently they may not decrease their effective size to the same degree. However, it should be noted that the parasites have a much more complex shape than the biconcave, disc-shaped RBCs and the increase in effective size is an effect of several factors. First the long parasites constantly rotates, between the subsequent rows, while it travels through the device and consequently it crosses several different flow streams which affects its resulting trajectory in the device. Secondly, the parasites can travel in a U-shape throughout the device trapped between two posts. Third, the constant undulation of the parasites results in a shift in the hydrodynamic centre of mass out from the posts, acting to increase the effective size of the parasites. In the future more device depths could be tested which lies in between 8 μm and 11 μm . At 8 μm a significant lateral displacement of the RBCs was shown in *Chapter 8*, however, there could be a depth between this depth and the one which gave best separation in the experiments

conducted here, 11 μm . Lowering the depth further could act to increase the effective size of the trypanosomes while still maintaining a minimal effective size of the RBCs.

For a final device both enrichment and detection of the parasites needs to be incorporated. Enrichment needs to be conducted due to the very low concentration of parasites, making detection hard even if the large background has been removed. A simple way to achieve enrichment of parasites is to construct a sieving structure with small enough pores to restrict passage for the parasites, which hence would clog at this section, enabling a region where detection can be performed.

The current device was intended as a proof of principle of separation of trypanosomes from human blood, diagnosis would currently not be possible within reasonable time limits due to the low throughput of around 1nL/s. Redesigning the device could however have the potential to increase the throughput considerably. The next generation of devices would only be constituted by arrays having the same parameters as the second array in the current device, *i.e.* where the actual separation occurred. This section has a period of 32.5 and is consequently 1.04 mm in length per period. With the same length restrictions the inlet could be widened by a factor of 60, see *Figure 50*. Further, a mirroring of the array could be constructed further increasing the throughput by a factor of 2. These changes together with parallelization by stacking ten devices on top of each other would result in an increased throughput by a factor of ~ 1200 , which means that the throughput is around 1.2 $\mu\text{L/s}$. Consequently a diagnosis, of 140 μL of blood, would take less than 2 minutes.

In a final device detection of the parasite needs to be considered. The current separation of parasite could be extended to enrichment which would make read-out easier. Enrichment of the parasites could be done by having a sieving structure in the trypanosome outlet. The sieving structures could be made out of posts with minimal gaps between them, making any trypanosomes entering this region clog. Different

surface treatments in the trypanosome outlet could also be used in order to promote surface immobilization. If this area is maximum the size of one field-of-view (FOV) a camera could be mounted and read-out easily be made here. A cell-phone based microscope could be used, such as the ones developed by the Ozcan group.¹³¹ These would have the possibility to send the result of an analysis to a trained expert located elsewhere to get accurate diagnosis.

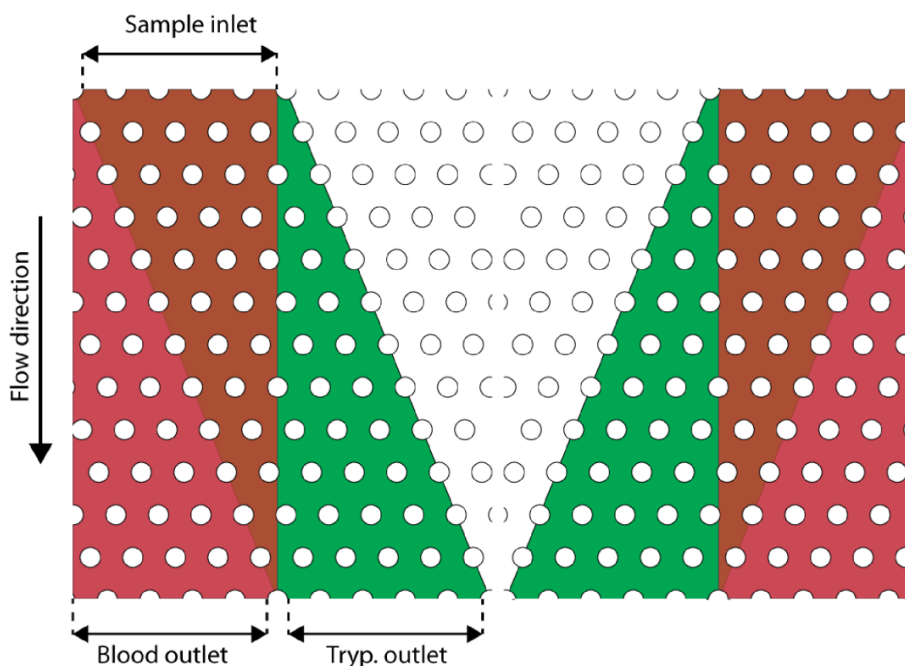


Figure 50. Widening of the inlet act to increase the throughput. A wider inlet will also require longer devices in order for complete separation to occur as shown in the image. The length restriction of the device puts a limit to the maximum inlet width. Here not only the inlet has been widened but the array has been mirrored, acting to further increase the throughput by a factor of 2.

A further question which needs to be solved in order to achieve a functional device is how the pressure will be applied. The current setup with the MFCS-2 cannot be considered portable. Normal syringes would be ideal but the sensitivity of the device to pressure differences makes this difficult to implement. An idea is to construct a device with a single inlet comprised of the enrichment followed by separation

approach described in *Chapter 3*. This device could be driven by a simple syringe due to its single inlet.

The device presented herein was shown to achieve high sensitive sorting between RBCs and parasites by optimization of the channel depth. The great potential of the device stems to a large part that the separation is based on hydrodynamic interactions. No external field is needed, and consequently the device could be driven without a power source, for example by a simple syringe. Consequently, a high sensitive device, capable of field-detection of sleeping-sickness could be achieved.

Appendix 1. Sample preparation

A1.1 Drawing blood samples

- Prick finger with Haemedic HAEMOLANCE low flow
- Fill a pipette tip with 190 μL AutoMACS running buffer
- Aspirate one large drop of blood ($\sim 10 \mu\text{L}$)
- Pipette down and up in an Eppendorf tube to homogenize the liquids
- Add around 20 μL into the sample inlet reservoir of the device

A1.2 Trypanosome samples

- Use log-phase growth trypanosomes, 5-7 days since last split
- Fill a 1.5 mL Eppendorf tube with 1 mL of trypanosome culture
- Wash sample twice at 1000 g for 1 min to exchange medium to autoMACSTM
- Pipette 20 μL of trypanosomes into the inlet reservoir
- Use autoMACSTM in the other inlets

A1.3 Simultaneous analysis

- Pool a 1 mL trypanosome sample at 1000g for 1 min, wash twice and re-suspend in 100 μL autoMACSTM
- Aspirate 160 μL of autoMACSTM in a 200 μL pipette tip
- Prick finger with Haemedic Haemolance[®] low flow
- Aspirate 40 μL of blood with the filled pipette tip into the Eppendorf tube
- Wash blood sample three times with autoMACSTM at 1000 RCF for 1 min, re-suspend pellet with 20 μL of the trypanosome sample
- Add the samples to the inlet reservoir

A1.3 Staining of T. cyclops

- Dilute the DAPI stock solution to 50 $\mu\text{g}/\text{mL}$
- Fill an Eppendorf tube with 1mL trypanosome sample
- Add 10 μL of the DAPI solution to the trypanosomes, pipette up and down to mix, cover with aluminum foil and let rest for 45 minutes

- Stop staining by washing three times in autoMACS™

A1.4 DiI staining of RBC

- Draw 10 μL of blood through finger pricking
- Wash 3 times with 200 μL PBS
- Re-suspend pellet in 200ul PBS
- Add 2 μL DiI, incubate on ice 25 min
- Wash 3 times and re-suspend in 200 μL autoMACS + 3 μL Pluronics

A1.5 Preparation of Cunningham's medium from dry salt

- Add the ingredients of group 1 and 2 to two separate autoclaved glass bottles. Dissolve the dry salts in 900 mL milliQ water and use magnetic stirrers at a moderate speed overnight
- Combine the solutions
- Dissolve 1.16 % (w/v) phenol red
- Add 10M NaOH slowly until pH 7.4 is reached. Colour should be cherry red
- Filter sterilize using vacuum through 0.22 μm filter into autoclaved bottles
- Store at 4⁰C
- Add FCS, 20% (v/v) before use

Appendix 2. Handling of *T. cyclops*

A2.1 Freezing

- Harvest cells by centrifuging log₁₀ phase culture (i.e. 5–7 days since last split) at 1000 g for 10min
- Aspirate medium and re-suspend cells in Cunningham's medium containing 20% Fetal Calf Serum (FCS) which has been preheated to 28°C. The final volume should be chosen to reach a concentration of $\sim 7 \cdot 10^7$ cells/mL
- Slowly add 10% Dimethyl sulfoxide (DMSO) while stirring
- Transfer cells to autoclaved cryotube, wrap with parafilm
- Encapsulate tube with foam rubber to protect cells from freezing too rapidly, place package in a Styrofoam box in freezer at -80°C

A2.2 Reactivation

- Heat Cunningham's medium with 20% FCS to 28°C
- Take out the tube from freezer and immerse immediately in 28°C warm water, shake tube while still immersed in water
- Rinse outside of tube with tap water followed by rinsing with ethanol
- Transfer cell suspension to autoclaved 50 mL Falcon tube. Add 10 mL medium at a rate of 1 mL/minute drop by drop. The remaining 40 mL can be added faster

A2.3 Culture splitting

(every 14 days)

- Autoclave culture flasks
- Sterilize laminar flow hood and gloves with 70% EtOH, allow to air dry for 30s
- Add 20% FCS to the Cunningham's medium, heat to 28°C
- Fill each culture flask with 19 mL
- Use sterile pipettes to transfer 1 mL of trypanosome suspension to each culture flask
- Collect another 1 mL of suspension to perform cell counting

- Store the culture flasks in a sterile environment at 28°C

Appendix 3. Device fabrication

A3.1 UV lithography

- Rinse and sonicate mask in acetone for 2 min followed by IPA for another 2 min
- Dry with Nitrogen gas

- Bake Silicon wafers in oven for at least 30 min at 200°C
- Spin Coat SU8 for 10s at 500rpm minimum acceleration followed by 45s at a suitable speed to obtain desired SU8 thickness
- Soft bake for 1 min at 65°C followed by 2 min at 95°C

- Relax for 2 min, test for wrinkling to assure proper soft baking time
- Expose at a time corresponding to the correct dose with the current lamp intensity, with a 30% increase due to blocking with I-line filter
- Post exposure bake for 1min at 65°C followed by 3-4 min at 95°C, depending on thickness
- Develop in SU8 Developer for 6min stir fluid a bit to keep SU8 from settling on the wafer again. Sonication might be needed to get proper development of high aspect ratio structures
- Rinse in fresh developer followed by IPA, if the wafer turns white it means it is under developed
- Dry with Nitrogen Gas

- Hard Bake in Oven for 30min at 200°C

- Image
- Anti-sticking is done by applying f13tfs for 3 h at 175°C, Use glove box with cloth gloves. Insert sample to load lock. Follow pump down instructions. Open from inside. Place sample in petri dish on hot plate to one side. Place petri dish top with hole away from wafer. Inject 70 μ L of antisticking for a 4" petri dish. Place a small square of glass over the whole. Clean syringe in hexane and dispose of hexane stuff.
- Measure height using Profilometer

A3.2 Soft Lithography

- Mix PDMS and hardener (Dow Corning, Sylgard) 10:1
- Place in desiccator for 30 min
- Pour carefully on wafer, avoid bubble formation
- Make planar PDMS surfaces by spin coating PDMS on a glass slide 30s at 800rpm
- Bake for 1h
- Plunge hole for in and outlets
- Bond the pieces together by using oxygen plasma
 - Evacuate chamber to $6 \cdot 10^{-1}$ mBar
 - Ventilate oxygen at 8 mBar for 60s
 - Close oxygen valve, wait till pressure has dropped, flow Nitrogen at 10mbar for 60s
 - Wait till pressure has dropped and then ventilate to atmospheric pressure
- Fill channel with milliQ or 0.1% PLL-g-PEG depending on if polystyrene beads or cells are to be used
- Glue the inlets, let harden for 1h

A3.3 Preparation for SEM of RBC and trypanosomes

- Collect cell sample (blood and/or trypanosomes)
- Wash twice with PBS
- Replace cell sample liquid with cacodylate buffer, leave for 2 hours.
- Wash sample 3 times in PBS
- Dehydrate the cell sample by increasing the ethanol content of the buffer gradually
 - Remove PBS and replace with 50% EtOH, leave 3 minutes
 - replace with 75% EtOH, leave 3 minutes
 - replace with 95% EtOH, leave 3 minutes
 - replace with 100% EtOH
- Perform critical point drying if necessary according to manual
- Sputter the sample to coat with gold, see manual

Appendix 4. Osmolarity Measurements

All of the samples were freshly drawn at a volume of around 10 μL . The pipette tips were filled with 500 μL of autoMACSTM buffer before pooling the sample to help prevent coagulation as much as possible. This is done due to autoMACSTM containing EDTA which is a chelating agent acting to deplete the solution of calcium ions crucial for the platelets during clot formation, or thrombosis.^{132, 133} The sample is thereafter put into a tube containing another 500 μL of autoMACSTM as well as the amount of NaCl needed to produce the desired osmolarity.

Some cells did not move with the flow during analysis, instead they seem to have been immobilized on the glass surface. It might be that they have adhered to the surface and this could cause them to be able to resist any osmolarity-induced conformation change. It would then be necessary to neglect these blood cells as indicative of how typical red blood cells behave at the osmolarity in question. Instead focus should be directed towards the freely flowing cells.

The buffer which was used consisted of isotonic PBS with supplements of 0.5% BSA and 5 mM EDTA. This is a common mixture when working with blood due to its tonicity being close to physiological, it has a pH of 7.4 which is the same as blood and it has good anticoagulant properties¹³². BSA has a molecular weight of 66.4 kDa making the 0.5% solution contribute with around 0.075 mOsm/L, a neglectable small amount. Consideration has to be taken with the EDTA which is stored as a disodium salt in its dry state. Upon dissolving it in the PBS the EDTA will contribute with three times the number of particles per volume giving rise to an increase of the osmolarity with 15mOsm/L. The initial PBS solution had an

Appendix 4: Osmolarity Measurements

osmolarity of 285 mOsm/L giving the resulting solution an osmolarity of 300 mOsm/L.

Table 9. *Solution preparation*

<i>Osmolarity (mOsm/L)</i>	<i>milliQ addition (μL)</i>	<i>30% (w/w) NaCl addition (μL)</i>
0	<i>Pure milliQ</i>	0
150	1000	0
165	818	0
180	667	0
195	539	0
210	429	0
225	333	0
240	250	0
255	177	0
270	111	0
285	53	0
315	0	4,8
330	0	9,7
345	0	14,7
360	0	19,6
375	0	24,7
390	0	29,7
405	0	34,9
420	0	40,0
435	0	45,3
450	0	50,6
465	0	55,9
480	0	61,3
495	0	66,7
510	0	72,3
525	0	77,8
540	0	83,4
555	0	89,1
570	0	94,8
585	0	100,6

The first row of data shows an osmolarity of 0 meaning that the solution was pure milliQ water, thus in this specific sample no autoMACS was used at all. In the other half of the measurements the hypertonic samples were added with a 10% solution of NaCl to obtain the desired osmolarity as shown in table 2. The amount needed can be calculated as follows

$$v_1 O_1 + v_2 O_2 = (v_1 + v_2) O_3 \leftrightarrow v_2 = v_1 \frac{O_3 - O_1}{O_2 - O_3}$$

where v_1 and v_2 are the initial sample volume and the volume of salt needed. O_1 , O_2 and O_3 are the different osmolarities of the solutions.

When calculating the osmolarity of the salt solution consideration has to be taken to the fact that the number of moles in the final solution is twice as high as the moles of salt with 100% dissociation of the salt. This is often referred to as the dimensionless Van Hoff't factor, i . With NaCl having a molecular weight of 58.44 the final osmolarity of a 10% (w/v) salt solution is hence given by

$$O = \frac{m \cdot i}{M_w \cdot v} = \frac{10 \cdot 2}{58.44 \cdot 0.1} [mOsm/l] = 3422 [mOsm/l]$$

Applying this to formula (1) we can derive the required volumes of salt solution v_2 as a function of the desired osmolarities O_3 , the results are given in table 2.

$$v_2 = 1000 [ul] \frac{O_3 [l/mOsm] - 300}{3422 - O_3 [l/mOsm]}$$

Appendix 5. MATLAB and Java code

A5.1 Particle tracker

```
function varargout = particleTracker2(varargin)

gui_Singleton = 1;
gui_State = struct('gui_Name',       mfilename, ...
                  'gui_Singleton',  gui_Singleton, ...
                  'gui_OpeningFcn', @particleTracker2_OpeningFcn, ...
                  'gui_OutputFcn',  @particleTracker2_OutputFcn, ...
                  'gui_LayoutFcn',  [], ...
                  'gui_Callback',   []);
if nargin && ischar(varargin{1})
    gui_State.gui_Callback = str2func(varargin{1});
end

if nargin
    [varargout{1:nargout}] = gui_mainfcn(gui_State,
varargin{:});
else
    gui_mainfcn(gui_State, varargin{:});
end
% End initialization code - DO NOT EDIT

% --- Executes just before particleTracker2 is made visible.
function particleTracker2_OpeningFcn(hObject, eventdata,
handles, varargin)

% Choose default command line output for particleTracker2
handles.output = hObject;
% Update handles structure
guidata(hObject, handles);
% UIWAIT makes particleTracker2 wait for user response (see
UIRESUME)
% uiwait(handles.figure1);
% --- Outputs from this function are returned to the command
line.
function varargout = particleTracker2_OutputFcn(hObject,
eventdata, handles)
varargout{1} = handles.output;
% --- Executes on slider movement.
```

```
function slider1_Callback(hObject, eventdata, handles)
a=round(get(handles.slider1,'Value'));
set(handles.slider1,'Value',a);
set(handles.edit1,'String',num2str(a));
handles=updateGraphs(handles);
guidata(hObject,handles);
% --- Executes during object creation, after setting all
properties.
function slider1_CreateFcn(hObject, eventdata, handles)
if isequal(get(hObject,'BackgroundColor'),
get(0,'defaultUicontrolBackgroundColor'))
    set(hObject,'BackgroundColor',[.9 .9 .9]);
end
function edit1_Callback(hObject, eventdata, handles)
%get the string for the editText component
a = get(handles.edit1,'String');
%convert from string to number if possible, otherwise returns
empty
a = str2num(a);
%if user inputs something is not a number, or if the input is
less than 0
%or greater than 100, then the slider value defaults to 0
if (isempty(a) || a < get(handles.slider1,'Min') || a >
get(handles.slider1,'Max'))

    set(handles.edit1,'String',get(handles.slider1,'Value'));
else
    set(handles.slider1,'Value',a);
end
[handles]=updateGraphs(handles)
guidata(hObject,handles);
function edit1_CreateFcn(hObject, eventdata, handles)
if ispc && isequal(get(hObject,'BackgroundColor'),
get(0,'defaultUicontrolBackgroundColor'))
    set(hObject,'BackgroundColor','white');
end
function checkbox1_Callback(hObject, eventdata, handles)
handles = updateGraphs(handles);
guidata(hObject,handles);
% --- Executes on slider movement.
function slider2_Callback(hObject, eventdata, handles)
set(hObject,'Value',round(get(hObject,'Value')));
set(handles.edit2,'String',get(hObject,'Value'));
if((get(handles.slider3,'Value')<get(hObject,'Value'))&&(get(
handles.slider2,'Value')<40))
    set(handles.slider3,'Value',get(hObject,'Value')+1)
    set(handles.edit3,'String',get(hObject,'Value')+1)
elseif(get(handles.slider3,'Value')<get(hObject,'Value') &&
(get(handles.slider2,'Value')>39))
    set(handles.slider2,'Value',39)
    set(handles.edit2,'String',39)
```

```
        set(handles.slider3,'Value',40)
        set(handles.edit3,'String',40)
    end
handles=updateGraphs(handles);
guidata(hObject,handles);
% --- Executes during object creation, after setting all
properties.
function slider2_CreateFcn(hObject, eventdata, handles)
    if isequal(get(hObject,'BackgroundColor'),
get(0,'defaultUicontrolBackgroundColor'))
        set(hObject,'BackgroundColor',[.9 .9 .9]);
    end
        guidata(hObject,handles);
function edit2_Callback(hObject, eventdata, handles)
function edit2_CreateFcn(hObject, eventdata, handles)
    if ispc && isequal(get(hObject,'BackgroundColor'),
get(0,'defaultUicontrolBackgroundColor'))
        set(hObject,'BackgroundColor','white');
    end
% --- Executes on slider movement.
function slider3_Callback(hObject, eventdata, handles)
set(handles.slider3,'Value',round(get(hObject,'Value')));
set(handles.edit3,'String',get(hObject,'Value'));
if (get(handles.slider2,'Value')>get(hObject,'Value')    &&
(get(handles.slider3,'Value')>1)
    set(handles.slider2,'Value',get(hObject,'Value')-1)
    set(handles.edit2,'String',get(hObject,'Value')-1)
elseif (get(handles.slider2,'Value')>get(hObject,'Value')    &&
(get(handles.slider3,'Value')<2)
    set(handles.slider2,'Value',0)
    set(handles.edit2,'String',0)
    set(handles.slider3,'Value',1)
    set(handles.edit3,'String','1')
end
handles=updateGraphs(handles);
guidata(hObject,handles);
function slider3_CreateFcn(hObject, eventdata, handles)
set(hObject,'Value',10);
    if isequal(get(hObject,'BackgroundColor'),
get(0,'defaultUicontrolBackgroundColor'))
        set(hObject,'BackgroundColor',[.9 .9 .9]);
    end
function edit3_Callback(hObject, eventdata, handles)
function edit3_CreateFcn(hObject, eventdata, handles)
    if ispc && isequal(get(hObject,'BackgroundColor'),
get(0,'defaultUicontrolBackgroundColor'))
        set(hObject,'BackgroundColor','white');
    end
% --- Executes on button press in pushbutton2.
function pushbutton2_Callback(hObject, eventdata, handles)
global sortedMatrix histad
```

Appendix 5: MATLAB and Java code

```
set(handles.pushbutton14, 'Visible', 'on');
sizes=size(get(handles.listbox3, 'String'));
nbrOfFiles=sizes(1);

sortedMatrix=zeros(1:1:nbrOfFiles);
for listNumber=1:nbrOfFiles
    [sort
 handles]=fixAndTrack(get(handles.listbox3, 'String'), [str2double
 (get(handles.edit9, 'String'))
 str2double(get(handles.edit10, 'String'))], str2double(get(handles.edit4, 'String')), str2double(get(handles.edit2, 'String')),
 str2double(get(handles.edit3, 'String')), str2double(get(handles.edit8, 'String')), handles, listNumber);
    sizeSort=size(sort);
    sortedMatrix(1:sizeSort(1), 1:4, listNumber)=sort;
vel=[];

    if listNumber==nbrOfFiles ||
get(handles.checkbox9, 'Value')==0
    [handles N X]=updateGraphs2(handles, sortedMatrix);

        eval(['assignin(''base'', ''N'' num2str(listNumber)
 ''', 'N');'])
        eval(['assignin(''base'', ''X'' num2str(listNumber)
 ''', 'X');'])
        histad=[];
    end
end

set(handles.edit11, 'String', 'Ready');
guidata(hObject, handles)
function slider4_Callback(hObject, eventdata, handles)
set(hObject, 'Value', round(get(hObject, 'Value')))
set(handles.edit4, 'String', get(hObject, 'Value'))
handles=updateGraphs(handles);
guidata(hObject, handles)
function slider4_CreateFcn(hObject, eventdata, handles)
if isequal(get(hObject, 'BackgroundColor'),
get(0, 'defaultUiControlBackgroundColor'))
    set(hObject, 'BackgroundColor', [.9 .9 .9]);
end
function edit4_Callback(hObject, eventdata, handles)
function edit4_CreateFcn(hObject, eventdata, handles)
if ispc && isequal(get(hObject, 'BackgroundColor'),
get(0, 'defaultUiControlBackgroundColor'))
    set(hObject, 'BackgroundColor', 'white');
end
function edit5_Callback(hObject, eventdata, handles)
function edit5_CreateFcn(hObject, eventdata, handles)
```

```
if ispc && isequal(get(hObject,'BackgroundColor'),
get(0,'defaultUicontrolBackgroundColor'))
    set(hObject,'BackgroundColor','white');
end
function listbox3_Callback(hObject, eventdata, handles)
handles=updateGraphs(handles);
function listbox3_CreateFcn(hObject, eventdata, handles)
if ispc && isequal(get(hObject,'BackgroundColor'),
get(0,'defaultUicontrolBackgroundColor'))
    set(hObject,'BackgroundColor','white');
end
% --- Executes on button press in pushbutton3.
function pushbutton3_Callback(hObject, eventdata, handles)
global bgImage imageNames imwidth imheight histad
% this is to check if this is the first file being added
if isempty(get(handles.listbox3,'String'))
    itWasEmpty=1;
end
[input_file,pathname] = uigetfile( ...
    {'*.tif', 'Tiff (*.Tif)'; ...
    '*.*', 'All Files (*.*)'}, ...
    'Select files', ...
    'MultiSelect', 'on');

%if file selection is cancelled, pathname should be zero
%and nothing should happen
if pathname == 0
    return
end

%gets the current data file names inside the listbox
inputFileNames = get(handles.listbox3,'String');

%if they only select one file, then the data will not be a
cell
%if more than one file selected at once,
%then the data is stored inside a cell
if iscell(input_file) == 0
%    checks to see if the file is already in the list
    if isempty(find(ismember(inputFileNames,
fullfile(pathname,input_file))==1, 1))
        %add the most recent data file selected to the cell
containing
        %all the data file names
        %stores full file path into inputFileNames
        inputFileNames{end+1} =
fullfile(pathname,input_file);
    else
        place=find(ismember(inputFileNames,
fullfile(pathname,input_file))==1);
```

Appendix 5: MATLAB and Java code

```
        eval(['warndlg('' fullfile(input_file) ' finns redan
i listan! På plats: ' num2str(place) '')']);

    end

%else, data will be in cell format
else
    exists=[];
    for n = 1:length(input_file)
        % checks to see if the file is already in the
list
        temp=find(ismember(inputFileNames,
fullfile(pathname,input_file{n}))==1, 1);
        if isempty(temp)
            %notice the use of {}, because we are dealing
with a cell here!
            inputFileNames{end+1} =
fullfile(pathname,input_file{n});
            else
                if(isempty(exists))
                    eval(['exists=[] num2str(temp) '''])
                else
                    eval(['exists=[exists ', ' ' ' '
num2str(temp) '''])
                end
            end
        end
        if isempty(exists)==0;
            eval(['warndlg(''Hittade dublett(er) i listan på
följande platser: ' exists '')']);
        end
    end

%updates the gui to display all filenames in the listbox
set(handles.listbox3, 'String',inputFileNames);

%make sure first file is always selected so it doesn't go out
of range
%the GUI will break if this value is out of range
set(handles.listbox3, 'Value',1);

imageName=get(handles.listbox3, 'String');
if(get(handles.checkbox6, 'Value'))

bgImage=medianBG(imageNames, str2num(get(handles.edit14, 'Strin
g')), str2num(get(handles.edit16, 'String')),handles);
end
handles=updateGraphs(handles);
% update framenumbers
handles = setFrameNbr(handles);
```

```
% update slider:

    maxInt=(max(max(imageNames{1,1})));
    if(get(handles.slider4, 'Value')>round(maxInt)+1)
        set(handles.slider4, 'Value', round(maxInt)+1)
        set(handles.edit4, 'String', round(maxInt)+1)

    end

% set image height
temp=double(imread(imageNames{1,1}));
imwidth=length(temp(1,:));
imheight=length(temp(:,1));
set(handles.edit13, 'String', imheight)

% subtract background

% make single outputchoice visible if multiple input files
are chosen
if size(inputFileNames,2)>1
    set(handles.checkbox9, 'Visible', 'on')
end
guidata(hObject, handles);

function handles = setFrameNbr(handles)
    fileNames=get(handles.listbox3, 'String');
    info
    =
imfindo(fileNames{get(handles.listbox3, 'Value'),1});
    num_images = numel(info);
    global imgSize
    imgSize=[info(1).Width info(1).Height];
    set(handles.edit9, 'String', 1);
    set(handles.edit10, 'String', num_images);
    set(handles.slider1, 'Max', num_images);
    set(handles.text3, 'String', num_images);
    maxValue=get(handles.slider1, 'Max');
    minValue=get(handles.slider1, 'Min');
    set(handles.slider1, 'SliderStep', [1/maxValue 10/maxValue])
% --- Executes on button press in pushbutton4.
function pushbutton4_Callback(hObject, eventdata, handles)
% hObject      handle to pushbutton4 (see GCBO)
% eventdata    reserved - to be defined in a future version of
MATLAB
% handles      structure with handles and user data (see
GUIDATA)
%get the current list of file names from the listbox
inputFileNames = get(handles.listbox3, 'String');

%get the values for the selected file names
```

Appendix 5: MATLAB and Java code

```
option = get(handles.listbox3, 'Value');
%is there is nothing to delete, nothing happens
if (isempty(option) == 1 || option(1) == 0 ||
isempty(inputFileNames))
    return
end
%erases the contents of highlighted item in data array
inputFileNames(option) = [];
%updates the gui, erasing the selected item from the listbox
set(handles.listbox3, 'String', inputFileNames);
%moves the highlighted item to an appropriate value or else
will get error
if option(end) > length(inputFileNames)
    set(handles.listbox3, 'Value', length(inputFileNames));
end

% Update handles structure
guidata(hObject, handles);
function handles = updateGraphs(handles)
    global bgImage
    fileName=get(handles.listbox3, 'String');
    if(isempty(fileName))
        warndlg('Choose file first!');
        return
    else
        axes(handles.axes1)
        % dra av bg om rutan är ikryssad
        if(get(handles.checkbox6, 'Value'))
            img =
double(imread(fileName{get(handles.listbox3, 'Value'), 1}, get(h
andles.slider1, 'Value')))-bgImage;
            img(img<0)=0;
        else
            img =
double(imread(fileName{get(handles.listbox3, 'Value'), 1}, get(h
andles.slider1, 'Value')));
        end
        colormap('gray'), imagesc(img);
        set(handles.axes1, 'Ytick', []);
        set(handles.axes1, 'Xtick', []);

        if(get(handles.checkbox1, 'Value'))
            axes(handles.axes2)
            imgBp =
bpass(img, get(handles.slider2, 'Value'), get(handles.slider3, 'V
alue'));
            maxInt=max(max(imgBp));
            if(maxInt>get(handles.slider4, 'Max'))
                set(handles.slider4, 'Max', round(maxInt)+1)
            end
        end
    end
end
```

```

        %           thresholding
        imgBp(imgBp<get(handles.slider4,'Value'))=0;
        colormap('gray'), imagesc(imgBp);
        set(handles.axes2,'Ytick',[]);
        set(handles.axes2,'Xtick',[]);

set(handles.edit5,'String',num2str(round(maxInt)));
    end
        maxValue=get(handles.slider4,'Max');
        minValue=get(handles.slider4,'Min');
        set(handles.slider4,'SliderStep',[1/maxValue
10/maxValue])
end
function pushbutton6_Callback(hObject, eventdata, handles)
close(handles.figure1)
% --- Executes on button press in pushbutton7.
function pushbutton7_Callback(hObject, eventdata, handles)
% --- Executes on button press in checkbox2.
function checkbox2_Callback(hObject, eventdata, handles)
% --- Executes when figure1 is resized.
function figure1_ResizeFcn(hObject, eventdata, handles)
% --- Executes on button press in pushbutton8.
function pushbutton8_Callback(hObject, eventdata, handles)
% --- Executes on slider movement.
function slider8_Callback(hObject, eventdata, handles)
set(hObject,'Value',round(get(hObject,'Value')))
set(handles.edit8,'String',get(hObject,'Value'))
guidata(hObject, handles)

% --- Executes during object creation, after setting all
properties.
function slider8_CreateFcn(hObject, eventdata, handles)
if isequal(get(hObject,'BackgroundColor'),
get(0,'defaultUiControlBackgroundColor'))
    set(hObject,'BackgroundColor',[.9 .9 .9]);
end
function edit8_Callback(hObject, eventdata, handles)
function edit8_CreateFcn(hObject, eventdata, handles)
if ispc      &&      isequal(get(hObject,'BackgroundColor'),
get(0,'defaultUiControlBackgroundColor'))
    set(hObject,'BackgroundColor','white');
end
function slider7_Callback(hObject, eventdata, handles)
function slider7_CreateFcn(hObject, eventdata, handles)
if isequal(get(hObject,'BackgroundColor'),
get(0,'defaultUiControlBackgroundColor'))
    set(hObject,'BackgroundColor',[.9 .9 .9]);
end
function edit6_Callback(hObject, eventdata, handles)
function edit6_CreateFcn(hObject, eventdata, handles)
```

```
if ispc && isequal(get(hObject,'BackgroundColor'),
get(0,'defaultUicontrolBackgroundColor'))
    set(hObject,'BackgroundColor','white');
end
function checkbox3_Callback(hObject, eventdata, handles)
function slider5_Callback(hObject, eventdata, handles)
function slider5_CreateFcn(hObject, eventdata, handles)
if isequal(get(hObject,'BackgroundColor'),
get(0,'defaultUicontrolBackgroundColor'))
    set(hObject,'BackgroundColor',[.9 .9 .9]);
end
function edit7_Callback(hObject, eventdata, handles)
function edit7_CreateFcn(hObject, eventdata, handles)
if ispc && isequal(get(hObject,'BackgroundColor'),
get(0,'defaultUicontrolBackgroundColor'))
    set(hObject,'BackgroundColor','white');
end
% --- Executes on button press in checkbox4.
function checkbox4_Callback(hObject, eventdata, handles)
function slider6_Callback(hObject, eventdata, handles)
function slider6_CreateFcn(hObject, eventdata, handles)
if isequal(get(hObject,'BackgroundColor'),
get(0,'defaultUicontrolBackgroundColor'))
    set(hObject,'BackgroundColor',[.9 .9 .9]);
end
function edit9_Callback(hObject, eventdata, handles)
function edit9_CreateFcn(hObject, eventdata, handles)
if ispc && isequal(get(hObject,'BackgroundColor'),
get(0,'defaultUicontrolBackgroundColor'))
    set(hObject,'BackgroundColor','white');
end
function edit10_Callback(hObject, eventdata, handles)
function edit10_CreateFcn(hObject, eventdata, handles)
if ispc && isequal(get(hObject,'BackgroundColor'),
get(0,'defaultUicontrolBackgroundColor'))
    set(hObject,'BackgroundColor','white');
end
function [handles N X]=updateGraphs2(handles,sortedMatrix)
global histad
% histplot
% repeat for every frame(3rd dim of sortedMatrix)
files=size(sortedMatrix(1,1,:),3);
% files=files(1);
figure2=figure;
measHeight=str2num(get(handles.edit12,'String'));
stepSize=str2num(get(handles.edit8,'String'));
maximum=0;

if isempty(files)
    files=1;
end
```

```
for j=1:files
    maximum=maximum+max(sortedMatrix(:,4,j));
end

trackedSoFar=0;
for j=1:files
    i=1;
    lastrow=1;

    theEnd=find(sortedMatrix(:,4,j)==max(sortedMatrix(:,4,j)),1, '
    last');
    while i<=theEnd

        lastRow=find(sortedMatrix(lastrow:theEnd,4,j)==sortedMatrix(i
        ,4,j),1, 'last');

        plot(sortedMatrix(i:lastRow,1,j),sortedMatrix(i:lastRow,2,j),
        'Color',[1-
        1/maximum*(trackedSoFar+sortedMatrix(i,4,j)),1/maximum*(track
        edSoFar+sortedMatrix(i,4,j)),1-
        1/(maximum)*(trackedSoFar+sortedMatrix(i,4,j))]);
            hold on
            i=lastRow+1;
        end
        trackedSoFar=trackedSoFar+sortedMatrix(theEnd,4,j);
    end
    plot([get(handles.axes1,'XLim')-0.5],[measHeight
    measHeight],'w');
    plot([get(handles.axes1,'XLim')-0.5],[measHeight+stepSize/2
    measHeight+stepSize/2],':','Color',[0.4 0.4 0.4]);
    plot([get(handles.axes1,'XLim')-0.5],[measHeight-stepSize/2
    measHeight-stepSize/2],':','Color',[0.4 0.4 0.4]);
    set(gca,'Ytick',[],'Xtick',[],'YDir','reverse','Color',[0 0
    0],'XLim',[get(handles.axes1,'XLim')-
    0.5],'YLim',[get(handles.axes1,'YLim')-0.5]);

    if files==1
        NameOfFile=get(handles.listbox3,'String');
        xlabel(gca,NameOfFile{1});
    else
        xlabel('Merged output of multiple files');
    end
    lambda=str2double(get(handles.edit25,'String'));
    %% % map of particles
    figure3 = figure;

    pxlRatio=lambda/str2double(get(handles.edit24,'String'));
    for j=1:files
        Gets the horisontal positions at the measuring height
```

```

binToRows=(outletGraph(sortedMatrix(:, :, j), measHeight, stepSize,
str2num(get(handles.edit23, 'String')), str2double(get(handles.edit24,
'String')), str2num(get(handles.edit22, 'String'))));
    histad=[histad; lambda*binToRows(:, 1) binToRows(:, 2)];

end

X=[(str2num(get(handles.edit22, 'String'))-
1/2)*lambda:lambda:(round(max(histad)/Lambda+1)+0.5)*lambda];
if length(X)==1
    X=[X X+lambda]
end

% self hist
Xself=[-Inf X Inf];
Nself=zeros(1, length(X))
v=Nself;
vLat=v;
for a=1:length(Nself)
    counts=find(histad(:, 1)>Xself(a)+lambda/2 &
histad(:, 1)<=Xself(a+1)+lambda/2)
    if (length(counts)==0)
        counts=0;
    else
        for c=1:length(counts')
            b=counts(c);
forsta=find(sortedMatrix(:, 4)==histad(b, 2), 1, 'first');
sista=find(sortedMatrix(:, 4)==histad(b, 2), 1, 'last');
            v(c, a)=(((sortedMatrix(sista, 1)-
sortedMatrix(forsta, 1))^2+(sortedMatrix(sista, 2)-
sortedMatrix(forsta, 2))^2)^0.5/(sortedMatrix(sista, 3)-
sortedMatrix(forsta, 3))/str2num(get(handles.edit24, 'String'))
*str2num(get(handles.edit25, 'String'))*str2num(get(handles.framerate, 'String')));
            vLat(c, a)=(abs((sortedMatrix(sista, 2)-
sortedMatrix(forsta, 2))/(sortedMatrix(sista, 3)-
sortedMatrix(forsta, 3)))/str2num(get(handles.edit24, 'String'))
)*str2num(get(handles.edit25, 'String'))*str2num(get(handles.framerate, 'String')));
            if (vLat(c, a)<0)
                1
            end
        end
        Nself(a)=length(counts);
    end
end
[N, X]=hist(histad(:, 1), X)
plot(X, N, ':x')

assignin('base', 'v', v);

```

```
assignin('base','vLat',vLat);
for a=1:length(v(1,:))
    vMean(a)=mean(v((v(:,a)~=0),a));
    vStand(a)=std(v((v(:,a)~=0),a));
    vLatMean(a)=mean(vLat((vLat(:,a)~=0),a));
    vLatStand(a)=std(vLat((vLat(:,a)~=0),a));
end
vStand(isnan(vStand))=0;
vMean(isnan(vMean))=0;
vLatStand(isnan(vLatStand))=0;
vLatMean(isnan(vLatMean))=0;

assignin('base','vMean',vMean);
assignin('base','vStand',vStand);
assignin('base','vLatMean',vLatMean);
assignin('base','vLatStand',vLatStand);
hold on
Ylimit=get(gca,'YLim');
set(gca,'YLim',[0 (Ylimit(2)+2)]);
function edit11_Callback(hObject, eventdata, handles)
function edit11_CreateFcn(hObject, eventdata, handles)
if ispc && isequal(get(hObject,'BackgroundColor'),
get(0,'defaultUiControlBackgroundColor'))
    set(hObject,'BackgroundColor','white');
end

% --- Executes on button press in pushbutton10.
function pushbutton10_Callback(hObject, eventdata, handles)
% hObject    handle to pushbutton10 (see GCBO)
% eventdata  reserved - to be defined in a future version of
MATLAB
% handles    structure with handles and user data (see
GUIDATA)
% --- Executes on button press in pushbutton3.
if isempty(get(handles.listbox4,'String'))
    itWasEmpty=1;
end
[input_file,pathname] = uigetfile( ...
    {'*.tif', 'Tiff (*.Tif)'; ...
    ' *.*', 'All Files (*.*)'}, ...
    'Select files', ...
    'MultiSelect', 'on');

%if file selection is cancelled, pathname should be zero
%and nothing should happen
if pathname == 0
    return
end

%gets the current data file names inside the listbox
```

Appendix 5: MATLAB and Java code

```
inputFileNames = get(handles.listbox4, 'String');

%if they only select one file, then the data will not be a
cell
%if more than one file selected at once,
%then the data is stored inside a cell
if iscell(input_file) == 0
%   checks to see if the file is already in the list
    if isempty(find(ismember(inputFileNames,
fullfile(pathname, input_file))==1, 1))
        %add the most recent data file selected to the cell
        containing
            %all the data file names
            %stores full file path into inputFileNames
            inputFileNames{end+1} =
fullfile(pathname, input_file);
        else
            place=find(ismember(inputFileNames,
fullfile(pathname, input_file))==1);
            eval(['warndlg('' fullfile(input_file) ' finns redan
i listan! På plats: ' num2str(place) '')']);
        end
    end

%else, data will be in cell format
else
    exists=[];
    for n = 1:length(input_file)
        %   checks to see if the file is already in the
list
            temp=find(ismember(inputFileNames,
fullfile(pathname, input_file{n}))==1, 1);
            if isempty(temp)
                %notice the use of {}, because we are dealing
with a cell here!
                inputFileNames{end+1} =
fullfile(pathname, input_file{n});
            else
                if isempty(exists)
                    eval(['exists=[]' num2str(temp) '''])
                else
                    eval(['exists=[exists ', ' ', ' '
num2str(temp) '''])
                end
            end
        end
    end
    if isempty(exists)==0
        eval(['warndlg(''Hittade dublett(er) i listan på
följande platser: ' exists '')']);
    end
end
```

```
%updates the gui to display all filenames in the listbox
set(handles.listbox4, 'String', inputFileNames);

%make sure first file is always selected so it doesn't go out
of range
%the GUI will break if this value is out of range
set(handles.listbox4, 'Value', 1);
guidata(hObject, handles);

% --- Executes on button press in pushbutton11.
function pushbutton11_Callback(hObject, eventdata, handles)
% hObject      handle to pushbutton11 (see GCBO)
% eventdata    reserved - to be defined in a future version of
MATLAB
% handles      structure with handles and user data (see
GUIDATA)
inputFileNames = get(handles.listbox4, 'String');

%get the values for the selected file names
option = get(handles.listbox3, 'Value');
%is there is nothing to delete, nothing happens
if (isempty(option) == 1 || option(1) == 0 ||
isempty(inputFileNames))
    return
end

%erases the contents of highlighted item in data array
inputFileNames(option) = [];

%updates the gui, erasing the selected item from the listbox
set(handles.listbox4, 'String', inputFileNames);

%moves the highlighted item to an appropriate value or else
will get error
if option(end) > length(inputFileNames)
    set(handles.listbox4, 'Value', length(inputFileNames));
end

% Update handles structure
guidata(hObject, handles);
% --- Executes on selection change in listbox4.
function listbox4_Callback(hObject, eventdata, handles)
function listbox4_CreateFcn(hObject, eventdata, handles)
if ispc && isequal(get(hObject, 'BackgroundColor'),
get(0, 'defaultUicontrolBackgroundColor'))
    set(hObject, 'BackgroundColor', 'white');
end
function checkbox5_Callback(hObject, eventdata, handles)
function edit12_Callback(hObject, eventdata, handles)
```

```
function edit12_CreateFcn(hObject, eventdata, handles)
if ispc && isequal(get(hObject,'BackgroundColor'),
get(0,'defaultUicontrolBackgroundColor'))
    set(hObject,'BackgroundColor','white');
end
function edit13_Callback(hObject, eventdata, handles)
function edit13_CreateFcn(hObject, eventdata, handles)
if ispc && isequal(get(hObject,'BackgroundColor'),
get(0,'defaultUicontrolBackgroundColor'))
    set(hObject,'BackgroundColor','white');
end
% --- Executes on button press in checkbox6.
function checkbox6_Callback(hObject, eventdata, handles)
global bgImage
global imageNames
% Hint: get(hObject,'Value') returns toggle state of
checkbox6
if
(get(hObject,'Value')&&isempty((get(handles.listbox3,'String'
)))==0)

bgImage=medianBG(imageNames,str2num(get(handles.edit14,'Strin
g')),str2num(get(handles.edit16,'String')),handles);
end

function edit14_Callback(hObject, eventdata, handles)
function edit14_CreateFcn(hObject, eventdata, handles)
if ispc && isequal(get(hObject,'BackgroundColor'),
get(0,'defaultUicontrolBackgroundColor'))
    set(hObject,'BackgroundColor','white');
end
function edit16_Callback(hObject, eventdata, handles)
function edit16_CreateFcn(hObject, eventdata, handles)
if ispc && isequal(get(hObject,'BackgroundColor'),
get(0,'defaultUicontrolBackgroundColor'))
    set(hObject,'BackgroundColor','white');
end
function checkbox7_Callback(hObject, eventdata, handles)
function edit17_Callback(hObject, eventdata, handles)
function edit17_CreateFcn(hObject, eventdata, handles)
if ispc && isequal(get(hObject,'BackgroundColor'),
get(0,'defaultUicontrolBackgroundColor'))
    set(hObject,'BackgroundColor','white');
end
% --- Executes on button press in pushbutton13.
function pushbutton13_Callback(hObject, eventdata, handles)
global sorted imageNames imwidth imheight
[sort1 sort2]=sort(sorted(:,3));
timeSorted=sorted(sort2,:);
```

Appendix 5: MATLAB and Java code

```
% börjar leta i ruta 2 efter partiklar som även fanns i ruta
ett, sen
% plota och upprepa
figure('Tag', 'plotFigure');
set(gca, 'Position', [0 0 1 1], 'XTick', [], 'YTick', [], 'XLim', [0
imwidth], 'YLim', [0 imheight], 'Color', [0 0
0], 'YDir', 'reverse')
set(gcf, 'position', [200 200 imwidth imheight])
WM='overwrite';
frames=(str2double(get(handles.edit10, 'String'))-
str2double(get(handles.edit9, 'String'))+1);
pplot=zeros(imheight, imwidth, 3, frames);
emptyWrite=[];
for
i=str2double(get(handles.edit9, 'String')):str2double(get(hand
les.edit10, 'String'))
    b1=find(timeSorted(:,3)==i-1,1);
    b2=find(timeSorted(:,3)==i-1,1, 'last');
    a1=find(timeSorted(:,3)==i);
    a2=find(timeSorted(:,3)==i,1, 'last');
    writeCheck=0;
    nbrOfPrtcls=timeSorted(end,4);
    loopnr=i-str2double(get(handles.edit9, 'String'))+1;

    if (isempty(a1)==0) && (isempty(b1)==0)
        for a=a1:a2
            % finding particle with same id in last frame
            row=(find(timeSorted(a,4)==timeSorted(b1:b2,4),
1)+b1-1);
            if (isempty(row)==0)
                writeCheck=1;
                line([timeSorted(row,1)
timeSorted(a,1)], [timeSorted(row,2)
timeSorted(a,2)], 'Color', [1-
(timeSorted(a,4))/(2*nbrOfPrtcls), (timeSorted(a,4))/nbrOfPrtc
ls, 1-(timeSorted(a,4))/nbrOfPrtcls], 'LineWidth', 3)
                drawnow
                hold on
            end
            row=[];
        end

        b1=a1;
        b2=a2;
        a1=a2+1;
    end
% set(gca, 'DataAspectRatio', [1 1 1])
temp=getframe;
pplot(:, :, :, loopnr)=temp.cdata;
```

Appendix 5: MATLAB and Java code

```
% check if writing has occurred (this is needed in plot/img
overlay below)
if (writeCheck==0)
    emptyWrite(end+1)=i;

end
end
WM='overwrite';
eval(['outputFileName='''          get(handles.edit21, 'String')
'.tif''']);
    toClose = findobj(get(0, 'Children'), 'flat', 'Tag',
'plotFigure');
    delete(toClose)
for
i=str2double(get(handles.edit9, 'String')):str2double(get(hand
les.edit10, 'String'))
    bild=double(imread(imageNames{1}, i));
    BG=uint8(round(255*( (bild-
min(min(bild)) / (max(max(bild)) -min(min(bild)) ) ) ) );
    BG=cat(3, BG, BG, BG);
    loopnr=i-str2double(get(handles.edit9, 'String'))+1;
    pxls=length(pplot(:, 1, 1, 1))*length(pplot(1, :, 1, 1));

BG((pplot(:, :, 1, loopnr)>0))=uint8(pplot(find(pplot(:, :, 1, loop
nr)>0)+3*pxls*(loopnr-1)));

BG(find(pplot(:, :, 2, loopnr)>0)+pxls)=uint8(pplot(find(pplot(:
, :, 2, loopnr)>0)+pxls+3*pxls*(loopnr-1)));

BG(find(pplot(:, :, 3, loopnr)>0)+2*pxls)=uint8(pplot(find(pplot
(:, :, 3, loopnr)>0)+2*pxls+3*pxls*(loopnr-1)));

imwrite(BG, outputFileName, 'tif', 'WriteMode', WM, 'Compression',
'none');
    WM='append';

end

function edit18_Callback(hObject, eventdata, handles)
function edit18_CreateFcn(hObject, eventdata, handles)
if ispc && isequal(get(hObject, 'BackgroundColor'),
get(0, 'defaultUiControlBackgroundColor'))
    set(hObject, 'BackgroundColor', 'white');
end
function edit19_Callback(hObject, eventdata, handles)
function edit19_CreateFcn(hObject, eventdata, handles)
if ispc && isequal(get(hObject, 'BackgroundColor'),
get(0, 'defaultUiControlBackgroundColor'))
    set(hObject, 'BackgroundColor', 'white');
end
function edit20_Callback(hObject, eventdata, handles)
```

```
function edit20_CreateFcn(hObject, eventdata, handles)
if ispc && isequal(get(hObject,'BackgroundColor'),
get(0,'defaultUicontrolBackgroundColor'))
    set(hObject,'BackgroundColor','white');
end
function edit21_Callback(hObject, eventdata, handles)
function edit21_CreateFcn(hObject, eventdata, handles)
if ispc && isequal(get(hObject,'BackgroundColor'),
get(0,'defaultUicontrolBackgroundColor'))
    set(hObject,'BackgroundColor','white');
end
% --- Executes on button press in checkbox8.
function checkbox8_Callback(hObject, eventdata, handles)
function edit22_Callback(hObject, eventdata, handles)
function edit22_CreateFcn(hObject, eventdata, handles)
if ispc && isequal(get(hObject,'BackgroundColor'),
get(0,'defaultUicontrolBackgroundColor'))
    set(hObject,'BackgroundColor','white');
end
function edit23_Callback(hObject, eventdata, handles)
function edit23_CreateFcn(hObject, eventdata, handles)
if ispc && isequal(get(hObject,'BackgroundColor'),
get(0,'defaultUicontrolBackgroundColor'))
    set(hObject,'BackgroundColor','white');
end
function edit24_Callback(hObject, eventdata, handles)

function edit24_CreateFcn(hObject, eventdata, handles)
if ispc && isequal(get(hObject,'BackgroundColor'),
get(0,'defaultUicontrolBackgroundColor'))
    set(hObject,'BackgroundColor','white');
end
function edit25_Callback(hObject, eventdata, handles)

function edit25_CreateFcn(hObject, eventdata, handles)
if ispc && isequal(get(hObject,'BackgroundColor'),
get(0,'defaultUicontrolBackgroundColor'))
    set(hObject,'BackgroundColor','white');
end

function pushbutton14_Callback(hObject, eventdata, handles)
global histad
histad=[];
set(hObject,'Visible','off')
function checkbox9_Callback(hObject, eventdata, handles)

function framerate_Callback(hObject, eventdata, handles)

function framerate_CreateFcn(hObject, eventdata, handles)
if ispc && isequal(get(hObject,'BackgroundColor'),
get(0,'defaultUicontrolBackgroundColor'))
```

```
set(hObject, 'BackgroundColor', 'white');  
end
```



```
        first=lst+1;
    end
    if(outOfBounds>0)
        x(end-outOfBounds+1:end,:)=[];
    end
    x(:,1)=x(:,1)+firstGap-1/2;
```

fixAndTrack.m

```
function [sorted handles] =
fixAndTrack(fileName, frames, threshold, bpLow, bpHigh, stepSize,
handles, listNumber)
global bgImage
cnt=zeros(1,5);
rowNbr=1;
fileName=fileName{listNumber,1};
a=double(imread(fileName,1));
storlek=size(a); % changed

% make sure stepsize is even..
if(mod(stepSize,2)==0)
    stepSize=stepSize+1;
end
% kolla om max frame är satt till 0, och sätt den isf till
max
if frames(2)==0
    info = imfinfo(fileName);
    frames(2)=numel(info);
end
% find positions of particles -> cnt matrix.
for i=frames(1):frames(2)

    eval(['set(handles.edit11, 'String', ['' num2str(i-
frames(1)+1) ' of ' num2str(frames(2)-frames(1)+1) ', movie '
num2str(listNumber) ''])'])
    drawnow
    if(get(handles.checkbox6, 'Value')==0)
        bild=double(imread(fileName,i)); %changed

a=[zeros(stepSize,2*stepSize+storlek(2));zeros(storlek(1),ste
pSize) bild
zeros(storlek(1),stepSize);zeros(stepSize,2*stepSize+storlek(
2))]; %changed
    else
        bild=double(imread(fileName,i));
        bild=bild-bgImage;
        bild(bild<0)=0;

a=[zeros(stepSize,2*stepSize+storlek(2));zeros(storlek(1),ste
pSize) bild
zeros(storlek(1),stepSize);zeros(stepSize,2*stepSize+storlek(
2))]; %changed
    end

    b = bpass(a,bpLow,bpHigh+1); % could add a 3rd parameter
here, sz if data is noise, sz=~diameter+1
    pk = pkfnd(b,threshold,bpHigh+1); % th, could add sz here
aswell
```

```
if (isempty(pk) == 0)

    temp = cntrd(b, pk, stepSize); %
    image, positions, stepsize
    sze = size(temp);
    cnt(rowNbr:rowNbr+sze(1)-1, 1:4) = temp;
    cnt(rowNbr:rowNbr+sze(1)-1, 5) = i;
    rowNbr = rowNbr + sze(1);
end
end
% pick out particle position and time
fix = (cnt(:, 1:2));
fix(:, 3) = cnt(:, 5);
% remove sidebars
fix(:, 1:2) = fix(:, 1:2) - stepSize;
% and now... track particles!
sorted = track(fix, stepSize); % matrix, stepSize

end
```

A5.2 Java program for designing the array

```
import se.lth.cs.pt.io.*;
import java.io.*;
class Array {
    public static void main(String[] args) {
        // System.out.println("Allt ska anges i mikrometer");
        double gapSize = 25; //Keyboard.nextDouble("ange gapsize: ");
        double postSize = 20; //Keyboard.nextDouble("ange postsize: ");
        double minCriticalSize = 8; //Keyboard.nextDouble("ange minsta kritiska diameter: ");
        double maxCriticalSize = 20; //Keyboard.nextDouble("ange största kritiska diameter: ");
        double stepSize = 1; //Keyboard.nextDouble("ange ökningen: ");
        double L[] = new double[(int) Math.round((maxCriticalSize - minCriticalSize) / stepSize + 0.5)];
        double N[] = new double[(int) Math.round((maxCriticalSize - minCriticalSize) / stepSize + 0.5)];
    }
}
```

```
double smallestFeature = 0.2; //Keyboard.nextDouble("ange
manufacturing grid: ");
double bumpDistance = 5*(gapSize+postSize);
//Keyboard.nextDouble("ange bumpdistance per region: ");
String name = ("test.txt"); //Keyboard.next("Ange filnamn: ");
*/
double verticesOfCircle=40;
double width = N.length*bumpDistance+450;
//Keyboard.nextDouble("ange ungefärlig bredd: ");
System.out.println(width);

// Räkna ut perioden
N=calcPeriod(minCriticalSize,maxCriticalSize,stepSize,gapSize
,N);
// System.out.println("N: " + N[0] + ", " + N[1]);

//räkna ut korrigerad N, med hänsyn till manufacturer grid
double[] N_fix = correctPeriod(N,gapSize,postSize,smallestFeature);
// System.out.println("N_fix: " + N_fix[0] + ", " + N_fix[1]);

//räkna ut L för de olika regionerna med de nya periodvärdena
L=calcLength(minCriticalSize,maxCriticalSize,stepSize,bumpD
istance,L,N_fix,gapSize,postSize);
// System.out.println("L: " + L[0] + ", " + L[1]);

double[] L_fix = correctLength(L,gapSize,postSize,N_fix);
// System.out.println("L_fix: " + L_fix[0] + ", " + L_fix[1]);

// konstruera enhetscell samt placera ut denna i
koordinatssystemet
String coordinates = postCoordinates(postSize,gapSize,N_fix,L_fix,width,verticesOf
Circle);

//skriv filen till ett textdokument
writeFile(coordinates,postSize, name);
}
```

```
static void writeFile(String coordinates, double postSize, String name)
{
    try{
        Writer output = null;
        String pre = ("(DATE: 22 Feb 1983);\r\n(FABCELL:
NONE);\r\n(L-Edit Layer Poly = CIF Layer CPG);\r\n(L-Edit
Layer Active = CIF Layer CAA);\r\n(L-Edit Layer Metall =
CIF Layer CMF);\r\n(L-Edit Layer Metall-Tight = CIF Layer
CMF);\r\n(L-Edit Layer Metal2 = CIF Layer CMS);\r\n(L-Edit
Layer Metal2-Tight = CIF Layer CMS);\r\n(L-Edit Layer
Metal3 = CIF Layer CMT);\r\n(L-Edit Layer N Well = CIF
Layer CWN);\r\n(L-Edit Layer Cap Well = CIF Layer
CWC);\r\n(L-Edit Layer N Select = CIF Layer CSN);\r\n(L-Edit
Layer P Select = CIF Layer CSP);\r\n(L-Edit Layer Poly
Contact = CIF Layer CCP);\r\n(L-Edit Layer Active Contact =
CIF Layer CCA);\r\n(L-Edit Layer Vial = CIF Layer
CVA);\r\n(L-Edit Layer Via2 = CIF Layer CVS);\r\n(L-Edit
Layer Overglass = CIF Layer COG);\r\n(L-Edit Layer Pad
Comment = CIF Layer XP);\r\n(L-Edit Layer Icon/Outline =
CIF Layer CX);\r\n(SCALING: 1 CIF Unit = 1/2000
Microns);\r\nDS 1 2 40;\r\n9 Cell0;\r\nL CAA;");

        String post = ("\r\nDF;\r\nE");
        String text = (pre + coordinates + post);
        File file = new File("Array.cif");
        output = new BufferedWriter(new FileWriter(file));
        output.write(text);
        output.close();
        System.out.println("Your file has been written");
    } catch (Exception e) {
        System.out.println("Fel!");
    }
}

static double[] correctPeriod(double[] N, double gapSize, double
postSize, double smallestFeature) {
    double[] N_fix = new double[N.length];
    for (int i=0;i<N.length;i++) {
```

```

        int n = (int) Math.round((gapSize +
postSize)/(N[i]*smallestFeature));
        if (n==0) {
            n=1;
            System.out.println("fail..");
        }
        N_fix[i]=((gapSize+postSize)/(smallestFeature*n));
        System.out.println("N_fix[" + i + "] = " + N_fix[i]);
        System.out.println("Dc[" + i + "] : " +
1.4*gapSize/(Math.pow(N_fix[i],0.48)) + "\r\n\r\n");
    }
    return N_fix;
}
// fix correct length to make sure that there is a whole gap in the end
to the adjacent section
static double[] correctLength(double[] L, double gapSize, double
postSize,double[] N_fix) {
    /*
    double[] L_fix = new double[L.length];
    new double[L.length];
    for (int i=0;i<L.length;i++) {
        int n = (int) Math.round(L[i]/(gapSize+postSize));
        L_fix[i] = n*(gapSize+postSize);
        // System.out.println(L_fix[i]);
    }
    for (int i=0;i<L.length;i++){
        L_fix[i] = Math.round((N_fix[i]-0.5))*(gapSize*postSize));
        System.out.println(L_fix[i]);
    }
    */
    double[] L_fix = L;
    for (int i =0; i<L.length;i++) {
        System.out.println("L[" + i + "] = " + L[i]);
    }
    return L_fix;
}
static double[] calcPeriod(double minCriticalSize,double
maxCriticalSize,double stepSize, double gapSize, double[] N) {

```

```

        for (double d=minCriticalSize;d<=(maxCriticalSize);d+=stepSize) {
            int pos = (int)Math.round((d-minCriticalSize)/stepSize);
            N[pos]=Math.pow((1.4*gapSize/d),(1/0.48));
            System.out.println("CalcPeriod:" + N[pos]);
        }
    return N;
}

static double[] calcLength(double minCriticalSize,double
maxCriticalSize,double stepSize, double bumpDistance,
double[] L, double[] N_fix, double gapSize, double postSize) {
    for (int i = 0; i<N_fix.length;i++) {
        //avrundar till helt antal (posts+gaps)
        //sätt kvoten bumpdistance/(postSize+gapSize) till ett heltal.
        System.out.println("n= " + N_fix[i]);
        L[i]=(Math.round(N_fix[i]-
0.5)*(gapSize+postSize)*(bumpDistance/(gapSize+postSize)));
        System.out.println("hej:" + L[i]);
    }
    return L;
}

static String postCoordinates(double postSize, double gapSize,
double[] N_fix, double[] L_fix,double width,double
verticesOfCircle) {

    double lateralNbrOfPosts
=(width+5*(gapSize+postSize))/(gapSize+postSize);
    double[] vertNbrOfPosts = new double[L_fix.length];
    int sumVert=0;
    for (int i=0;i<L_fix.length;i++) {
        System.out.println("L:::" + L_fix[i]);
        vertNbrOfPosts[i] = L_fix[i]/(gapSize+postSize);
        System.out.println("v: " + vertNbrOfPosts[i]);
        sumVert += vertNbrOfPosts[i];
    }
    String textning = ("");

```

```
// används för att kompensera så att nya regioner hamnar rätt i
x-led (förskjuts pga att perioden ej är heltal)
double latCorrection=0;

int counter = 0;
System.out.println(sumVert + " " + lateralNbrOfPosts);
int[][] coordinates = new
int[sumVert*((int)Math.round(lateralNbrOfPosts))][2];

double delta=0;
double distance=0;
for (int l=0;l<L_fix.length;l++) { //L_fix.length ska in här!
    double period = N_fix[l];
    System.out.println(period);
    if (l > 0) {
        distance += L_fix[l-1];
        System.out.println("distance: " + distance);
    }
    // System.out.println("l: " + l);
    //skapa enhetscell
    int[][] unitCell = new int[(int)
Math.round(6+verticesOfCircle)][2];
    unitCell[0][0]=0;
    unitCell[0][1]=0;
    unitCell[1][0]=((int) Math.round((gapSize+postSize)*1000));
    unitCell[1][1]=0;
    unitCell[2][0]=((int)
Math.round(1000*((gapSize+postSize)+1/period*(gapSize+post
Size)))));
    unitCell[2][1]=-(int)
Math.round(1000*(gapSize+postSize));
    unitCell[3][0]=((int)
Math.round(1000*1/period*(gapSize+postSize)));
    unitCell[3][1]=-(int)
Math.round(1000*(gapSize+postSize));
    unitCell[4][0]=0;
    unitCell[4][1]=0;
    double angle;
    int temp=0;
```

```

double maxAngle=(3.0*Math.PI);
for
(angle=(Math.PI);Math.round(1000*angle)<=(Math.round(1000
*maxAngle)));angle=angle+2*Math.PI*(1/verticesOfCircle)) {
    int                loopNumber=((int)Math.round(((angle-
(Math.PI))/(2*Math.PI*(1/verticesOfCircle))));
    unitCell[5        +                loopNumber][0]=((int)
Math.round(1000*((gapSize+postSize)/(2*period)+(gapSize+po
stSize)/2+postSize/2*Math.cos(angle)));
    unitCell[5 + loopNumber][1]=((int) Math.round(1000*(-
(gapSize+postSize)/2+postSize/2*Math.sin(angle)));
    }

double vertX=0;
for (int vert=1;vert<=period;vert++) {
    //                System.out.println(vert);
    //Left edge adjustment
    textning=(textning + "\r\nP " + 2*((int)
Math.round(1000*(-3*(gapSize+postSize)-
latCorrection*1000)) + "," + 2*((int) Math.round(-
(gapSize+postSize)*vert*1000-distance*1000)) + " " + 2*((int)
(Math.round(((gapSize+postSize)*vert/period*1000)-
latCorrection*1000-
2*1000*(gapSize+postSize)+gapSize*19000/40))) + "," +
2*((int) Math.round(-(gapSize+postSize)*vert*1000-
distance*1000)) + " " + 2*((int)
(Math.round((gapSize+postSize)*(vert+1)/period*1000)-
latCorrection*1000-
2*1000*(gapSize+postSize)+gapSize*19000/40)) + "," +
2*((int) Math.round(-(gapSize+postSize)*(vert+1)*1000-
distance*1000)) + " " + 2*((int) Math.round(-
latCorrection*1000+1000*(-3*(gapSize+postSize)))) + "," +
2*((int) Math.round(-(gapSize+postSize)*(vert+1)*1000-
distance*1000)) + "\r\n " + 2*((int) Math.round(-
latCorrection*1000+1000*(-3*(gapSize+postSize)))) + "," +
2*((int) Math.round(-(gapSize+postSize)*vert*1000-
distance*1000)));

    for (int S=5;S<unitCell.length;S++) {

```

```

//plotning av vänster kantkorrigering

    textning = (textning + " " + 2*((int) Math.round(-
latCorrection*1000+unitCell[S][0]+2*(gapSize+postSize)*vert/
(2*period)*1000-1000*(2*gapSize+3*postSize)-
1000*gapSize*Math.sqrt((vert+1)/period))) + "," + 2*((int)
Math.round(unitCell[S][1]-(gapSize+postSize)*vert*1000-
distance*1000));
    if (S==unitCell.length-1) {
        textning=(textning + ";");
        break;
    }
    if ((S+1)%4==0) {
        textning=(textning + ("\r\n"));
    }
}
/*
                                textning = (textning + " " +
2*((int)                                (Math.round(-
latCorrection*1000+unitCell[uC][0]+(gapSize+postSize)*vert/p
eriod*1000+(gapSize+postSize)*lat*1000+(gapSize+postSize)*
(Math.round((width/(gapSize+postSize)-3))*1000)-
gapSize*1000+1000*gapSize*Math.sqrt(2-(vert+1)/period)))) +
", " + 2*((int)                                Math.round((unitCell[uC][1]-
(gapSize+postSize)*vert*1000-distance*1000)));
*/

//                                System.out.println("-=[COUNTDOWN]=-
Regions left: " + (L_fix.length-1) + " Rows left in this region: "
+ (int)(period-vert));

int latX=0;
lateralNbrOfPosts=2;
for (int lat=0;lat<=lateralNbrOfPosts;lat++) {
    textning=(textning + "\r\nP");
    //                                System.out.println("lat: " + lat);
    for (int uC=0;uC<unitCell.length;uC++) {

```

```

        if (lat==0) {
            if (uC==0) {
                textning = (textning + " " +
2*((int)
                    (Math.round(-latCorrection*1000+(unitCell[0][0]-
2*1000*(gapSize+postSize)+(gapSize+postSize)*lat*1000)+(gapSize+
postSize)*vert/period*1000+1000*gapSize*19/40)) + "," +2*((int)
Math.round((unitCell[0][1]-(gapSize+postSize)*vert*1000-
distance*1000)));

                textning = (textning + " " +
2*((int)
                    (Math.round(-latCorrection*1000+unitCell[1][0]-
2*1000*(gapSize+postSize)+(gapSize+postSize)*lat*1000)+(gapSize+
postSize)*vert/period*1000)) + "," + 2*((int)
Math.round((unitCell[1][1]-(gapSize+postSize)*vert*1000-
distance*1000)));

                textning = (textning + " " +
2*((int)
                    (-latCorrection*1000+Math.round(unitCell[2][0]-
2*1000*(gapSize+postSize)+(gapSize+postSize)*lat*1000)+(gapSize+
postSize)*vert/period*1000)) + "," + 2*((int)
Math.round((unitCell[2][1]-(gapSize+postSize)*vert*1000-
distance*1000)));

                textning = (textning + " " +
2*((int)
                    (-latCorrection*1000+Math.round(unitCell[3][0]-
2*1000*(gapSize+postSize)+(gapSize+postSize)*lat*1000)+(gapSize+
postSize)*vert/period*1000+1000*gapSize*19/40)) + "," + 2*((int)
Math.round((unitCell[3][1]-(gapSize+postSize)*vert*1000-
distance*1000)));

                textning = (textning + "\r\n " +
2*((int)
                    (Math.round(-latCorrection*1000+(unitCell[0][0]-
2*1000*(gapSize+postSize)+(gapSize+postSize)*lat*1000)+(gapSize+
postSize)*vert/period*1000+1000*gapSize*19/40)) + "," + 2*((int)
Math.round((unitCell[4][1]-(gapSize+postSize)*vert*1000-
distance*1000)));

                uC=5;

            }

```

```

                textning = (textning + " " +
2*((int)          (Math.round(-latCorrection*1000+unitCell[uC][0]-
2*1000*(gapSize+postSize)+(gapSize+postSize)*lat*1000+(gapSize+
postSize)*vert/period*1000))) + "," + 2*((int)
Math.round((unitCell[uC][1]-(gapSize+postSize)*vert*1000-
distance*1000)));
                //
                System.out.println(lat=0);

                } else if (lat==lateralNbrOfPosts)
{
                if (uC<5) {
                        if (uC==1) {
                                textning =
(textning + " " + 2*((int) Math.round(-
latCorrection*1000+(gapSize+postSize)*(lat+2)*1000+(gapSize+post
Size)*(Math.round((width/(gapSize+postSize)-3))*1000))) + "," +
2*((int) Math.round(-(gapSize+postSize)*vert*1000-distance*1000)));
                                textning =
(textning + " " + 2*((int) Math.round(-
latCorrection*1000+(gapSize+postSize)*(lat+2)*1000+(gapSize+post
Size)*(Math.round((width/(gapSize+postSize)-3))*1000))) + "," +
2*((int) Math.round(-(gapSize+postSize)*vert*1000-distance*1000-
(gapSize+postSize)*1000)));
                                uC=2;
                        } else {
                                textning = (textning + " " +
2*((int)          (Math.round(-
latCorrection*1000+unitCell[uC][0]+(gapSize+postSize)*vert/period*
1000+(gapSize+postSize)*lat*1000+(gapSize+postSize)*(Math.round(
(width/(gapSize+postSize)-3))*1000))) + "," + 2*((int)
Math.round((unitCell[uC][1]-(gapSize+postSize)*vert*1000-
distance*1000)));
                                }
                        } else {
                                //      plottning      av      höger
kantkorrigering

```

```

                textning = (textning + " " +
2*((int)                (Math.round(-
latCorrection*1000+unitCell[uC][0]+(gapSize+postSize)*vert/period*
1000+(gapSize+postSize)*lat*1000+(gapSize+postSize)*(Math.round(
(width/(gapSize+postSize)-3))*1000)-
gapSize*1000+1000*gapSize*Math.sqrt(2-(vert)/period)))) + "," +
2*((int)  Math.round((unitCell[uC][1]-(gapSize+postSize)*vert*1000-
distance*1000)));

//
System.out.println("right gap: " + gapSize*Math.sqrt(2-
(vert+1)/period));
    }

    } else {
        textning = (textning + " " +
2*((int)                (Math.round(-
latCorrection*1000+unitCell[uC][0]+(gapSize+postSize)*lat*1000+(g
apSize+postSize)*vert/period*1000))) + "," + 2*((int)
Math.round((unitCell[uC][1]-(gapSize+postSize)*vert*1000-
distance*1000)));
    }
    if (uC==unitCell.length-1) {
        textning=(textning + ";");
        break;
    }
    if ((uC+1)%4==0) {
        textning = (textning + "\r\n" );
    }
}
}
/*
if (periodX++>=period) {
    periodX-=period; //periodX används om man vill rita ut
flera perioder efter varandra och perioden i N_fix ej är ett
heltal(alltid), nu vill jag dock rita så lite som möjligt...
}
*/

```

```
        //                               System.out.println("l: " + l + ",
period: " + period + ", vert: " + vert);

        if (period<vert+1){
            //                               System.out.println("l'a'gg till: "
+ (gapSize+postSize)*(period-vert-1));
            // System.out.println((gapSize+postSize)/period )
            System.out.println("justera region nr " + (l+1) + " at
v'a'nster med: " + (gapSize+postSize)*(period-vert)/(period) + "
(vid array)\r\n");
            // 5 är för antalet peroder
            latCorrection+=(gapSize+postSize)*(period-
vert)/(period)*5;
            // System.out.println(latCorrection);
        }
    }
}

//plotta ut andra layers för att enkelt kunna
fixa till kanter + posts
System.out.println("create an array with this amount of x
elements: " + (int)Math.round((width/(gapSize+postSize)-2)));

return textning;
}
}
```

Appendix 6. Laboratory Setup

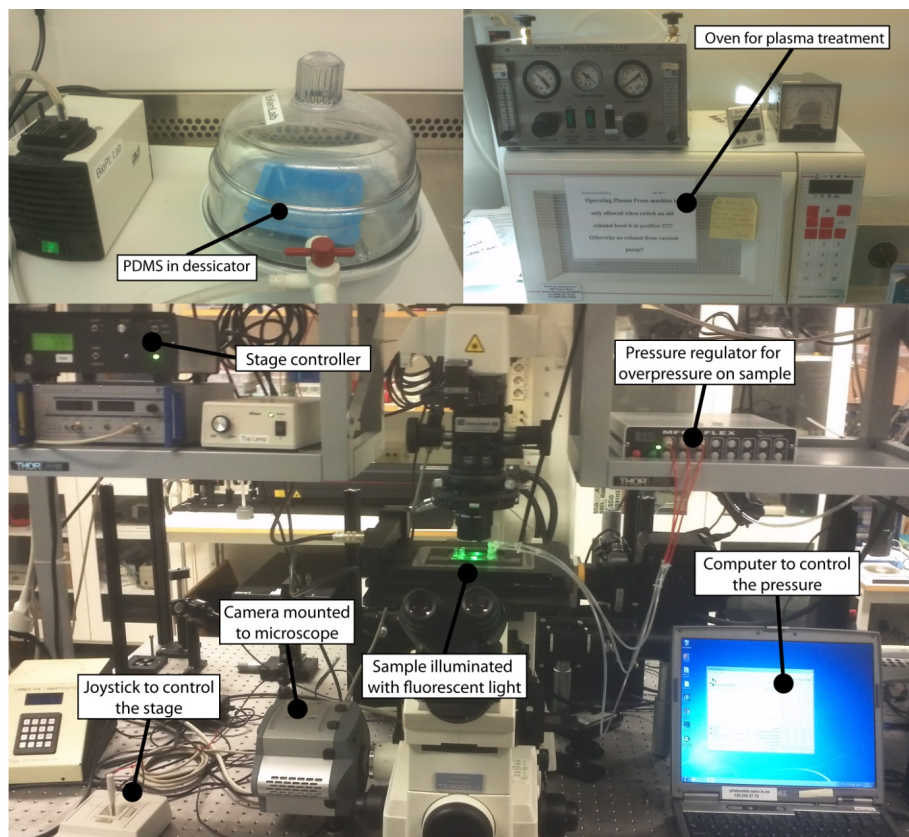


Figure 51. Image showing the lab where much of the device fabrication and experimental measurements took place.

Cite this: *Lab Chip*, 2011, **11**, 1326

www.rsc.org/loc

PAPER

Separation of parasites from human blood using deterministic lateral displacement†

Stefan H. Holm,^{‡a} Jason P. Beech,^{‡a} Michael P. Barrett^b and Jonas O. Tegenfeldt^{*ac}

Received 3rd November 2010, Accepted 20th January 2011

DOI: 10.1039/c0lc00560f

We present the use of a simple microfluidic technique to separate living parasites from human blood. Parasitic trypanosomatids cause a range of human and animal diseases. African trypanosomes, responsible for human African trypanosomiasis (sleeping sickness), live free in the blood and other tissue fluids. Diagnosis relies on detection and due to their often low numbers against an overwhelming background of predominantly red blood cells it is crucial to separate the parasites from the blood. By modifying the method of deterministic lateral displacement, confining parasites and red blood cells in channels of optimized depth which accentuates morphological differences, we were able to achieve separation thus offering a potential route to diagnostics.

1. Introduction

Human African trypanosomiasis is caused by parasitic protozoa of the *Trypanosoma brucei* subgroup.¹ The parasites, transmitted by tsetse flies, proliferate in the haemolymphatic system of infected patients in stage 1 of the disease. In stage 2 they invade the central nervous system where they cause increasing neurological dysfunction, including the changes to sleep–wake patterns that lend the disease its common name of sleeping sickness. Two subspecies of *T. brucei* are responsible for human disease, both forms of which are fatal if left untreated. *T. brucei rhodesiense* causes an acute form where uncontrolled parasite proliferation leads to death within weeks of an infection. *T. brucei gambiense* causes a chronic infection where parasite proliferation is limited and several years elapse between infection and development of stage 2 disease, which can last for a year or more prior to death. Treatment of stage 1 disease is easier than for stage 2 and different drugs are used.² At stage 2, treatment depends either on melarsoprol, a highly toxic organic arsenical that kills 5% of those taking the drug, or eflornithine, which is given for two weeks by intravenous infusion. Eflornithine costs are high enough to limit use of the drug. Early stage treatment involves the use of either suramin or pentamidine depending on the type of parasite. Although both of these drugs have non-negligible

side effects, early diagnosis and treatment are very much preferred over late stage treatment. However, diagnosis of human African trypanosomiasis is challenging and the standard parasitological techniques currently used are estimated to give false negatives in 20–30% of cases.³ Large scale screening for *gambiense* disease (which is responsible for >90% of all current cases) involves use of the serologically based Card Agglutination Test for Trypanosomiasis (CATT). The test, however, depends upon particular surface antigens found on most, but not all, *gambiense* parasites which limit its sensitivity and selectivity.⁴ The gold standard in diagnosis depends upon microscopical detection of parasites in blood. This is very difficult in *gambiense* disease where the parasitaemia is frequently below 1000 cells per mL of blood.³ Given the low abundance of parasites in blood, methods have been developed to concentrate the trypanosomes prior to microscopy, each with its limitations, as reviewed by Chappuis *et al.*³ Microhematocrit Centrifugation Technique (MHCT) involves separating the buffy coat containing the white blood cells (WBC) and trypanosomes from the denser red blood cells (RBCs). Quantitative Buffy Coat (QBC) is a method derived from this approach that also uses high-speed centrifugation together with fluorescence detection. Both of these techniques have a detection limit of ~500 trypanosomes per mL of blood.

Currently the best trypanosome separation technique is the mini-Anion-Exchange Centrifugation Technique (mAECT) which has been reported of having a detection limit of 100 trypanosomes per mL of blood. This method exploits the negative surface charge of RBCs to remove them from a blood sample while neutrally charged trypanosomes pass through the column and can then be concentrated by centrifugation. A large field-study in 2004 concluded the sensitivity of mAECT to be 75.3%, cost per test almost €3 and time per test half an hour.⁵

An alternate method to these separation techniques is to selectively lyse the RBCs.⁶ This method has been estimated to

^aDivision of Solid State Physics, nmC@LU, Lund University, PO Box 118, S-221 00 Lund, Sweden. E-mail: jonas.tegenfeldt@ftf.lth.se; Fax: +46 (0)46 222 3637; Tel: +46 (0)46 222 8063

^bWelcome Trust Centre for Medical Parasitology, Institute of Infection, Immunity and Inflammation, College of Medical, Veterinary and Life Sciences, University of Glasgow, UK

^cDepartment of Physics, University of Gothenburg, Gothenburg, Sweden

† Electronic supplementary information (ESI) available. See DOI: 10.1039/c0lc00560f

‡ Authors contributed equally.

also have a detection limit of ~ 500 trypanosomes per mL of blood but has been difficult to implement and has yet to receive widespread use.

All of the above methods are focused on increasing the trypanosome concentration by removing the background cells, predominantly RBCs. Given that 1 mL of blood might contain fewer than 1000 parasites, but on the order of 5×10^9 RBCs, 0.35×10^9 platelets and 7×10^6 WBCs the task is not trivial. However, advances in microfluidics, together with the fact that trypanosomes differ in multiple biophysical ways from blood cells including surface charge (as previously exploited in mAECT), size, shape and motility, offer the potential for new routes to separation of trypanosomes from blood cells. In the work reported here we are concerned with the problem of removing RBCs and present a proof of concept of a lab-on-a-chip microfluidic device that can readily separate trypanosomes from RBCs.

2. Deterministic lateral displacement

Deterministic Lateral Displacement (DLD) is a microfluidics-based particle separation technique, easy to implement in cheap disposable plastic chips, that we believe is well suited for the task of removing parasites from blood cells in order to aid detection. The method of separation by DLD was first developed by Huang *et al.*⁷ and has been shown capable of separating RBCs, WBCs, platelets and plasma from whole blood⁸ as well as separating different types of WBCs based on their size.⁹ The mechanism of separation by DLD is based on the interaction of particles suspended in a fluid (in this case whole blood and parasites) with an ordered array of micrometre-sized posts that the fluid is forced to flow through under low Reynolds number conditions. The array of circular posts divides the fluid into many narrow streams, the widths of which correspond to the critical radii. Particles smaller than a critical size are able to follow one such stream through the array whereas larger particles are forced, through interactions with posts, to change streams many times, always in the same direction, becoming laterally displaced. For spherical particles the critical size, D_c , at which the transition between following the flow (zigzagging mode) and being displaced (displacement mode) occurs is given by eqn (1), which was empirically deduced by Davis.¹⁰

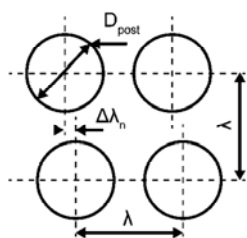


Fig. 1 A rhombic unit cell within the array of posts. In each of the 13 sections in the device every row is shifted a specific distance, Δ_n , with respect to the preceding row giving a range of critical diameters, $D_{c,n}$, as described by eqn (1). The gap (post–post separation) is given by $d = D_{\text{post}}$ and the periodicity is given by $N_n = 1/\Delta_n$.

$$D_{c,n} = 1.4dN_n^{-0.48} \quad (1)$$

The definitions of the array parameters are shown in Fig. 1. The amount of lateral displacement is a function of the array parameters and of the particles' effective sizes (and as we will show here, morphology).

A full description of the device, with all array parameters, can be found in the ESI, Section 1†. The device consists of 13 sections, each with a specific and increasing critical diameter, $D_{c,n}$ ($n = 1, 2, \dots, 13$), and where each section gives rise to a lateral displacement of $\sim 160 \mu\text{m}$ for particles with diameters larger than $D_{c,n}$. The total displacement for a particle with diameter D_{particle} is given by $x_{\text{particle}} \approx 160 \mu\text{m} \sum_{n=1}^{13} (D_{\text{particle}} > D_{c,n})$. The boolean term within the brackets equals 1 if true, else 0. A spherical particle that has a smaller diameter than all of the critical diameters in the device should not be laterally displaced at all and is expected to emerge from the device at the position depicted by the first vertical grey line at $x = 0 \mu\text{m}$ in Fig. 2a. At the same time a particle which, for example, is larger than the third critical diameter but smaller than the fourth should emerge on the fourth vertical line at $x \approx 480 \mu\text{m}$. Particles are separated into 14 fractions with thresholds ranging from 3 to $9 \mu\text{m}$ in $0.5 \mu\text{m}$ steps, see Fig. 2b.

Spherical, fluorescent polystyrene microspheres with diameters in the range 3– $10 \mu\text{m}$ were used to calibrate our device. Fig. 2a shows how the microspheres are displaced by well-defined

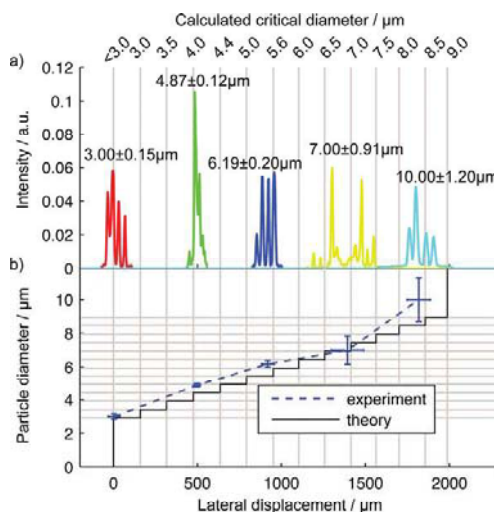


Fig. 2 Calibration of a deep separation device ($20 \mu\text{m}$) using fluorescent polystyrene microspheres. (a) The distribution of particles at the end of the separation device. The greater the diameter of the particles the further they are laterally displaced. The grey vertical lines show theoretical displacements for each discrete $0.5 \mu\text{m}$ step in critical diameter. The individual spikes correspond to the rows of posts in the actual device. (b) Comparison of the expected displacement of hard spheres according to theory (black line) with the experimentally measured displacements (blue dashed line). Vertical error bars show the standard deviation in the diameters of the microspheres according to the manufacturer, and horizontal error bars show the standard deviation in the lateral distribution measured at the end of the device.

amounts depending on their size, as described above. Fig. 2b shows a comparison of the measured displacement with the theory. Comparing microsphere sizes with their mean lateral displacements shows that the device parameters used result in a somewhat larger critical diameter than predicted by the theory. This applies to all of the microsphere sizes but is most notable for those of 10 μm diameter. For 10 μm microspheres the mean lateral displacement differs by almost 20% from the expected value. We believe this is due in part to the large diameter of the microspheres compared to the gap between posts (12 μm) and the large disturbance in the flow field this must cause, and in part due to a small imbalance in the exit flow in our present design. The volume flow through the channel that collects particles with maximum displacement (in this case 10 μm) was smaller than intended and particle trajectories tended to curve in toward the centre of the device where the volume flow was marginally larger leading to a decrease in total displacement for these particles.

In all work previously reported on DLD, devices have been fabricated much deeper than even the largest dimension of the particles, the aim being to attain high volume throughput. Particles are assumed to be either spherical or approximately spherical in these devices. We have previously shown that non-spherical particles can be oriented in DLD devices such that they present different dimensions to the device¹¹ thereby changing the effective size of the particle so that it approaches that of the selected dimension, for example the diameter of a disk shaped particle or the length of a long thin particle. The smallest dimensions of RBCs and parasites are very similar, the result, being that in a conventional deep DLD device their effective sizes are also very similar. This makes separation impossible or at best gives it very poor resolution. The method we present here, of tailoring device depth to the specific particle system, overcomes this problem and makes it possible to control the sensitivity of DLD to specific morphologies.

3. *Trypanosoma cyclops* as a model system

The African trypanosomes comprise a taxonomic group that includes those subspecies discussed above that are infectious to man, but also numerous other hemoflagellates infectious to other vertebrate species. Given the risks and regulatory constraints associated with working with *T. brucei* subspecies, we have confined our initial proof-of-concept studies to trypomastigotes (the flagellated parasite form found in the mammalian host) of the parasite *T. cyclops*, Fig. 3. This is a parasite of the macaque monkey, *Macaca*, found in Southeast Asia which also propagates as a trypomastigote in culture medium. The *T. cyclops* culture forms are similar but not identical to *T. brucei*. Cultured *T. cyclops* trypomastigotes are expected to be 33.5 μm long and 2.5 μm wide according to the literature,¹² while *T. brucei* trypomastigotes are described as 30 μm long and 1.5–3.5 μm wide.³ Initial size characterisation of our cultured *T. cyclops* was carried out by microscopical examination of 160 parasites resulting in a measured length of $30.6 \pm 4.7 \mu\text{m}$ and a broadest width of $2.6 \pm 0.4 \mu\text{m}$. No distinct subpopulations could be distinguished within the culture based on the size and there was very little correlation (correlation coefficient of 0.14) between the length and width of the parasites, see the ESI, Section 2†. The width of the *T. cyclops* is almost identical to the width of the RBCs which makes

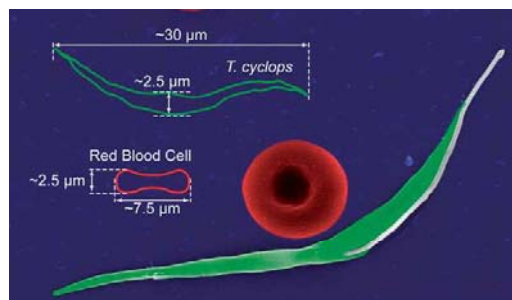


Fig. 3 A colour-enhanced scanning electron micrograph of an RBC (red) and a *T. cyclops* (green), both of which are representative of the most common size and shape. The dimensions of the two are also given.

separation in conventional DLD devices very difficult as described above.

It is possible that properties, such as surface charge and flagellum waveform, for example, differ between *T. cyclops* and *T. brucei*. However, the Deterministic Lateral Displacement technique that we employ depends primarily on cell shape and size. We thus believe that *T. cyclops* represent a legitimate surrogate for pathogenic *T. brucei* in demonstrating the separability of trypanosomes from RBCs in blood using DLD.

4. Materials and methods

To make a master for replica moulding SU-8 (MicroChem, Newton, MA, USA) was spin coated onto 3" silicon wafers at varying thicknesses and patterned using UV light in a contact mask aligner (Karl Suss MJB3 and MJB4, Munich, Germany). A chrome mask was fabricated by Delta Mask (Delta Mask, Enschede, The Netherlands) with a design drawn in L-Edit 11.02 (Tanner Research, Monrovia, CA USA). Before casting, the master was given an anti-adhesion layer of 1H,1H,2H,2H-perfluorooctyltrichlorosilane (ABC R GmbH & Co. KG, Karlsruhe, Germany) to facilitate demoulding.¹³ PDMS monomer and hardener (Sylgard 184, Dow Corning, Midland, MI, USA) were mixed to a ratio of 10 : 1, degassed, poured onto the master and baked for 1 hour at 80 °C. Connection tubes were cast directly into the PDMS to avoid the need for any additional adhesive. Our first generation of devices were sealed with glass slides as is commonly done. In these devices we observed a high proportion of echinocytes (deformed RBCs). We discovered later that this is due to the proximity to the glass surface consistent with the observations by Lim *et al.*¹⁴ In order to avoid this problem we fabricated devices entirely in PDMS. The patterned PDMS slab was bonded to a blank PDMS slide following surface treatment with oxygen plasma (Plasma Preen II-862, Plasmatic Systems, Inc, North Brunswick, NJ, USA). A pressure gradient was used to drive flow through the DLD devices. Outlets were kept at atmospheric pressure and the overpressure at the three inlets was controlled individually using an MFCS-4C (Fluigent, Paris, France). This made it possible to hydrodynamically focus the sample into a stream of $\sim 10 \mu\text{m}$ in width. A schematic overview of the device is shown in Fig. 4a.

All images were taken through an inverted Nikon Eclipse TE2000-U microscope (Nikon Corporation, Tokyo, Japan) using an Andor Luca EMCCD camera (Andor Technology,

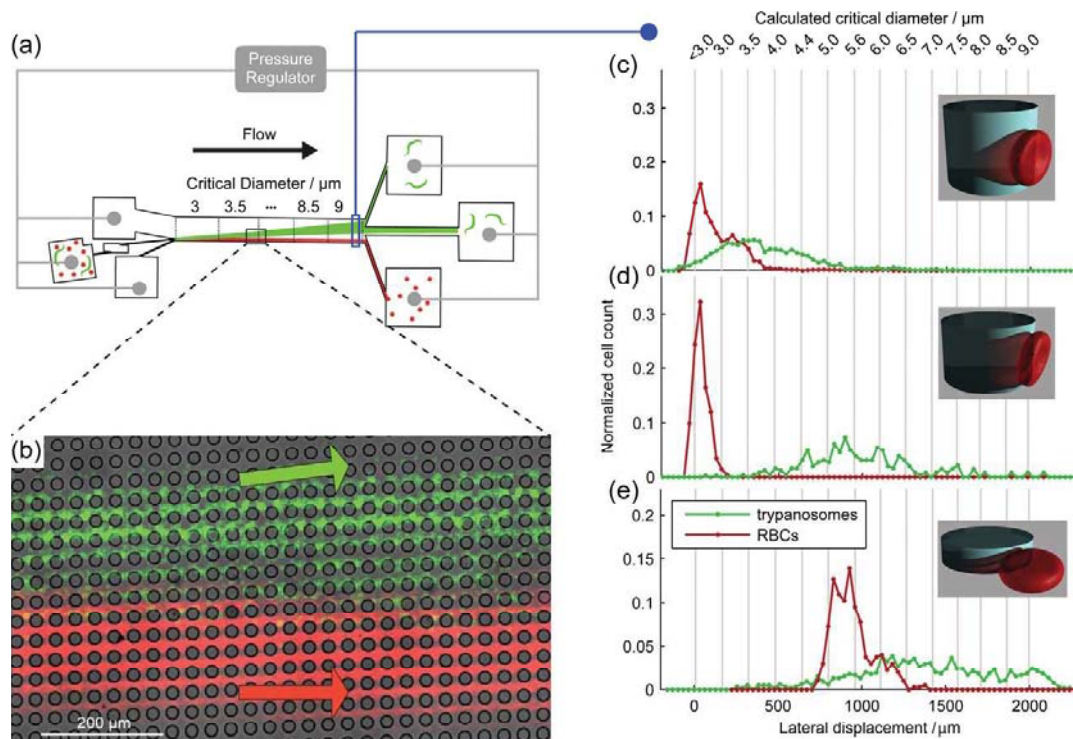


Fig. 4 (a) Overview of our DLD device. A focused stream of particles enters from the left. Particles larger than the critical diameter are laterally displaced (upwards in the figure) by $\sim 160 \mu\text{m}$ in each section and can be collected at the end of the device. The distributions of RBCs and *T. cyclops* are measured at the end of devices of three different depths. (b) A time-integrated micrograph showing a mixture of RBCs and parasites imaged in brightfield and coloured red. Overlaid on this image, in green, is an epifluorescence micrograph in which only the DAPI-stained trypanosomes can be seen having been displaced out of the stream of blood cells. (c) In a $33 \mu\text{m}$ deep device the RBCs behave like spherical particles with diameters of $3 \mu\text{m}$ or less with a lateral displacement of $x_{\text{RBC}} = 9 \pm 23 \mu\text{m}$. Trypanosomes, despite being much longer, are not displaced significantly more, $x_{\text{Tryp}} = 66 \pm 105 \mu\text{m}$, resulting in a large overlap. (d) In an $11 \mu\text{m}$ deep device the spread in the displacement of the trypanosomes is still large, $x_{\text{Tryp}} = 980 \pm 330 \mu\text{m}$. The mean displacement however is sufficiently large that the trypanosomes are almost all separated from the RBCs, which at this depth still behave like small particles, $x_{\text{RBC}} = 36 \pm 44 \mu\text{m}$. (e) In a $4 \mu\text{m}$ deep device the RBCs are confined such that they present their largest dimension, the diameter of the disc, to the array. Oriented thus they behave like particles with a diameter of around $6 \mu\text{m}$, $x_{\text{RBC}} = 944 \pm 123 \mu\text{m}$. Trypanosomes are also oriented such that their effective size increases, $x_{\text{Tryp}} = 1386 \pm 424 \mu\text{m}$. The variation in both the shape of trypanosomes and the manner by which they move through the array gives rise to the large spread in displacement, and a large overlap between the distributions.

Belfast, Northern Ireland). Differential Interference Contrast (DIC) was used to ensure adequate contrast of blood cells and trypanosomes.

Fluorescent polystyrene microspheres with diameters $4.87 \pm 0.12 \mu\text{m}$, $6.19 \pm 0.20 \mu\text{m}$ (Polysciences Inc., Warrington, PA; 18340, 19102), $3.00 \pm 0.15 \mu\text{m}$, $7.00 \pm 0.91 \mu\text{m}$ and $10.00 \pm 1.20 \mu\text{m}$ (Duke Scientific Corp. Palo-Alto, CA; R0300, 35-2, 36-3) were used to evaluate the device.

Particle tracking software was written in MATLAB 2009b (The MathWorks, Natick, MA, USA). The tracking program was based on available MATLAB code and optimized for our specific setup.[§] The software was able to track many particles in

a field of view when the signal-to-noise ratio was sufficiently high and when the concentration was low enough to avoid particle overlap. This made it possible to obtain readings of particle trajectories of several hundreds of cells per experiment. However, for the final simultaneous measurement of undiluted blood and trypanosomes ImageJ 1.43 was used instead to evaluate the separation. By removing the static background and generating binary images, a time-integrated micrograph could be constructed which closely matched the actual distributions. Despite being less accurate than the particle tracking software, this method does not need to be able to discriminate between separate particles making it more suitable for analysis of samples of high concentration. Still, particle overlap will lead to underestimation of the number of cells in regions of high concentration giving the appearance of broader distributions with less sharp peaks.

For work with blood and *T. cyclops*, surfaces were treated to minimize adhesion. Immediately after O_2 plasma treatment and

[§] The tracking program was built around a free MATLAB adaption of the IDL Particle Tracking software, and can be found at <http://www.physics.georgetown.edu/matlab/>. This intensity-based tracking core was optimised for reduced noise and correct path detection.

bonding, devices were filled with 0.2% PLL(20)-g[3.5]-PEG(2) (SuSoS AG, Dübendorf, Switzerland) in DI water and allowed to rest for at least 20 min before rinsing with DI water for another 20 min.

Long-time storage of *T. cyclops* was achieved at $-80\text{ }^{\circ}\text{C}$ in 10% dimethyl sulfoxide (DMSO, Fluka, St Louis, MO: 41639). After thawing, trypanosomes were incubated in Cunningham's medium¹⁵ with 20% Fetal Calf Serum (FCS, Sigma-Aldrich, St Louis, MO: F2442) at $28\text{ }^{\circ}\text{C}$ under which conditions the parasites proliferated. A full description of freezing, reactivation and cell culturing can be found in the ESI, Section 3†.

Blood was extracted from the first authors, *via* finger pricking and diluted around 20 times to facilitate particle tracking in autoMACS™ running buffer (Miltenyi Biotech, Auburn, CA). Because blood serum is known to lyse *T. cyclops*,¹² in the experiments where blood and parasites were run simultaneously, serum was removed and blood cells resuspended in autoMACS™. Section 4 of the ESI† contains details.

The experiments were carried out in two stages. Firstly separations were performed at low concentration in order to enable automated particle tracking. The purpose of this first step was to find the device depth which maximizes separation of RBCs and parasites. Once the optimum depth was found a second series of measurements was performed in order to verify that the device would also function with whole blood.

5. Results and discussion

While the behaviour of spherical particles is reasonably well described by eqn (1), non-spherical particles behave in a much more complex fashion and a new approach to device design is warranted.

Device depth, we discovered, has a large effect on the displacement of both RBCs and parasites. In order to evaluate the sorting efficiency we defined the purified fraction, F_p , as the fraction of trypanosomes captured with a lateral displacement chosen such that 99% of the RBCs are rejected in the device.

This percentage is chosen to estimate the fraction of trypanosomes that can be collected with 100-fold enrichment. As the vast majority of blood cells are RBCs this is a valid estimation. Fig. 4c–e shows the distributions of *T. cyclops* and of RBCs at the end of three of our devices, almost identical except for depth. During fabrication we aimed for a gap size of $12\text{ }\mu\text{m}$ in all three devices. Although the same photo-mask was used in all three cases, some variation in the gap size is inevitably introduced due to the variation in resist thickness and the processing parameters needed in each case. Fig. S1d, in the ESI†, shows micrographs of thin slices of the three PDMS devices in which the gap, d , between posts can be seen in the profile. The gap in the $33\text{ }\mu\text{m}$ device is marginally narrower ($\leq 10\%$) than in the other two devices. The smaller gap leads to a $\leq 10\%$ reduction in critical size in the $33\text{ }\mu\text{m}$ device compared to the values shown in the ESI, Table S1†. The result of this is that while RBCs are not displaced in the $11\text{ }\mu\text{m}$ deep device, a fraction of them ($\sim 1/3$) are displaced in section two of the $33\text{ }\mu\text{m}$ device. This leads to a broadening of the distribution. One would also expect the parasites to be displaced marginally more in this device, but as we will discuss below, the effects of device depth dominate their behaviour.

In a $33\text{ }\mu\text{m}$ deep device RBCs behave like particles around $3\text{ }\mu\text{m}$ in diameter and parasites like particles in the range $3\text{--}5\text{ }\mu\text{m}$ and almost no separation occurs, $F_p = 14.0\%$. In a $11\text{ }\mu\text{m}$ deep device the RBCs behave like particles smaller than $3\text{ }\mu\text{m}$ but *T. cyclops* are displaced to a much greater degree. At this depth RBCs and *T. cyclops* are well separated, $F_p = 99.5\%$. In a $4.0\text{ }\mu\text{m}$ deep device the RBCs behave like particles with an effective diameter of $\sim 6\text{ }\mu\text{m}$ while the mean displacement of *T. cyclops* also increases relative to the deeper devices. In a device as shallow as $4.0\text{ }\mu\text{m}$, due to the overlap in the distributions of both *T. cyclops* and RBCs, separation is very poor, $F_p = 53\%$.

The increased displacement comes about when particles, partially confined in shallow channels, are forced to adopt orientations that give them a greater effective size in the device. For RBCs that have a biconcave disc shape, see Fig. 3, the effect is, we believe, solely due to orientation constraints. In a $33\text{ }\mu\text{m}$ deep device (Fig. 4c) RBCs have room to rotate and will be forced to do so by a combination of the shear field and the interactions with posts. Because of this rotation they present their smallest dimensions to the array. The inset shows the orientation of an RBC in a deep device. For an RBC the smallest dimension is around $2.5\text{ }\mu\text{m}$ and indeed the RBCs are displaced by a similar amount as microspheres smaller than $3\text{ }\mu\text{m}$ diameter. In the $11\text{ }\mu\text{m}$ deep device, Fig. 4d, the orientation of RBCs is the same as that in the $33\text{ }\mu\text{m}$ deep device and the displacement therefore the same. It is only when the depth of the device becomes smaller than the diameter of RBCs that an effect is observed. In a $4.0\text{ }\mu\text{m}$ device (Fig. 4e) the rotation of RBCs is severely constrained and they present their largest dimension to the device (see inset) giving them an effective size of $\sim 6\text{ }\mu\text{m}$, close to their diameter.

The increase in the effective size of the trypanosomes is more complex and not as intuitive or as easily characterised as that of the RBCs. A series of videos can be found in Section 5 of the

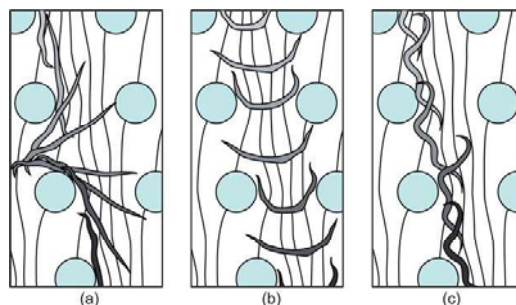


Fig. 5 Mechanisms that give long particles a larger effective size (see ESI, Section 5† for corresponding movies). (a) Shear forces in conjunction with post-particle interactions can give rise to rotation. When a particle is perpendicular with the direction of flow it is influenced by many flow streams and the effective size is increased. (b) Long but flexible particles such as *T. cyclops* can be seen locked into a u-shape. In this case they are unable to rotate in the space between one row and the next and they behave like particles with a large effective size. (c) Even in the absence of the effects described in (a) and (b), when parasites are aligned with the flow direction, their bent shape gives rise to an effective size that is larger than their width. This effective size could fluctuate if the parasite is motile and constantly changing shape.

ESI† in which parasites can be seen moving through sections 2 and 6 of devices of different depths. Fig. 5 shows some sketches that summarize the most frequently observed modes of motion that lead to increased effective size.

Because the *T. cyclops* are around 30 μm in length the orientation constraints should be minimal in the 33 μm deep device. This can also be seen in Fig. 4c where they are not significantly displaced. In an 11 μm deep device (Fig. 4d) *T. cyclops* are constrained to a degree that greatly changes their effective sizes leading to greater lateral displacement. Because the orientations of RBCs are not constrained at this depth the amount by which they can be separated from parasites is greatly increased. As can be seen in Fig. 4e, *T. cyclops* are displaced to an even greater extent in the 4.0 μm deep device than in the 11 μm device but because RBCs are also affected at this depth the overlap in displacement distributions results in a poor separation.

Rotation has a considerable effect on particles as long, thin and relatively rigid as trypanosomes. Fig. 5a illustrates how, when perpendicular to the flow direction, a long particle will be influenced by many flow streams that can force the particle to move in the displacement mode.

As long, flexible particles rotate they tend to become trapped in a U-shape configuration between rows of posts in the fashion illustrated in Fig. 5b. The shallower the device, the more frequently this trapping occurs. This mode of transport through the device appears to be stable and once parasites entered this mode they moved for long distances through the device without rotation and without becoming stuck. In this configuration the parasites have the largest possible effective size.

The fact that the parasites are not straight also influences their effective size as depicted in Fig. 5c. This together with the constant undulation due to the motion of their flagella contributes to an increase in their effective size (the flagella can be seen in white along the side of the parasite in Fig. 3 and a swimming parasite is shown in the ESI, Section 5†). The flagellar movement gives rise to a swimming speed of 20 $\mu\text{m s}^{-1}$ which is small compared to the velocity through the array (600 $\mu\text{m s}^{-1}$) and is therefore not expected to affect the displacement significantly.

In general the trend we observe is that the modes shown in Fig. 5 become more prevalent as devices become shallower and that this collectively leads to greater lateral displacement of the parasites in our devices.

In the second series of measurements we focused on the 11 μm deep device which gave the highest separation efficiency in the previous measurements with a pure trypanosome fraction of $F_p = 99.5\%$. Because a future diagnostic device should be able to deal with whole blood it is important that the device can function both at those cell concentrations found in blood and also in the presence of serum. Because serum kills *T. cyclops* (as explained above) this was demonstrated in two separate experiments.

Firstly we injected the resuspended blood and parasites, at whole blood concentration, into the device with the results shown in Fig. 6. Despite a small broadening of the RBC peak, the separation efficiency was not degraded, $F_p = 99.6\%$. The RBCs still behave like spherical particles of 3 μm or less with a small lateral displacement, $x_{\text{RBC}} = 24 \pm 75 \mu\text{m}$. The lateral displacement of the trypanosomes is also in agreement with the first series of measurements at this depth, $x_{\text{tryp}} = 841 \pm 259 \mu\text{m}$. While many WBCs are too large to enter the device the behaviour of

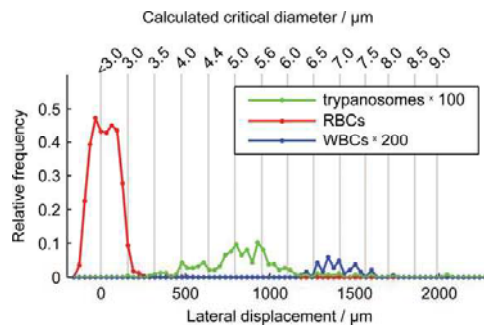


Fig. 6 Evaluation of trypanosomes in resuspended whole blood. The lateral displacements of RBCs and trypanosomes are $x_{\text{RBC}} = 24 \pm 75 \mu\text{m}$ and $x_{\text{tryp}} = 841 \pm 259 \mu\text{m}$ respectively with a purified fraction of $F_p = 99.6\%$. This is in parallel with the preceding diluted separation experiment at this depth except for the broader distribution profile of the RBCs which in part is due to particle overlap as previously discussed. The behaviour of WBCs was also characterised and they were found to become separated from the major trypanosome fraction. $x_{\text{WBC}} = 1400 \pm 111 \mu\text{m}$. The number of counted cells are $n_{\text{RBC}} = 19\,700$, $n_{\text{WBC}} = 61$ and $n_{\text{trypanosomes}} = 435$. The sample concentrations are $c_{\text{RBC}} = 4.9 \times 10^6 \mu\text{L}^{-1}$, $c_{\text{WBC}} = 2600 \mu\text{L}^{-1}$, $c_{\text{trypanosomes}} = 8400 \mu\text{L}^{-1}$.

those small enough to do so ($<11 \mu\text{m}$) was also characterized in these measurements and they were found to be laterally displaced by the same amount as $\sim 7 \mu\text{m}$ sized spherical particles, $x_{\text{WBC}} = 1400 \pm 111 \mu\text{m}$, meaning that they are also separated from the parasites. The size and number concentration of these WBCs suggest that they are lymphocytes, which are between 7 and 8 μm in diameter and are present in blood at concentrations around 2000 μL^{-1} .

Secondly, using Na_2EDTA at 1.75 mg mL^{-1} as an anticoagulant we were able to flow whole blood through the device for 75 minutes with no visible clogging of cells and no change in the critical size in the devices. See ESI, Section 6† for more details.

While shallow devices separate a much higher fraction of parasites from blood there are some limitations. Large blood cells such as monocytes (14–17 μm) and neutrophils (10–12 μm) might clog the device. The experiment with whole blood shows that while some WBCs undoubtedly become stuck at the entrance to the channel, this has a large area and does not become blocked in the first 75 minutes at least. The filter in the sample inlet also removes any WBCs that would otherwise become stuck in the pillar array. Since we are only interested in finding parasites, provided clogging does not occur over the relevant timescales for the experiment (less than 1 hour) WBCs are not expected to constitute a problem. Clogging due to WBCs could further be decreased either by improving the entrance to the device and the prefilter or alternatively by implementing a two step separation in which the WBCs, which have larger effective sizes than both RBCs and parasites at any device depth, are first removed in an array that is deeper than the largest blood cells (e.g. $>20 \mu\text{m}$).

The volume flow and therefore throughput of a shallow device are also less than for a deeper channel with otherwise equal dimensions. The device we present here was designed to study the behaviour of individual, non-spherical particles as device depth is

altered, which is best done with a narrow sample stream. There is therefore much room to improve the throughput in the next generation of devices. The following are a few examples of how this could be done.

In addition to working with whole blood to further increase the throughput the width of the sample stream could be increased from 10 μm to 1 mm and still make the device no longer than a microscope slide. Making devices thin¹⁶ would also make it possible to stack multiple devices and run them in parallel with a single inlet and a single outlet. These steps alone would increase the throughput from the 1 nL s⁻¹ in our current device to 1 $\mu\text{L s}^{-1}$. With a goal of one million true positives per false negative on average we need to (assuming Poisson statistics) collect 6 ln 10 \approx 14 parasites. With a lowest target concentration of 100 parasites per mL this translates into 140 μL of blood which would take less than three minutes to sort.

The way we envision our method being of use is as a preparative step before either conventional smear examination or automated, on-chip detection of parasites. The latter would be more time and cost-effective and could be achieved by first capturing and concentrating the parasites after separation from RBCs using for example sieving structures or sticky surface modifications followed by subsequent detection with a cheap, field-portable camera such as the cell-phone cameras developed by the Ozcan group (see ref. 17 for an example). This one-step device would constitute a considerable improvement compared to the aforementioned more complicated and labor-intensive techniques such as mAECT and QBC.

In addition to possible utility in finding African trypanosomes in the blood of human or animal victims of trypanosomiasis, it is noteworthy that related parasites e.g. *Trypanosoma cruzi*, the causative agent of Chagas disease in Latin America and *Leishmania* species responsible for the leishmaniasis throughout the tropical and sub-tropical world, can also present as elongate, flagellated cells in mammalian blood. These could also be separated using the same basic principals outlined here. These latter parasites, however, spend much of their time within the mammalian host, as intracellular amastigote forms, hence the general utility for diagnosis of the diseases caused by the parasites would require further evaluation.

6. Conclusions

We have successfully shown how particle orientation, controlled via device depth, can be used to accentuate morphological differences making possible the sorting of otherwise indistinguishable particles in DLD devices. We have separated *T. cyclops*, a non-pathogenic relative of *T. brucei* from RBCs opening up for a cheap, simple to use, point-of-care, diagnostics

tool. The next generation of devices will be designed to achieve both a higher throughput and a lower detection limit along with features for the capture and concentration of the parasites.

Acknowledgements

This work was carried out within nmC@LU (the Nanometer Structure Consortium at Lund University). The work was supported by the Swedish Foundation for Strategic Research (SSF), the Swedish Research Council (VR) grant nr. 2007 584, the Crafoord Foundation grant no. 2008 0841 and 2005 1123, and the Knut and Alice Wallenberg Foundation. We would also like to extend our gratitude to Dr Mathis Riehle for first introducing us to the problem of HAT diagnostics.

References

- 1 M. P. Barrett, R. J. S. Burchmore, A. Stich, J. O. Lazzari, A. C. Frasch, J. J. Cazzulo and S. Krishna, *Lancet*, 2003, **362**, 1469–1480.
- 2 M. P. Barrett, D. W. Boykin, R. Brun and R. R. Tidwell, *Br. J. Pharmacol.*, 2007, **152**, 1155–1171.
- 3 F. Chappuis, L. Loutan, P. Simarro, V. Lejon and P. Buscher, *Clin. Microbiol. Rev.*, 2005, **18**, 133–146.
- 4 P. Dukes, W. C. Gibson, J. K. Gashumba, K. M. Hudson, T. J. Bromidge, A. Kaukus, T. Asonganyi and E. Magnus, *Acta Trop.*, 1992, **51**, 123–134.
- 5 P. Lutumba, J. Robays, C. Miaka, V. Kande, D. Mumba, P. Büscher, B. Dujardin and M. Boelaert, *Trop. Med. Int. Health*, 2006, **11**, 470–478.
- 6 E. Matovu, A. Kazibwe, A. Boobo, S. Biéler and J. Ndung'u, *Revisiting Red Blood Cell Lysis as a Critical Step in Demonstrating Trypanosomes in Patient Blood*, FIND, Geneva, Switzerland, 2009.
- 7 L. R. Huang, E. C. Cox, R. H. Austin and J. C. Sturm, *Science*, 2004, **304**, 987–990.
- 8 J. A. Davis, D. W. Inglis, K. J. Morton, D. A. Lawrence, L. R. Huang, S. Y. Chou, J. C. Sturm and R. H. Austin, *Proc. Natl. Acad. Sci. U. S. A.*, 2006, **103**, 14779–14784.
- 9 D. W. Inglis, J. A. Davis, T. J. Zieziulewicz, D. A. Lawrence, R. H. Austin and J. C. Sturm, *J. Immunol. Methods*, 2008, **329**, 151–156.
- 10 J. A. Davis, PhD thesis, Princeton University, 2008.
- 11 J. Beech and J. Tegenfeldt, *The Thirteenth International Conference on Miniaturized Systems for Chemistry and Life Sciences*, Jeju, Korea, 2009, 800–802.
- 12 D. Weinman, *Trans. R. Soc. Trop. Med. Hyg.*, 1972, **66**, 628–633, IN621–IN622, 634–636.
- 13 M. Beck, M. Graczyk, I. Maximov, E. L. Sarwe, T. G. I. Ling, M. Keil and L. Montelius, *Microelectron. Eng.*, 2002, **61-2**, 441–448.
- 14 G. H. W. Lim, M. Wortis and R. Mukhopadhyay, *Proc. Natl. Acad. Sci. U. S. A.*, 2002, **99**, 16766–16769.
- 15 I. Cunningham, *J. Protozool.*, 1977, **24**, 325–329.
- 16 J. P. Beech, T. Mäkelä, P. Majander and J. O. Tegenfeldt, *The 12th International Conference on Miniaturized Systems for Chemistry and Life Sciences*, San Diego, USA, 2008, 1492–1494.
- 17 O. Mudanyali, C. Oztoprak, D. Tseng, A. Erlinger and A. Ozcan, *Lab Chip*, 2010, **10**, 2419–2423.

References

1. S. H. Holm, J. P. Beech, M. P. Barrett and J. O. Tegenfeldt, *Lab on a Chip*, 2011, **11**, 1326-1332.
2. H. A. Noyes, M. H. Alimohammadian, M. Agaba, A. Brass, H. Fuchs, V. Gailus-Durner, H. Hulme, F. Iraqi, S. Kemp, B. Rathkolb, E. Wolf, M. H. de Angelis, D. Roshandel and J. Naessens, *PloS one*, 2009, **4**, e5170.
3. H. H. Goldstine, *The computer from Pascal to von Neumann*, Princeton University Press, 1980.
4. M. Yamada and M. Seki, *Lab on a Chip*, 2005, **5**, 1233-1239.
5. M. Yamada, M. Nakashima and M. Seki, *Analytical Chemistry*, 2004, **76**, 5465-5471.
6. J. Takagi, M. Yamada, M. Yasuda and M. Seki, *Lab on a Chip*, 2005, **5**, 778-784.
7. Y. T. Shevkoplyas SS, Munn LL, Bitensky MW., *Anal Chem.*, 2005, **77**, 933-937.
8. H. W. Hou, A. A. S. Bhagat, A. G. Lin Chong, P. Mao, K. S. Wei Tan, J. Han and C. T. Lim, *Lab on a Chip*, 2010, **10**, 2605-2613.
9. S. M. McFaul, B. K. Lin and H. Ma, *Lab on a Chip*, 2012.
10. S. S. Kuntaegowdanahalli, A. A. S. Bhagat, G. Kumar and I. Papautsky, *Lab on a Chip*, 2009, **9**, 2973-2980.
11. D. Di Carlo, J. F. Edd, D. Irimia, R. G. Tompkins and M. Toner, *Analytical Chemistry*, 2008, **80**, 2204-2211.
12. D. Gossett, W. Weaver, A. Mach, S. Hur, H. Tse, W. Lee, H. Amini and D. Di Carlo, *Analytical & Bioanalytical Chemistry*, 2010, **397**, 3249-3267.
13. D. Di Carlo, *Lab on a Chip*, 2009, **9**, 3038-3046.
14. A. Lenshof and T. Laurell, *Chemical Society Reviews*, 2010, **39**, 1203-1217.
15. L. R. Huang, E. C. Cox, R. H. Austin and J. C. Sturm, *Science*, 2004, **304**, 987-990.
16. N. T. K. Sasso L., Snakenborg D., and Kutter J.P., *American biotechnology laboratory*, 2009, **27**, 13-15.

References

17. J. V. Green, M. Radisic and S. K. Murthy, *Analytical Chemistry*, 2009, **81**, 9178-9182.
18. L. A. Herzenberg, D. Parks, B. Sahaf, O. Perez, M. Roederer and L. A. Herzenberg, *Clinical Chemistry*, 2002, **48**, 1819-1827.
19. A. Trickett and Y. L. Kwan, *Journal of Immunological Methods*, 2003, **275**, 251-255.
20. P. Y. J P Brody, *Sensors and Actuators A: Physical*, 1997, **58**, 13-18.
21. J. P. Brody and P. Yager, *Sensors and Actuators A: Physical*, 1997, **58**, 13-18.
22. B. S. Cho, T. G. Schuster, X. Zhu, D. Chang, G. D. Smith and S. Takayama, *Analytical Chemistry*, 2003, **75**, 1671-1675.
23. S. V. Shadomy, S. C. Waring and C. L. Chappell, *Clinical and Diagnostic Laboratory Immunology*, 2004, **11**, 313-319.
24. M. J. Fulwyler, *Science*, 1965, **150**, 910-911.
25. N. Ross, C. Pritchard, D. Rubin and A. Dusé, *Medical and Biological Engineering and Computing*, 2006, **44**, 427-436.
26. H. Ceelie, R. B. Dinkelaar and W. van Gelder, *Journal of Clinical Pathology*, 2007, **60**, 72-79.
27. H. Bruus, *Theoretical Microfluidics*, Oxford University Press, 2008.
28. S. T. W. Nam-Trung Nguyen, *Fundamentals and applications of microfluidics*, 2nd edn., Artech House, INC., 2006.
29. J. S. Hansen, J. C. Dyre, P. J. Davis, B. D. Todd and H. Bruus, *Physical Review E*, 2011, **84**, 036311.
30. N. A. Mortensen, F. Okkels and H. Bruus, *Physical Review E*, 2005, **71**, 057301.
31. H. Bruus, Technical University of Denmark, 2006.
32. A. D. Stroock, S. K. W. Dertinger, A. Ajdari, I. Mezić, H. A. Stone and G. M. Whitesides, *Science*, 2002, **295**, 647-651.
33. R. H. Liu, M. A. Stremler, K. V. Sharp, M. G. Olsen, J. G. Santiago, R. J. Adrian, H. Aref and D. J. Beebe, *Microelectromechanical Systems, Journal of*, 2000, **9**, 190-197.
34. N. Xize and L. Yi-Kuen, *Journal of Micromechanics and Microengineering*, 2003, **13**, 454.
35. B. H. Weigl and P. Yager, *Science*, 1999, **283**, 346-347.
36. M. Balvin, E. Sohn, T. Iracki, G. Drazer and J. Frechette, *Physical Review Letters*, 2009, **103**, 078301.
37. J. A. Davis, Princeton University, 2008.

38. D. W. Inglis, Princeton University, 2007.
39. D. W. Inglis, J. A. Davis, R. H. Austin and J. C. Sturm, *Lab on a Chip*, 2006, **6**, 655-658.
40. B. R. Long, M. Heller, J. P. Beech, H. Linke, H. Bruus and J. O. Tegenfeldt, *Physical Review E*, 2008, **78**, 046304.
41. M. Luo, F. Sweeney, S. R. Risbud, G. Drazer and J. Frechette, *Applied Physics Letters*, 2011, **99**, 064102.
42. J. P. Beech, S. H. Holm, K. Adolfsson and J. O. Tegenfeldt, *Lab on a Chip*, 2012, **12**.
43. G. P. J. Bessman JD, Gardner FH., *Am J Clin Pathol.* , 1983, **80**, 322-326.
44. J. P. Beech, P. Jonsson and J. O. Tegenfeldt, *Lab on a Chip*, 2009, **9**, 2698-2706.
45. J. P. Beech and J. O. Tegenfeldt, *Lab on a Chip*, 2008, **8**, 657-659.
46. J. A. Davis, D. W. Inglis, K. J. Morton, D. A. Lawrence, L. R. Huang, S. Y. Chou, J. C. Sturm and R. H. Austin, *Proceedings of the National Academy of Sciences*, 2006, **103**, 14779-14784.
47. K. Louthback, KS Chou, J. Newman, J. Puchalla, R. H. Austin, and J. C. Sturm, *MICROFLUIDICS AND NANOFUIDICS*, 2010, **9**, 1143-1149.
48. J. P. Beech, Tegenfeldt, J.O., in *The 13th International Conference on Miniaturized Systems for Chemistry and Life Sciences*, Jeju, Korea, 2009.
49. S. Sugaya, M. Yamada and M. Seki, *Biomicrofluidics*, 2011, **5**, 024103-024113.
50. S. C. Hur, S.-E. Choi, S. Kwon and D. D. Carlo, *Applied Physics Letters*, 2011, **99**, 044101.
51. WHO, 1999, vol. 2011.
52. W. O. Inojosa, I. Augusto, Z. Bisoffi, T. Josenado, P. M. Abel, A. Stich and C. J. M. Whitty, *BMJ*, 2006, **332**, 1479.
53. A. Stich, P. M. Abel and S. Krishna, *BMJ*, 2002, **325**, 203-206.
54. IAEA, 2011, vol. 2012.
55. I. A. E. Agency, IAEA/FPO, Vienna, 2011, vol. 2011.
56. F. Chappuis, L. Loutan, P. Simarro, V. Lejon and P. Buscher, *Clin. Microbiol. Rev.*, 2005, **18**, 133-146.
57. J. K. Thuita, J. M. Kagira, D. Mwangangi, E. Matovu, C. M. R. Turner and D. Masiga, *PLoS Neglected Tropical Diseases*, 2008, **PLoS N**, e238.
58. WHO, N°259 edn., 2011, vol. 2011, p. Fact sheet
59. F. a. A. O. o. t. U. Nations, Food and Agriculture Organization of the United Nations, Rome, 1998, vol. 2011.

References

60. W. H. Organization, World Health Organization, Vienna, 2009, vol. 2011.
61. WHO, 2011, vol. 2012.
62. T. K. Jha and V. K. Sharma, *Transactions of the Royal Society of Tropical Medicine and Hygiene*, 1984, **78**, 252-253.
63. O. V. Nikolskaia, A. P. C. de A. Lima, Y. V. Kim, J. D. Lonsdale-Eccles, T. Fukuma, J. Scharfstein and D. J. Grab, *The Journal of Clinical Investigation*, 2006, **116**, 2739-2747.
64. J. K. Thuita, J. M. Kagira, D. Mwangangi, E. Matovu, C. M. R. Turner and D. Masiga, *PLoS Negl Trop Dis*, 2008, **2**, e238.
65. CDC, 2011, vol. 2011.
66. FAO, 1998, vol. 2010.
67. K. L. Hill, *Eukaryotic Cell*, 2003, **2**, 200-208.
68. J. David Barry and R. McCulloch, in *Advances in Parasitology*, Academic Press, 2001, vol. Volume 49, pp. 1-70.
69. C. Paquet, T. Ancelle, M. Gastellu-Etchegorry, J. Castilla and I. Harndt, *The Lancet*, 1992, **340**, 250.
70. J. J. Penchenier L, Moulia-Pelat JP, Elfassi de la Baume F, Fadat G, Chanfreau B, Eozenou P., *Ann Soc Belg Med Trop*, 1991, **71**, 221-228.
71. K. P. Henry MC, Ruppel JF, Bruneel H, Claes Y., *Ann Soc Belg Med Trop.*, 1981, **61**, 79-92.
72. W. H. R. Lumsden, C. D. Kimber, D. A. Evans and S. J. Doig, *Transactions of the Royal Society of Tropical Medicine and Hygiene*, 1979, **73**, 312-317.
73. P. Büscher, D. Mumba Ngoyi, J. Kaboré, V. Lejon, J. Robays, V. Jamonneau, N. Bebronne, W. Van der Veken and S. Biéler, *PLoS Negl Trop Dis*, 2009, **3**, e471.
74. R. A. Levine, S. C. Wardlaw and C. L. Patton, *Parasitology today (Personal ed.)*, 1989, **5**, 132-134.
75. M. Toro, E. Leon and R. Lopez, *Veterinary Parasitology*, 1981, **8**, 23-29.
76. P. Lutumba, J. Robays, C. Miaka, V. Kande, D. Mumba, P. Büscher, B. Dujardin and M. Boelaert, *Tropical Medicine & International Health*, 2006, **11**, 470-478.
77. V. M. Nantulya, *Transactions of the Royal Society of Tropical Medicine and Hygiene*, **91**, 551-553.
78. T. Asonganyi, F. Doua, S. N. Kibona, Y. M. Z. Nyasulu, R. Masake and F. Kuzoe, *Annals of Tropical Medicine and Parasitology*, 1998, **92**, 837-844.

References

79. R. Martini and E. Bartholomew, *Essentials of anatomy and physiology*, 4th ed. edn., Benjamin-Cummings Publishing Company, 2007.
80. B. Young, J. W. Heath, A. H. Stevens and G. Burkitt, *Wheater's Functional Histology: A Text and Colour Atlas*, 5th ed. edn., 2006.
81. G. P. Downey, D. E. Doherty, B. Schwab, E. L. Elson, P. M. Henson and G. S. Worthen, *Journal of Applied Physiology*, 1990, **69**, 1767-1778.
82. F. Krombach, S. Munzing, A. M. Allmeling, J. T. Gerlach, J. Behr and M. Dorger, *Environmental health perspectives*, 1997, **105 Suppl 5**, 1261-1263.
83. N. A. Campbell, Pearson Education, 8th Edition edn., 2008, p. 912.
84. R. Fänge, B. Lundh, A. Lundquist, H. Ringgren and J.-Ö. Swahn, *National Encyklopedin*, Stockholm, 2011, vol. 2011.
85. D. Venes, *Taber's Cyclopedic Medical Dictionary*, 21 edn., F.A. Davis Company, 2009.
86. L. T. Goodnough, B. Skikne and C. Brugnara, *Blood*, 2000, **96**, 823-833.
87. H. Lodish, A. Berk, S. L. Zipursky, P. Matsudaira, D. Baltimore and J. Darnell, *Molecular Cell Biology*, 4th edn., W. H. Freeman, New York, 2000.
88. P. L. LaCelle, *Semin Hematol*, 1970, **7**, 355-371.
89. J. J. Ipsaro and A. Mondragon, 2009, vol. 2011.
90. J. J. Ipsaro and A. Mondragón, *Blood*, 2010, **115**, 4093-4101.
91. J. H. Jeong, Y. Sugii, M. Minamiyama and K. Okamoto, *Microvascular Research*, 2006, **71**, 212-217.
92. in *Encyclopædia Britannica*, Encyclopædia Britannica Inc., 2012.
93. G. V. F. Seaman, *Journal of Supramolecular Structure*, 1973, **1**, 437-447.
94. F. C. M. e. al., *Annals of Hematology*, 1991, **64**.
95. K. Lindmark and K. G. Engström, *Biorheology*, 1996, **33**, 379-395.
96. P. C. Buchan, *British Journal of Haematology*, 1980, **45**, 97-105.
97. M. R. Hardeman, P. Goedhart and D. Breederveld, *Clinica Chimica Acta*, 1987, **165**, 227-234.
98. W. Groner, N. Mohandas and M. Bessis, *Clinical Chemistry*, 1980, **26**, 1435-1442.
99. J. R. Henriksen and J. H. Ipsen, *Eur Phys J E Soft Matter*, 2004, **14**, 149-167.
100. R. M. Hochmuth, *J Biomech*, 2000, **33**, 15-22.
101. E. Evans and A. Yeung, *Biophys J*, 1989, **56**, 151-160.

References

102. G. M. Artmann, K. L. Sung, T. Horn, D. Whittemore, G. Norwich and S. Chien, *Biophysical Journal*, 1997, **72**, 1434-1441.
103. E. Biernacki, *Gazeta Lekarska*, 1897, **17**, 962-996.
104. N. J. Van Haeringen and E. Glasius, *Clinica Chimica Acta*, 1970, **29**, 55-60.
105. B. S. Bull and J. D. Brailsford, *Blood*, 1972, **40**, 550-559.
106. M. Toner and D. Irimia, *Annu Rev Biomed Eng*, 2005, **7**, 77-103.
107. H. W. Hou, A. A. S. Bhagat, W. C. Lee, S. Huang, J. Han and C. T. Lim, *Micromachines*, 2011, **2**, 319-343.
108. A. Bhagat, H. Bow, H. Hou, S. Tan, J. Han and C. Lim, *Medical and Biological Engineering and Computing*, 2010, **48**, 999-1014.
109. N. Sutton, M. C. Tracey, I. D. Johnston, R. S. Greenaway and M. W. Rampling, *Microvascular Research*, 1997, **53**, 272-281.
110. J. P. Brody, Y. Han, R. H. Austin and M. Bitensky, *Biophys J*, 1995, **68**, 2224-2232.
111. S. C. Gifford, M. G. Frank, J. Derganc, C. Gabel, R. H. Austin, T. Yoshida and M. W. Bitensky, *Biophys J*, 2003, **84**, 623-633.
112. J. Li, G. Lykotrafitis, M. Dao and S. Suresh, *Proceedings of the National Academy of Sciences*, 2007, **104**, 4937-4942.
113. B. Lincoln, H. M. Erickson, S. Schinkinger, F. Wottawah, D. Mitchell, S. Ulvick, C. Bilby and J. Guck, *Cytometry A*, 2004, **59**, 203-209.
114. S. Wakasa, T. Yagi, Y. Akimoto, N. Tokunaga, K. Iwasaki and M. Umezu, eds. C. T. Lim and J. C. H. Goh, Springer Berlin Heidelberg, 2009, vol. 23, pp. 1422-1425.
115. A. A. f. C. Chemistry, Washington, 2011, vol. 2012.
116. R. Hoffman, B. Furie, E. J. Benz, P. McGlave, L. E. Silberstein and S. J. Shattil, *Hematology: Basic Principles and Practice*, Churchill Livingstone, New York, 2004.
117. A. C. Allison, *Transactions of the Royal Society of Tropical Medicine and Hygiene*, 1954, **48**, 312-318.
118. D. Zieve and D. R. Eltz, in *The A.D.A.M. Medical Encyclopedia*, American Accreditation HealthCare Commission, New York, 2012.
119. K. Harmon, *Scientific American*, 2010, vol. 2011.
120. T. Gersten, *Medline Plus*, New York, 2012, vol. 2011.
121. J. Beech and J. Tegenfeldt, *MicroTAS 2009*, The thirteenth International Conference on Miniaturized Systems for Chemistry and Life Sciences, Jeju, Korea, 2009.

References

122. W. Goossens, V. Van Duppen and R. L. Verwilghen, *Clinical & Laboratory Haematology*, 1991, **13**, 291-295.
123. D. Weinman, *Transactions of the Royal Society of Tropical Medicine and Hygiene*, 1972, **66**, 628-636.
124. I. Cunningham, *Journal of Eukaryotic Microbiology*, 1977, **24**, 325-329.
125. I. CUNNINGHAM, *Journal of Eukaryotic Microbiology*, 1977, **24**, 325-329.
126. P. Heywood and D. Weinman, *Journal of Eukaryotic Microbiology*, 1978, **25**, 287-292.
127. Y. Xia and G. M. Whitesides, *Angewandte Chemie International Edition*, 1998, **37**, 550-575.
128. D. W. Inglis, *Applied Physics Letters*, 2009, **94**, 013510.
129. G. Lim H. W., M. Wortis and R. Mukhopadhyay, *Proceedings of the National Academy of Sciences of the United States of America*, 2002, **99**, 16766-16769.
130. B. Daniel and D. Eric, Georgetown, 2009.
131. D. Tseng, O. Mudanyali, C. Oztoprak, S. O. Isikman, I. Sencan, O. Yaglidere and A. Ozcan, *Lab on a Chip*, 2010, **10**, 1787-1792.
132. N. Y. L. Lam, T. H. Rainer, R. W. K. Chiu and Y. M. D. Lo, *Clin Chem*, 2004, **50**, 256-257.
133. S. G. Banfi G, Lippi G., *Clin Chem Lab Med.*, 2007, **45**, 565-576.
134. M. P. Barrett, R. J. S. Burchmore, A. Stich, J. O. Lazzari, A. C. Frasch, J. J. Cazzulo and S. Krishna, *The Lancet*, 2003, **362**, 1469-1480.
135. M. P. Barrett, D. W. Boykin, R. Brun and R. R. Tidwell, *British Journal of Pharmacology*, 2007, **152**, 1155-1171.
136. P. Dukes, W. C. Gibson, J. K. Gashumba, K. M. Hudson, T. J. Bromidge, A. Kaukus, T. Asonganyi and E. Magnus, *Acta Tropica*, 1992, **51**, 123-134.
137. E. Matovu, A. Kazibwe, A. Boobo, S. Biéler and J. Ndung'u, *Revisiting red blood cell lysis as a critical step in demonstrating trypanosomes in patient blood*, 9, Geneva, Switzerland, 2009.
138. D. W. Inglis, J. A. Davis, T. J. Zieziulewicz, D. A. Lawrence, R. H. Austin and J. C. Sturm, *Journal of Immunological Methods*, 2008, **329**, 151-156.
139. J. A. Davis, Princeton University, 2008.
140. M. Beck, M. Graczyk, I. Maximov, E. L. Sarwe, T. G. I. Ling, M. Keil and L. Montelius, *Microelectronic Engineering*, 2002, **61-2**, 441-448.
141. I. Cunningham, *Journal of Protozoology*, 1977, **24**, 325-329.

References

142. J. P. Beech, T. Mäkelä, P. Majander and J. O. Tegenfeldt, San Diego, USA, 2008.
143. O. Mudanyali, C. Oztoprak, D. Tseng, A. Erlinger and A. Ozcan, *Lab Chip*, 2010, **10**, 2419-2423.



LUND
UNIVERSITY

Solid State Physics
Department of Physics
Lund University